
Doctoral Dissertations

Student Theses and Dissertations

Spring 2005

CAD model extraction of PCB signal discontinuity using a circuit extraction approach based on mixed-potential integral equation formulation

Shaofeng Luan

Follow this and additional works at: https://scholarsmine.mst.edu/doctoral_dissertations



Part of the [Electromagnetics and Photonics Commons](#)

Department: **Electrical and Computer Engineering**

Recommended Citation

Luan, Shaofeng, "CAD model extraction of PCB signal discontinuity using a circuit extraction approach based on mixed-potential integral equation formulation" (2005). *Doctoral Dissertations*. 1603.
https://scholarsmine.mst.edu/doctoral_dissertations/1603

This thesis is brought to you by Scholars' Mine, a service of the Missouri S&T Library and Learning Resources. This work is protected by U. S. Copyright Law. Unauthorized use including reproduction for redistribution requires the permission of the copyright holder. For more information, please contact scholarsmine@mst.edu.

**CAD MODEL EXTRACTION OF PCB SIGNAL DISCONTINUITY USING A
CIRCUIT EXTRACTION APPROACH BASED ON MIXED-POTENTIAL
INTEGRAL EQUATION FORMULATION**

by

Shaofeng Luan

A DISSERTATION

Presented to the Faculty of the Graduate School of the

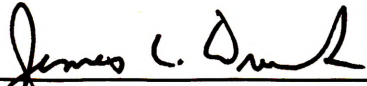
UNIVERSITY OF MISSOURI-ROLLA

In Partial Fulfillment of the Requirements for the Degree


DOCTOR OF PHILOSOPHY in ELECTRICAL ENGINEERING

2005

Approved by



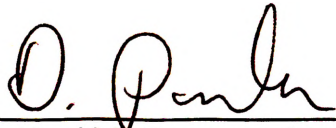
Dr. James L. Drewniak, Advisor



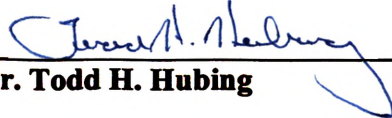
Dr. Jun Fan



Dr. Richard E. DuBroff



Dr. David J. Pommerenke



Dr. Todd H. Hubing



Dr. Barbara N. Hale

2-17-06
ah

© 2005

Shaofeng Luan

All Rights Reserved

ABSTRACT

In high-speed digital design, signal via transitions on printed circuit boards (PCBs) are becoming an important signal integrity issue. Efficient and accurate models for via transitions are necessary to analyze high bit-rate digital circuit system. The circuit extraction approach based on a mixed-potential integral equation formulation (CEMPIE) is an extension of the Partial Element Equivalent Circuit approach (PEEC) to general multi-layered media. CEMPIE was further developed to include the horizontal current components on the vertical surface and extended to model the discontinuities on multi-layer PCBs. A procedure of building SPICE models for signal via transitions between printed circuit board layers was developed. The method of extracting SPICE model parameters from full-wave simulation tool was studied. The validity of SPICE models was studied by comparing solutions from SPICE models with solutions from full-wave simulations. This procedure was further used for building SPICE models for via transitions in differential signaling.

ACKNOWLEDGMENTS

I would like to express my sincere gratitude to Dr. James L. Drewniak, my graduate advisor, for his inspiration, support and direction during the pursuit of my Ph.D. degree. I would like to extend my gratitude to Dr. Jun Fan for his guidance throughout my research. I would like to thank Dr. James L. Knighten for devoting his time and energy to advising my research.

Special thanks go to other faculty in the Electromagnetic Compatibility Laboratory (EMC Lab) at the University of Missouri-Rolla (UMR), Dr. David Pommerenke, Dr. Todd H. Hubing, Dr. Richard E. DuBroff, Dr. Thomas P. Van Doren, and Dr. Daryl G. Beetner for sharing their knowledge and experience in my study and research at UMR. I would like to thank Dr. Barbara N. Hale for her advices in my research. I would also like to thank my fellow students in the EMC Laboratory for their help.

I would like to thank my parents for their unconditional support. Most important, I want to thank my wife, Dr. Jing Wu, for all her love and support. Without them, I could not have accomplished my goals in pursuing my education. Finally, I would like to thank my lovely daughter, Jessica Luan. She has brought me so much happiness that I have never experienced before.

TABLE OF CONTENTS

	Page
ABSTRACT.....	iii
ACKNOWLEDGMENTS	iv
LIST OF ILLUSTRATIONS.....	vii
LIST OF TABLES	x
SECTION	
1. MODELING VERTICAL DISCONTINUITIES ON MULTI-LAYER PCBs USING A CIRCUIT EXTRACTION APPROACH BASED ON A MIXED- POTENTIAL INTEGRAL EQUATION FORMULATION	1
1.1. INTRODUCTION.....	1
1.2. CEMPIE FORMULATION	2
1.2.1. MPIE Formulation.	2
1.2.2. Basis Functions..	3
1.2.3. Partial Element Equivalent Circuit Extraction.....	13
1.2.4. Calculation of Green's Functions.	15
1.2.5. Analytic Integration of Some Components of the Green's Functions.	19
1.3. NUMERICAL RESULTS.....	33
1.4. CONCLUSION	37
2. VIA MODELS FOR SINGLE-ENDED SIGNALING.....	39
2.1. INTRODUCTION.....	39
2.2. MODELING A VIA WITH CEMPIE AND SPICE.....	40
2.3. LIBRARY MATRIX.....	43
2.4. PEELING PROCESS AND CHALLENGES	43
2.5. SIGNIFICANCE OF THE TRANSVERSE CURRENT.....	48
2.6. NEW BASIS FUNCTIONS FOR CEMPIE.....	57
2.7. EYE-DIAGRAM SIMULATION.....	58
2.8. CONCLUSION	59
3. VIA MODELS FOR DIFFERENTIAL SIGNALING.....	60

3.1. INTRODUCTION.....	60
3.2. PEELING AND PARTITIONING METHOD FOR VIA PAIR ON DIFFERENTIAL SIGNALING.....	60
3.3. BUILDING BLOCKS AND SPICE MODELS.....	62
3.4. EXTRACTION OF MODEL PARAMETERS.....	71
3.5. MODEL VALIDATION.....	83
3.6. CONCLUSION.....	88
APPENDICES	
A. SUB-CIRCUIT MODEL OF DIFFERENTIAL VIA TRANSITIONS.....	89
B. USER'S GUIDE OF CEMPIE.....	99
BIBLIOGRAPHY.....	104
VITA.....	107

LIST OF ILLUSTRATIONS

Figure	Page
1.1. A typical PCB structure and two kinds of PEC surfaces discretized in CEMPIE.....	3
1.2. The basis function for a triangular mesh.....	4
1.3. The basis function for vertical current component on rectangular mesh.....	5
1.4. The basis function for horizontal current component on rectangular mesh.....	6
1.5. Geometry for evaluation of basis functions at the edge between two patches	7
1.6. A typical circuit between any pair of two nodes m and n.....	15
1.7. A via transition on a 6-layer board	34
1.8. Modeling results— S_{11} using CEMPIE without horizontal current components on the vertical surface.....	35
1.9. Cascaded blocks with compensation inductors.....	35
1.10. Modeling results— S_{21} using CEMPIE without horizontal current components on the vertical surface.....	36
1.11. Current distribution of the test case in Figure 1.7.....	36
1.12. Modeling results— S_{11} using CEMPIE with the improved basis functions	37
1.13. Modeling results— S_{21} using CEMPIE with the improved basis functions	38
2.1. Geometry of a via transition for model extraction.....	41
2.2. Complete SPICE model for the entire via transition shown in Figure 2.1	42
2.3. Comparison of modeled results for the geometry shown in Figure 2.1	42
2.4. Building blocks for a standard 0.062'' board.	44
2.5. The meanings of underline and superscript in the library matrix	45
2.6. Via geometry and mesh patterns.....	46
2.7. Blocks and compensating inductances.....	47
2.8. Simulation results using the original CEMPIE for single-ended case.....	49
2.9. Side view of Block A-A (signal from left side goes back to left side of the via)	50
2.10. Magnitude of H-field at 2 GHz over the cross-section A-A' from MWS	51
2.11. Magnitude of H-field at 2 GHz over the cross-section B-B' from MWS.....	51
2.12. Magnitude of H-field at 2 GHz over the cross-section C-C' from MWS.....	52
2.13. Y component of H-field (associated with transverse current) at 2 GHz over the cross-section A-A' from MWS.....	52
2.14. Comparison of some simulation results.....	53
2.15. Side view of Block A-A (signal from left side goes to right side of the via).	54

2.16. Absolute magnitude of H-field at 2 GHz on the cross-section A-A' from MWS. ...	55
2.17. Absolute magnitude of H-field at 2 GHz on the cross-section B-B' from MWS....	55
2.18. Y component of H-field (associated with transverse current) at 2 GHz on the cross-section A-A' from MWS	56
2.19. Y component of H-field (associated with transverse current) at 2 GHz on the cross-section B-B' from MWS	56
2.20. Modeling results— S_{11} using CEMPIE with the improved basis functions	57
2.21. Modeling results— S_{21} using CEMPIE with the improved basis functions	58
2.22. Eye-diagram simulated using the circuit model of the via	59
3.1. Basic blocks for a 10-layer PCB.....	61
3.2. Circuit model for Block A.	62
3.3. Circuit model for Block B when signal makes reference to the top layer.	63
3.4. Circuit model for Block B when signal makes reference to the bottom layer.....	63
3.5. Circuit model for Block C.....	64
3.6. Circuit model for Block D.	64
3.7. Geometry of Block A_1	66
3.8. Geometry of Block A_2	67
3.9. Geometries of Block B_3 and B_5	67
3.10. Geometries of Block B_4 and B_6	68
3.11. Geometry of Block C_7	68
3.12. Geometry of Block C_8	69
3.13. Geometry of Block D_9	69
3.14. Geometry of Block D_{10}	70
3.15. Geometry of Block D_{11}	70
3.16. Geometries of Block D_{12}	71
3.17. The geometry used to extract the parameters of Block A_1	71
3.18. Comparison of S_{dd11}	73
3.19. Comparison of S_{dd21}	73
3.20. Comparison of S_{cc11}	73
3.21. Comparison of S_{cc21}	73
3.22. The geometry used to extract the parameters of Block D_9	74
3.23. Comparison of S_{dd11}	75
3.24. Comparison of S_{dd21}	75
3.25. Comparison of S_{cc11}	76

3.26. Comparison of S_{cc21}	76
3.27. Comparison of S_{dd11}	77
3.28. Comparison of S_{dd21}	77
3.29. Comparison of S_{cc11}	77
3.30. Comparison of S_{cc21}	78
3.31. The geometry used to extract the parameters of Block C_7	78
3.32. Comparison of S_{11}	79
3.33. Comparison of S_{21}	80
3.34. The geometry used to extract the parameters of Block B_3	80
3.35. Comparison of S_{dd11}	82
3.36. Comparison of S_{dd21}	82
3.37. Comparison of S_{cc11}	82
3.38. Comparison of S_{cc21}	83
3.39. A 6-layer structure that consists of Block A_1 , D_9 , D_{10} , B_3 and C_7	83
3.40. Comparison of magnitude of S_{dd11} of HSPICE model and full-wave model.....	84
3.41. Comparison of phase of S_{dd11} of HSPICE model and full-wave model	84
3.42. Comparison of magnitude of S_{dd21} of HSPICE model and full-wave model.....	85
3.43. Comparison of phase of S_{dd21} of HSPICE model and full-wave model	85
3.44. Comparison of magnitude of S_{cc11} of HSPICE model and full-wave model.....	85
3.45. Comparison of phase of S_{cc11} of HSPICE model and full-wave model.....	86
3.46. Comparison of magnitude of S_{cc21} of HSPICE model and full-wave model.....	86
3.47. Comparison of phase of S_{cc21} of HSPICE model and full-wave model.....	86
3.48. HSPICE model for a differential via pair	87

LIST OF TABLES

Table	Page
2.1. Library matrix for a 0.062" thick 10-layer printed circuit board.....	45
3.1. Geometry data sheet of blocks.....	65

1. MODELING VERTICAL DISCONTINUITIES ON MULTI-LAYER PCBs USING A CIRCUIT EXTRACTION APPROACH BASED ON A MIXED-POTENTIAL INTEGRAL EQUATION FORMULATION

The CEMPIE method is a Circuit Extraction approach based on a Mixed-Potential Integral Equation formulation [1]. CEMPIE is an extension of the Partial Element Equivalent Circuit approach (PEEC) to general multi-layered media. Finite dielectrics can be taken into account in PEEC, where the dielectric can be treated in a volume-integral formulation [2] -- [4]. CEMPIE handles infinite dielectric layers. It employs Green's functions for multi-layered media, thus the difficulties and complexity of a volume integral equation formulation due to an inhomogeneous medium can be transferred to the calculation of Green's functions. As a PEEC type method, the CEMPIE formulation results in an extracted circuit. The well developed SPICE sources, loads, transmission line models, and other lumped equivalent models may be easily incorporated into the first principle CEMPIE formulation [5]. The CEMPIE approach is typically used in lumped-circuit model extraction for vias [6] -- [9], DC power-bus modeling [1], [10] -- [12], and noise coupling modeling for PCB traces [13].

1.1. INTRODUCTION

The original CEMPIE formulation was first proposed by Hao Shi and J. Drewniak for planar structures without vertical discontinuities and can be found in [14]. Vertical discontinuities of planar power bus geometry were introduced into the first principle formulation by Jun Fan [1]. Currents were enforced to flow vertically on vertical metal surfaces in Jun Fan's model to simplify the formulation. Since in the power bus structure, the axial surface currents are dominant (the height of vias and ports of interests is relatively small compared with sizes of power buses), the error due to this simplification can be neglected. However, in some general cases, such as modeling via transitions for signal integrity, the horizontal components of currents on vertical surfaces must be considered. The improved sets of basis functions describing both horizontal and vertical components of currents on vertical surfaces are presented herein.

In Section 1.2, the MPIE formulation of the CEMPIE approach formulation is summarized and new basis functions are highlighted. An example is analyzed in Section

1.3, demonstrating the improvement of modeling results by incorporating horizontal current components on vertical surface. Some conclusive remarks are presented in Section 1.4.

1.2. CEMPIE FORMULATION

The CEMPIE approach is based on a Mixed Potential Integral Equation (MPIE) formulation, which is discretized and evaluated using a method of moment (MOM) procedure. Instead of solving the matrix equation directly, an equivalent circuit is extracted using partial element equivalent circuit concepts.

1.2.1. MPIE Formulation. Suppose a perfect electric conducting object with a surface S is located in space and exposed to an incident electric field \bar{E}^{inc} . The surface current density \bar{J} is induced as a result of the excitation. When S is open, \bar{J} is the vector sum of the surface currents on opposite sides of S . The scattered electric field is given by [15]

$$\bar{E}^s = -j\omega\bar{A} - \nabla\phi, \quad (1.1)$$

where

$$\bar{A} = \mu \int_S \bar{G}^A(\bar{r}, \bar{r}') \cdot \bar{J}(\bar{r}') ds', \quad (1.2)$$

$$\phi = \frac{1}{\epsilon} \int_S \sigma G^\phi(\bar{r}, \bar{r}') ds'. \quad (1.3)$$

The surface charge density σ is related to the surface divergence of \bar{J} through the equation of continuity,

$$-j\omega\sigma = \bar{\nabla}_s \cdot \bar{J}. \quad (1.4)$$

The EFIE (Electric Field Integral Equation) is formulated by enforcing the boundary condition on PEC,

$$n \times (\bar{E}^s + \bar{E}^{inc}) \Big|_s = 0, \quad (1.5)$$

or

$$\bar{E}_{tan}^{inc} = (j\omega\bar{A} + \nabla\phi) \Big|_{tan} = (j\omega\mu \int_S \bar{G}^A(\bar{r}, \bar{r}') \cdot \bar{J}(\bar{r}') ds' + \nabla\phi) \Big|_{tan}, \quad (1.6)$$

on S .

Since an equivalent circuit is extracted from this equation, the incident field is assumed to be zero in (1.6). Thus, impressed current sources, which are more easily to be handled than the incident wave, will be introduced in the circuit simulator later to represent the incident electric field.

1.2.2. Basis Functions. The RWG basis functions [15] are used to discretize horizontal PEC surfaces shown as S_1 in Figure 1.1. Rectangular patches are chosen here to discretize the vertical PEC surfaces S_2 . The mixed basis functions with triangle and rectangular patches simplify the complexity of calculation of Green's functions for layered media and make circuit extraction easier.

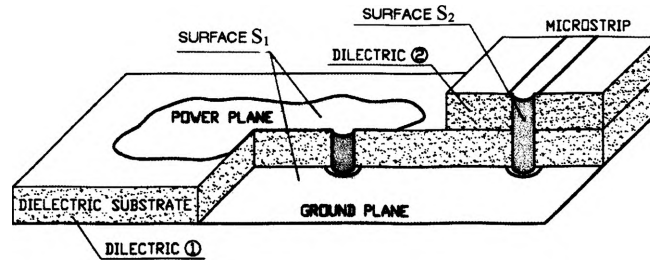


Figure 1.1. A typical PCB structure and two kinds of PEC surfaces discretized in CEMPIE.

For triangular patches, the current vector basis functions are anchored by the interior edges of triangles. As shown in Figure 1.2, the n^{th} interior edge \bar{l}_n has a length l_n , which uniquely defines two adjacent triangles, T_n^+ and T_n^- . The plus or minus designation of the T is determined by the choice of a positive current reference direction for the n^{th} edge, the reference for which is assumed to be from T_n^+ to T_n^- . Thus, the vector basis function associated with the n^{th} edge of a pair of adjacent triangle patches is defined as

$$\vec{f}_n^*(\vec{r}) = \begin{cases} \frac{l_n}{2A_n^+}(\vec{r} - \vec{r}_n^+), & \text{if } \vec{r} \in T_n^+, \\ -\frac{l_n}{2A_n^-}(\vec{r} - \vec{r}_n^-), & \text{if } \vec{r} \in T_n^-, \\ 0, & \text{otherwise.} \end{cases} \quad (1.7)$$

where the superscript h indicates that the basis function is defined for the horizontal triangular patches; A_n^+ and A_n^- are the areas of T_n^+ and T_n^- ; and, \bar{r}_n^+ and \bar{r}_n^- represent the free vertices of T_n^+ and T_n^- .

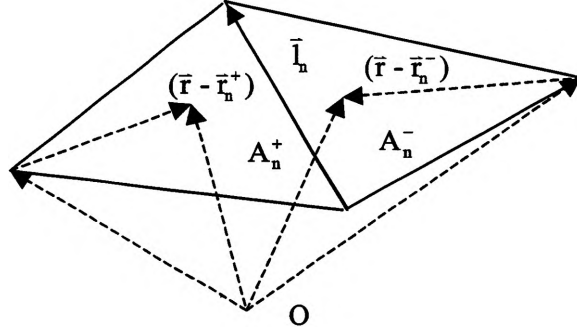


Figure 1.2. The basis function for a triangular mesh.

For rectangular patches on vertical surfaces, the vector basis functions of vertical current components are anchored by the horizontal edges of rectangles. As illustrated in Figure 1.3, the n^{th} interior edge \bar{l}_n has a length l_n , uniquely defining two adjacent rectangles R_n^+ and R_n^- . The plus or minus designation of the R is determined by the choice of a positive current reference direction for the n^{th} edge, the reference for which is assumed to be from R_n^+ to R_n^- . Then the vector current basis function associated with this edge is defined as

$$\bar{f}_n^{vv}(\bar{r}) = \begin{cases} \frac{l_n}{A_n^+}(z - z_n^+)\hat{z}, & \text{if } \bar{r} \in R_n^+, \\ -\frac{l_n}{A_n^-}(z - z_n^-)\hat{z}, & \text{if } \bar{r} \in R_n^-, \\ 0, & \text{otherwise} \end{cases} \quad (1.8)$$

where the superscript vv indicates that the basis function is defined for the vertical rectangular patches and for the vertical current components; A_n^+ and A_n^- are the areas of R_n^+ and R_n^- ; and, z_n^+ and z_n^- represent z -coordinates of opposite horizontal edges of R_n^+ and R_n^- .

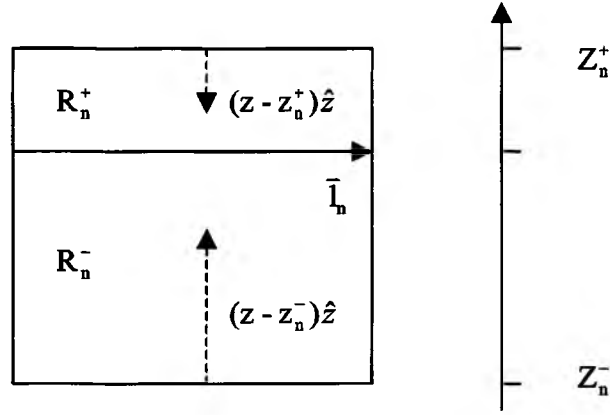


Figure 1.3. The basis function for vertical current component on rectangular mesh.

Similarly, for rectangular patches on vertical surfaces, the vector basis functions for horizontal current components are anchored by the vertical edges of rectangles. As illustrated in Figure 1.4, the n^{th} interior edge \bar{l}_n has a length l_n uniquely defined two adjacent rectangles R_n^+ and R_n^- . The plus or minus designation of the R is determined by the choice of a positive current reference direction for the n^{th} edge, the reference for which is assumed to be from R_n^+ to R_n^- . Thus the vector current basis function associated with this edge is

$$\bar{f}_n^{*v}(\bar{r}) = \begin{cases} \frac{1}{A_n^+}(\bar{r} - \bar{r}_n^+), & \text{if } \bar{r} \in R_n^+, \\ -\frac{1}{A_n^-}(\bar{r} - \bar{r}_n^-), & \text{if } \bar{r} \in R_n^-, \\ 0, & \text{otherwise} \end{cases} \quad (1.9)$$

where the superscript vh indicates that the basis function is defined for the vertical rectangular patches and for the horizontal current components; A_n^+ and A_n^- are the areas of R_n^+ and R_n^- ; and, \bar{r}_n^+ or \bar{r}_n^- represents the vectors from the origin to the point (p^+ or p^-) where a perpendicular line through the vertex of \bar{r} crosses the opposite vertical edges of R_n^+ or R_n^- .

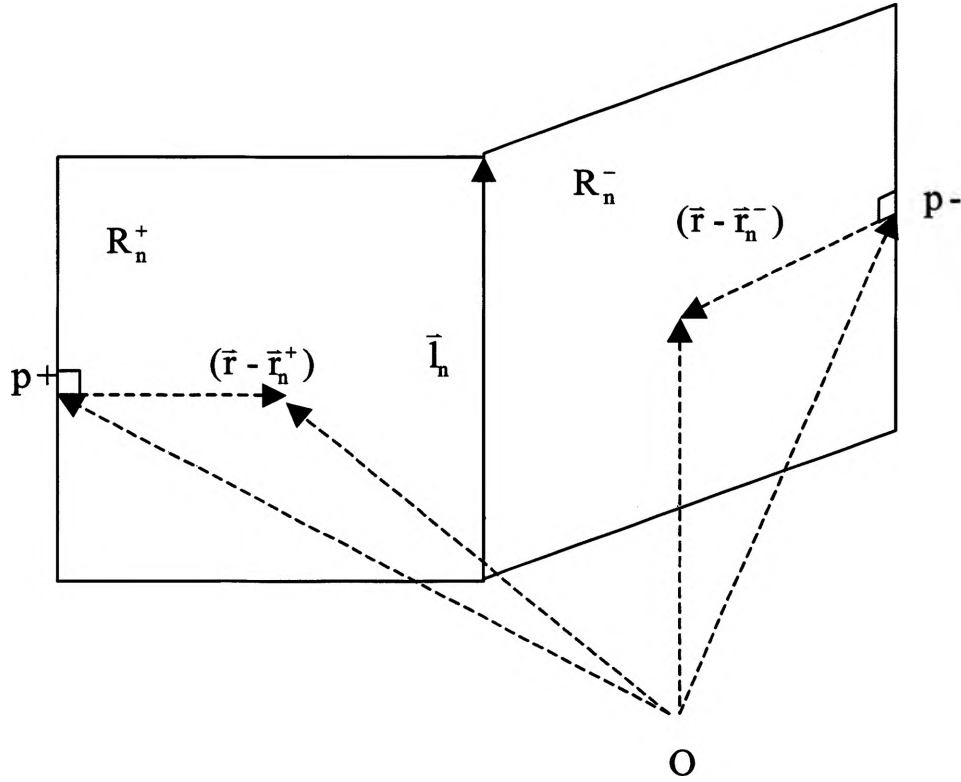


Figure 1.4. The basis function for horizontal current component on rectangular mesh.

The current basis functions have some important properties, which make them suitable for describing surface currents. First, the current has no component normal to the boundary of the surface. Second, the current component normal to the n^{th} edge is constant and continuous across the edge as may be seen in Figure 1.5. Hence, there is no line charge on any edge. Finally, the surface charge densities are constant over each patch, as can be shown by taking the surface divergence of these current basis functions.

Then induced current on both horizontal and vertical surfaces may be expanded in terms of the previously described basis functions as

$$\bar{J}(\bar{r}) = \bar{J}_h(\bar{r}) + \bar{J}_v(\bar{r}) = \sum_{n=1}^{M_1} \frac{i_n^h}{l_n} \bar{f}_n^h(\bar{r}) + \sum_{n=M_1+1}^{M_1+M_2} \frac{i_n^{vv}}{l_n} \bar{f}_n^{vv}(z) + \sum_{n=M_1+M_2+1}^{M_1+M_2+M_3} \frac{i_n^{vh}}{l_n} \bar{f}_n^{vh}(\bar{r}), \quad (1.10)$$

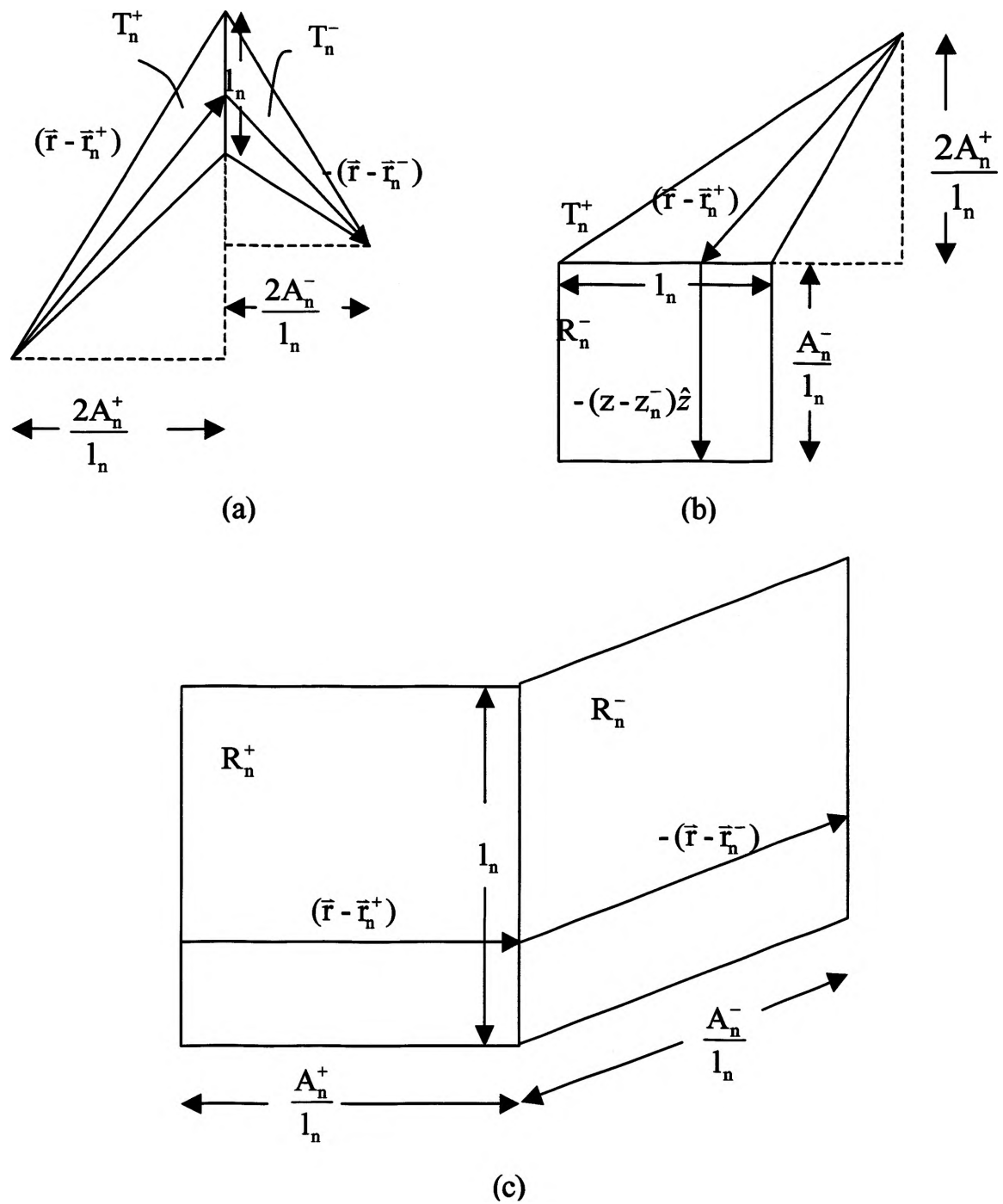


Figure 1.5. Geometry for evaluation of basis functions at the edge between two patches. (a) Two triangular patches, (b) One triangular and one rectangular patch, and (c) two rectangular patches.

where M_1 is the number of all inner edges of the triangle patches; M_2 is the number of all horizontal edges of the rectangular patches; and, M_3 is the number of all vertical edges of the rectangular patches. The dyadic Green's function $\overline{\overline{G}}^A(\vec{r}, \vec{r}')$ in (1.6) in layered media may be represented by [16],

$$\overline{\overline{G}}^A(\vec{r}, \vec{r}') = G_{xx}^A(\hat{x}\hat{x} + \hat{y}\hat{y}) + G_{zx}^A\hat{z}\hat{x} + G_{zy}^A\hat{z}\hat{y} + G_{zz}^A\hat{z}\hat{z}. \quad (1.11)$$

Substitution of (1.6), (1.9), and (1.10) yields

$$\begin{aligned} & \int_{s_1} G_{xx}^A(\vec{r}, \vec{r}') \bar{J}_h(\vec{r}') ds' + \int_{s_2} G_{xx}^A(\vec{r}, \vec{r}') \bar{J}_{vh}(\vec{r}') ds' \\ & + \frac{1}{j\omega} \nabla_{xy} \phi(\vec{r}) = 0, \quad \text{if } \vec{r} \in s_1. \end{aligned} \quad (1.12)$$

$$\begin{aligned} & \int_{s_1} (G_{zx}^A(\vec{r}, \vec{r}') J_x(\vec{r}') + G_{zy}^A(\vec{r}, \vec{r}') J_y(\vec{r}')) ds' \\ & + \int_{s_2} (G_{zx}^A(\vec{r}, \vec{r}') J_{vhx}(\vec{r}') + G_{zy}^A(\vec{r}, \vec{r}') J_{vhy}(\vec{r}')) ds' \\ & + \int_{s_2} G_{zz}^A(\vec{r}, \vec{r}') J_{vv}(z') ds' \\ & + \frac{1}{j\omega} \frac{\partial \phi(\vec{r})}{\partial z} = 0, \quad \text{if } \vec{r} \in s_2. \end{aligned} \quad (1.13)$$

$$\begin{aligned} & \left(\int_{s_1} (G_{xx}^A(\vec{r}, \vec{r}') \bar{J}_h(\vec{r}')) ds' \right. \\ & \quad \left. + \int_{s_2} (G_{xx}^A(\vec{r}, \vec{r}') \bar{J}_{vh}(\vec{r}')) ds' \right. \\ & \quad \left. + \frac{1}{j\omega} \nabla_{xy} \phi(\vec{r}) \right) |_{\text{tan}} = 0, \quad \text{if } \vec{r} \in s_2. \end{aligned} \quad (1.14)$$

Then (1.12), (1.13) and (1.14) are discretized by expanding the surface current densities using the basis function in (1.9). The next step is to select a testing procedure. The basis functions developed in this section are chosen as testing functions. Testing with $\bar{f}_m^h(\vec{r})$, (1.12) becomes

$$\begin{aligned} & j\omega \sum_{n=1}^{M_1} \frac{\bar{I}_n^h}{I_n} \langle G_{xx}^A \otimes \bar{f}_n^h(\vec{r}), \bar{f}_m^h(\vec{r}) \rangle + j\omega \sum_{n=M_1+M_2+1}^{M_1+M_2+M_3} \frac{\bar{I}_n^{vh}}{I_n} \langle G_{xx}^A \otimes \bar{f}_n^{vh}(\vec{r}), \bar{f}_m^h(\vec{r}) \rangle \\ & + \langle \nabla_{xy} \phi, \bar{f}_m^h(\vec{r}) \rangle = 0, \quad m = 1, \dots, M_1. \end{aligned} \quad (1.15)$$

where inner product $\langle a, b \rangle = \int (ab^*) ds$.

Similarly, when (1.13) is tested with $\bar{f}_m^{vv}(\vec{r})$,

$$\begin{aligned}
& j\omega \sum_{n=1}^{M_1} \frac{i_n^h}{l_n} (\langle \bar{G}_x^A \otimes \bar{f}_n^h(\bar{r}) \cdot \hat{x}, \bar{f}_m^v(\bar{r}) \rangle + \langle \bar{G}_y^A \otimes \bar{f}_n^h(\bar{r}) \cdot \hat{y}, \bar{f}_m^v(\bar{r}) \rangle) \\
& + j\omega \sum_{n=M_1+M_2+1}^{M_1+M_2+M_3} \frac{i_n^{vh}}{l_n} (\langle \bar{G}_x^A \otimes \bar{f}_n^{vh}(\bar{r}) \cdot \hat{x}, \bar{f}_m^v(\bar{r}) \rangle + \langle \bar{G}_y^A \otimes \bar{f}_n^{vh}(\bar{r}) \cdot \hat{y}, \bar{f}_m^v(\bar{r}) \rangle) \\
& + j\omega \sum_{n=M_1+1}^{M_1+M_2} \frac{i_n^{vv}}{l_n} (\langle G_x^A \otimes \bar{f}_n^{vv}(z), \bar{f}_m^v(\bar{r}) \rangle) \\
& + \langle \frac{\partial \phi(\bar{r})}{\partial z} \hat{z}, \bar{f}_m^v(\bar{r}) \rangle = 0, \quad m = M_1 + 1, \dots, M_1 + M_2.
\end{aligned} \tag{1.16}$$

Finally, when (1.14) is tested with $\bar{f}_m^{vh}(\bar{r})$,

$$\begin{aligned}
& j\omega \sum_{n=1}^{M_1} \frac{i_n^h}{l_n} \langle G_x^A \otimes \bar{f}_n^h(\bar{r}), \bar{f}_m^{vh}(\bar{r}) \rangle \\
& + j\omega \sum_{n=M_1+M_2+1}^{M_1+M_2+M_3} \frac{i_n^{vh}}{l_n} \langle G_x^A \otimes \bar{f}_n^{vh}(\bar{r}), \bar{f}_m^{vh}(\bar{r}) \rangle \\
& + \langle (\nabla_{xy} \phi(\bar{r}))|_{\text{in}}, \bar{f}_m^{vh}(\bar{r}) \rangle = 0, \quad m = M_1 + M_2 + 1, \dots, M_1 + M_2 + M_3.
\end{aligned} \tag{1.17}$$

From the definitions of the basis functions, it may be shown that

$$\begin{aligned}
& \langle \nabla_{xy} \phi, \bar{f}_m^h(\bar{r}) \rangle = -l_m (\phi(T_m^+) - \phi(T_m^-)), \\
& \quad m = 1, \dots, M_1, \\
& \langle \frac{\partial \phi(\bar{r})}{\partial z} \hat{z}, \bar{f}_m^v(\bar{r}) \rangle = -l_m (\phi(R_m^+) - \phi(R_m^-)), \\
& \quad m = m = M_1 + 1, \dots, M_1 + M_2, \\
& \langle (\nabla_{xy} \phi(\bar{r}))|_{\text{in}}, \bar{f}_m^{vh}(\bar{r}) \rangle = -l_m (\phi(R_m^+) - \phi(R_m^-)), \\
& \quad m = M_1 + M_2 + 1, \dots, M_1 + M_2 + M_3.
\end{aligned} \tag{1.18}$$

where ϕ is the unknown cell scalar electric potential, which is assumed to be constant with a cell. Combined (1.15), (1.16), (1.17), the matrix equation is

$$j\omega \begin{bmatrix} L^{h-h} & L^{h-vh} & 0 \\ L^{vh-h} & L^{vh-vh} & 0 \\ L^{vv-h} & L^{vv-vh} & L^{vv-vv} \end{bmatrix} \begin{bmatrix} i^h \\ i^{vh} \\ i^{vv} \end{bmatrix} - [\Lambda] \begin{bmatrix} \phi^h \\ \phi^v \end{bmatrix} = 0, \tag{1.19}$$

where

$$L_{mn}^{h-h} = \frac{1}{4}(M_{m^+n^-}^{h-h} - M_{m^+n^-}^{h-h} - M_{m^+n^-}^{h-h} + M_{m^+n^-}^{h-h}), \quad (1.20)$$

$$m, n = 1, \dots, M_1,$$

$$M_{m^+n^\pm}^{h-h} = \frac{1}{A_m A_n} \int_{x_m} ds \int_{x_n} ds' G_{xx}^A(\vec{r}, \vec{r}')((\vec{r} - \vec{r}_m^\pm) \cdot (\vec{r}' - \vec{r}_n^\pm)), \quad (1.21)$$

$$L_{mn}^{h-vh} = \frac{1}{2}(M_{m^+n^-}^{h-vh} - M_{m^+n^-}^{h-vh} - M_{m^+n^-}^{h-vh} + M_{m^+n^-}^{h-vh}), \quad (1.22)$$

$$m = 1, \dots, M_1, n = M_1 + M_2 + 1, \dots, M_1 + M_2 + M_3,$$

$$M_{m^+n^\pm}^{h-vh} = \frac{1}{A_m A_n} \int_{x_m} ds \int_{x_n} ds' [G_{xx}^A(\vec{r}, \vec{r}')((\vec{r} - \vec{r}_m^\pm) \cdot (\vec{r}' - \vec{r}_n^\pm))], \quad (1.23)$$

$$L_{mn}^{vv-h} = \frac{1}{2}(M_{m^+n^-}^{vv-h} - M_{m^+n^-}^{vv-h} - M_{m^+n^-}^{vv-h} + M_{m^+n^-}^{vv-h}), \quad (1.24)$$

$$m = M_1 + 1, \dots, M_1 + M_2, n = 1, \dots, M_1,$$

$$M_{m^+n^\pm}^{vv-h} = \frac{1}{A_m A_n} \int_{x_m} ds \int_{x_n} ds' (z - z_m^\pm) [G_{zx}^A(\vec{r}, \vec{r}')((\vec{r}' - \vec{r}_n^\pm) \cdot \hat{x})$$

$$+ G_{zy}^A(\vec{r}, \vec{r}')((\vec{r}' - \vec{r}_n^\pm) \cdot \hat{y})], \quad (1.25)$$

$$L_{mn}^{vv-vh} = (M_{m^+n^-}^{vv-vh} - M_{m^+n^-}^{vv-vh} - M_{m^+n^-}^{vv-vh} + M_{m^+n^-}^{vv-vh}), \quad (1.26)$$

$$m = M_1 + 1, \dots, M_1 + M_2, n = M_1 + M_2 + 1, \dots, M_1 + M_2 + M_3,$$

$$M_{m^+n^\pm}^{vv-vh} = \frac{1}{A_m A_n} \int_{x_m} ds \int_{x_n} ds' (z - z_m^\pm) [G_{zx}^A(\vec{r}, \vec{r}')((\vec{r}' - \vec{r}_n^\pm) \cdot \hat{x})$$

$$+ G_{zy}^A(\vec{r}, \vec{r}')((\vec{r}' - \vec{r}_n^\pm) \cdot \hat{y})], \quad (1.27)$$

$$L_{mn}^{vv-vv} = (M_{m^+n^-}^{vv-vv} - M_{m^+n^-}^{vv-vv} - M_{m^+n^-}^{vv-vv} + M_{m^+n^-}^{vv-vv}), \quad (1.28)$$

$$m = M_1 + 1, \dots, M_1 + M_2, n = M_1 + 1, \dots, M_1 + M_2,$$

$$M_{m^{\pm}n^{\pm}}^{v-v} = \frac{1}{A_m A_n} \int_{\mathbf{r}_m} ds \int_{\mathbf{r}_n} ds' [G_z^A(z - z_n^{\pm})(z' - z_n^{\pm})], \quad (1.29)$$

$$L_{mn}^{v-h} = \frac{1}{2} (M_{m^+n^-}^{v-h} - M_{m^-n^+}^{v-h} - M_{m^+n^+}^{v-h} + M_{m^-n^-}^{v-h}), \quad (1.30)$$

$$m = M_1 + M_2 + 1, \dots, M_1 + M_2 + M_3, n = 1, \dots, M_1,$$

$$M_{m^{\pm}n^{\pm}}^{v-h} = \frac{1}{A_m A_n} \int_{\mathbf{r}_m} ds \int_{\mathbf{r}_n} ds' [G_{xx}^A(\bar{\mathbf{r}}, \bar{\mathbf{r}}')((\bar{\mathbf{r}} - \bar{\mathbf{r}}_m^{\pm}) \cdot (\bar{\mathbf{r}}' - \bar{\mathbf{r}}_n^{\pm}))], \quad (1.31)$$

$$L_{mn}^{v-vh} = (M_{m^+n^-}^{v-h} - M_{m^-n^+}^{v-h} - M_{m^+n^+}^{v-h} + M_{m^-n^-}^{v-h}), \quad (1.32)$$

$$m = M_1 + M_2 + 1, \dots, M_1 + M_2 + M_3,$$

$$n = M_1 + M_2 + 1, \dots, M_1 + M_2 + M_3,$$

$$M_{m^{\pm}n^{\pm}}^{v-vh} = \frac{1}{A_m A_n} \int_{\mathbf{r}_m} ds \int_{\mathbf{r}_n} ds' [G_{xx}^A(\bar{\mathbf{r}}, \bar{\mathbf{r}}')((\bar{\mathbf{r}} - \bar{\mathbf{r}}_m^{\pm}) \cdot (\bar{\mathbf{r}}' - \bar{\mathbf{r}}_n^{\pm}))], \quad (1.33)$$

The connectivity matrix Λ defines the connectivity between edge-wise quantities and cell-wise quantities. Its elements are determined by

$$\Lambda_{\alpha n} = \begin{cases} 1, & \text{if Cell } n \text{ is Edge } \alpha \text{'s positive side;} \\ -1, & \text{if Cell } n \text{ is Edge } \alpha \text{'s negative side;} \\ 0, & \text{otherwise.} \end{cases} \quad (1.34)$$

On the other hand, nodal currents can be defined as total currents flowing out of the corresponding mesh cells. This means that

$$j\omega \begin{bmatrix} Q^h \\ Q^v \end{bmatrix} = \begin{bmatrix} I^h \\ I^v \end{bmatrix} + \begin{bmatrix} I^{eh} \\ I^{ev} \end{bmatrix}, \quad (1.35)$$

where Q^h , Q^v , I and I^e are the charge, the induced current and the impressed current associated with a cell, respectively. Then, the surface electric potential is related to the surface charge density by the scalar electric potential Green's functions as

$$\begin{aligned}\phi &= \int_{S_1} \sigma^h G_x^e(\bar{r}, \bar{r}') ds' + \int_{S_2} \sigma^v G_z^e(\bar{r}, \bar{r}') ds' \\ &= \int_{S_1} \sum_{n=1}^{N_1} \frac{Q_n^h}{A_n} \delta_n(\bar{r}') G_x^e(\bar{r}, \bar{r}') ds' + \int_{S_2} \sum_{n=N_1+1}^{N_1+N_2} \frac{Q_n^v}{A_n} \delta_n(\bar{r}') G_z^e(\bar{r}, \bar{r}') ds'\end{aligned}\quad (1.36)$$

where N_1 and N_2 are number of triangle and rectangle cells, respectively; $\delta_n(\bar{r}')$ is a pulse basis function.

$$\delta_n(\bar{r}') = \begin{cases} 1, & \bar{r}' \text{ in cell } n \\ 0, & \text{elsewhere} \end{cases} \quad (1.37)$$

The matrix-equation expression of (1.36) is

$$\begin{bmatrix} \phi^h \\ \phi^v \end{bmatrix} = \begin{bmatrix} K^{hh} & K^{hv} \\ K^{vh} & K^{vv} \end{bmatrix} \begin{bmatrix} Q^h \\ Q^v \end{bmatrix}, \quad (1.38)$$

where

$$\begin{aligned}K^{hh} &= \frac{1}{A_p A_q} \int_{\mathcal{R}_p} \int_{\mathcal{R}_q} G_x^e(\bar{r}, \bar{r}') ds' ds, \\ K^{vh} &= \frac{1}{A_p A_q} \int_{\mathcal{R}_p} \int_{\mathcal{R}_q} G_x^e(\bar{r}, \bar{r}') ds' ds, \\ K^{hv} &= \frac{1}{A_p A_q} \int_{\mathcal{R}_p} \int_{\mathcal{R}_q} G_z^e(\bar{r}, \bar{r}') ds' ds, \\ K^{vv} &= \frac{1}{A_p A_q} \int_{\mathcal{R}_p} \int_{\mathcal{R}_q} G_z^e(\bar{r}, \bar{r}') ds' ds.\end{aligned}\quad (1.39)$$

1.2.3. Partial Element Equivalent Circuit Extraction. The inductance between two current loops, i and j , is proportional to the magnetic flux in loop i due to the current in loop j . If loop i is assumed to consist of N segments while the loop j is divided into M segments, the total inductance can be expressed as the summation of the partial inductances. Generally, the partial inductance of the n^{th} segment due to current flow in the m^{th} segment may be defined as an average value over the cross section of the n^{th} segment, i.e.,

$$L_{mn} = \frac{1}{a_m a_n} \int_{\Omega_m} dV \int_{\Omega_n} dV' \bar{f}_m(\vec{r}) \cdot \bar{\bar{G}}^A(\vec{r}, \vec{r}') \cdot \bar{f}_n(\vec{r}'). \quad (1.40)$$

where Ω_m and a_m are the volume and cross section area of the m^{th} segment, respectively. $\bar{\bar{G}}^A(\vec{r}, \vec{r}')$ is a dyadic Green's function for the vector magnetic potential, and $\bar{f}_m(\vec{r})$ is the current distribution function over a_m .

Similarly, the partial capacitance matrix with normalized potential coefficients [C] can be defined through its inverse matrix [K], having elements of

$$K_{mn} = \frac{1}{A_m A_n} \int_{S_m} ds \int_{S_n} ds' G^\phi(\vec{r}, \vec{r}'). \quad (1.41)$$

where $G^\phi(\vec{r}, \vec{r}')$ is a scalar Green's function for the scalar electric potential, S_m is the surface of the m^{th} segment, and A_m is the area of S_m .

Comparing (1.20) - (1.33) and (1.38) with the definition of partial inductance and partial capacitance, it is may be found that [L] is a partial inductance matrix with normalized potential coefficients and [K] is an inverse partial capacitive matrix with normalized potential coefficients.

Combining (1.19) and (1.35) results in

$$\begin{bmatrix} j\omega L & -\Lambda \\ \Lambda^T & j\omega K^{-1} \end{bmatrix} \begin{bmatrix} i \\ \phi \end{bmatrix} = \begin{bmatrix} 0 \\ -I^e \end{bmatrix}. \quad (1.42)$$

The pure relationship between the node potentials and the impressed node currents may be derived from (1.42), i.e.,

$$\begin{aligned}
[Y][\phi] &= \left(\frac{1}{j\omega} [\Lambda^T L^{-1} \Lambda] + j\omega [K^{-1}] \right) [\phi] \\
&= [-I^e].
\end{aligned} \tag{1.43}$$

Instead of directly solving the MOM matrix equation, an equivalent circuit model is extracted from the admittance matrix $[Y]$. At an arbitrary Node m , the impressed node current is

$$\begin{aligned}
I_m^e &= \sum_n Y_{mn} \phi_n \\
&= \sum_n Y_{mn} (\phi_n - \phi_m) + \sum_n Y_{mn} (\phi_m - 0).
\end{aligned} \tag{1.44}$$

At the same time, Kirchhoff's Current Law (KCL) require the sum of currents at every node is 0, i.e.,

$$I_m^e = - \sum_{n \neq m} Y'_{mn} (\phi_n - \phi_m) + Y'_{m0} (\phi_m - 0). \tag{1.45}$$

Comparing (1.44) and (1.45) results in

$$\begin{aligned}
Y'_{mn} &= -Y_{mn}, & m \neq n \text{ and } n \neq 0, \\
Y'_{m0} &= \sum_n Y_{mn} & m \neq 0.
\end{aligned} \tag{1.46}$$

The admittance of an equivalent circuit branch, Y'_{mn} determines the values of the equivalent circuit directly. Since the Y matrix is the sum of an inductive part and a capacitive part, every branch is a parallel LC circuit, while the branch from a node to a reference point (ground or infinity) is a capacitor as shown in Figure 1.6.

The entries in the L and C matrices are functions of vector- or scalar- potential Green's functions, which are frequency dependent. Hence the circuit extracted from (1.46) is frequency dependent, making the circuit simulation difficult and time-consuming. A quasi-static approximation of the Green's functions is employed to overcome this problem. Then the values of extracted inductance and capacitance are constant over frequency. When frequency is very high, the quasi-static approximation causes a large condition number of the impedance matrix at some frequencies and the simulation accuracy is degraded. It may be cured by a proper definition of the far cell distance. Any reaction between two cells that have the distance larger than the far cell distance is ignored.

After the quasi-static approximation, the matrix $[K]$ is symmetric, but $[L]$ is asymmetric. This results in asymmetry in $[Y]$ (the circuit matrix whose entries are Y_{mn} 's) that is required by circuit reciprocity. Let

$$L_{ij,restored} = L_{ji,restored} = \frac{L_{ij} + L_{ji}}{2}. \quad (1.47)$$

The non-diagonal entries in the $[L]$ matrix are averaged so that the symmetry of the $[L]$ matrix, as well as the $[Y]$ matrix, is restored [17].

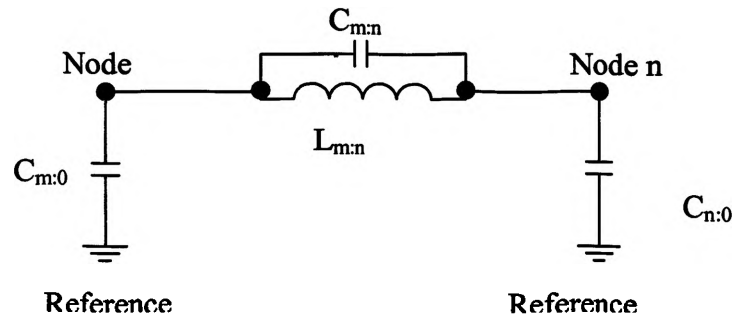


Figure 1.6. A typical circuit between any pair of two nodes m and n.

1.2.4. Calculation of Green's Functions. The calculation of Green's functions for a multi-layer media has been well studied by implementation of complex-image theory [18] - [20]. The spectral-domain Green's functions for multi-layer media can be derived from the solution of one-dimensional (plane wave) problems, assuming the horizontal dimension of dielectric layers are infinite.

The inverse 2-D Fourier transform (Hankel transform, Fourier-Bessel transform) is given by the Sommerfield identity as

$$\frac{e^{-jk_r r}}{4\pi r} = \frac{1}{4\pi} \int_0^\infty k_\rho dk_\rho H_0^{(2)}(k_\rho \rho) \frac{e^{-jk_z |z|}}{2jk_z}, \quad (1.48)$$

i.e.

$$\frac{e^{-jkr}}{4\pi r} = F^{-1}\left(\frac{e^{-jk_z|z|}}{2jk_z}\right). \quad (1.49)$$

Then the generalized pencil of function (GPOF) method is used to approximate the spectral-domain expressions of Green's functions as a series of complex images

$$\tilde{G} = \frac{1}{2\gamma} \sum_{p=1}^M \alpha_p e^{\gamma\beta_p}. \quad (1.50)$$

The spatial-domain expression of the Green's functions may be obtained by using the Sommerfield identity and

$$G = \sum_{p=1}^M \alpha_p \frac{e^{-jk\sqrt{x^2+y^2+\beta_p^2}}}{4\pi\sqrt{x^2+y^2+\beta_p^2}}. \quad (1.51)$$

When the point source is embedded in Layer p of multi-layer media and the field point is in the same layer, the spectral-domain expression of Green's functions are

$$\begin{aligned} \tilde{G}_{xx}^{A(pp)} = & \frac{\mu_p}{2\gamma_p} \{e^{-\gamma_p|z-z'|} + \tilde{M}_p^{TE} [\tilde{R}_{p+}^{TE} e^{-\gamma_p(2h_{p-1}-z-z')} \\ & + \tilde{R}_{p-}^{TE} e^{-\gamma_p(-2h_p+z+z')} + \tilde{R}_{p+}^{TE} \tilde{R}_{p-}^{TE} (e^{-\gamma_p(2d_p+z-z')} + e^{-\gamma_p(2d_p-z+z')})]\}, \end{aligned} \quad (1.52)$$

where h_{p-1} is the z coordinate of the interface between Layer p and Layer $p-1$; d_p is the thickness of Layer p ; the \tilde{R}_{p+}^{TE} and \tilde{R}_{p-}^{TE} are the generalized reflection coefficients for TE mode plane wave in multi-layer media; and,

$$\tilde{M}_p^{TE} = [1 - \tilde{R}_{p+}^{TE} \tilde{R}_{p-}^{TE} e^{-\gamma_p(2d_p)}]^{-1}. \quad (1.53)$$

$$\begin{aligned} \tilde{G}_{xx}^{A(pp)} = & \frac{\mu_p k_x}{j2k_p^2} \{ \tilde{M}_p^{TM} [-\tilde{R}_{p+}^{TM} e^{-\gamma_p(2h_{p-1}-z-z')} \\ & + \tilde{R}_{p-}^{TM} e^{-\gamma_p(-2h_p+z+z')} + \tilde{R}_{p+}^{TM} \tilde{R}_{p-}^{TM} (e^{-\gamma_p(2d_p-z+z')} - e^{-\gamma_p(2d_p+z-z')})] \\ & + \tilde{M}_p^{TE} [-\tilde{R}_{p+}^{TE} e^{-\gamma_p(2h_{p-1}-z-z')} \\ & + \tilde{R}_{p-}^{TE} e^{-\gamma_p(-2h_p+z+z')} + \tilde{R}_{p+}^{TE} \tilde{R}_{p-}^{TE} (e^{-\gamma_p(2d_p+z-z')} - e^{-\gamma_p(2d_p-z+z')})]\}, \end{aligned} \quad (1.54)$$

$$\begin{aligned}
\tilde{G}_h^{\phi(pp)} = & \frac{1}{j\varepsilon_p\gamma_p} \{e^{-\gamma_p|z-z'|} + \tilde{M}_p^{TE} \frac{\omega^2\varepsilon_p\mu_p}{\omega^2\varepsilon_p\mu_p + \gamma_p^2} [\tilde{R}_{p+}^{TE} e^{-\gamma_p(2h_{p-1}-z-z')} \\
& + \tilde{R}_{p-}^{TE} e^{-\gamma_p(-2h_p+z+z')} + \tilde{R}_{p+}^{TE}\tilde{R}_{p-}^{TE} (e^{-\gamma_p(2d_p+z-z')} + e^{-\gamma_p(2d_p-z+z')})] \\
& - \tilde{M}_p^{TM} \frac{\gamma_p^2}{\omega^2\varepsilon_p\mu_p + \gamma_p^2} [\tilde{R}_{p+}^{TM} e^{-\gamma_p(2h_{p-1}-z-z')} \\
& + \tilde{R}_{p-}^{TM} e^{-\gamma_p(-2h_p+z+z')} - \tilde{R}_{p+}^{TM}\tilde{R}_{p-}^{TM} (e^{-\gamma_p(2d_p+z-z')} - e^{-\gamma_p(2d_p-z+z')})]\},
\end{aligned} \tag{1.55}$$

$$\begin{aligned}
\tilde{G}_z^{A(pp)} = & \frac{\mu_p}{2\gamma_p} \{e^{-\gamma_p|z-z'|} + \tilde{M}_p^{TM} [\tilde{R}_{p+}^{TM} e^{-\gamma_p(2h_{p-1}-z-z')} \\
& + \tilde{R}_{p-}^{TM} e^{-\gamma_p(-2h_p+z+z')} + \tilde{R}_{p+}^{TM}\tilde{R}_{p-}^{TM} (e^{-\gamma_p(2d_p-z+z')} + e^{-\gamma_p(2d_p+z-z')})]\},
\end{aligned} \tag{1.56}$$

$$\begin{aligned}
\tilde{G}_v^{\phi(pp)} = & \frac{1}{2\varepsilon_p\gamma_p} \{e^{-\gamma_p|z-z'|} + \tilde{M}_p^{TM} [-\tilde{R}_{p+}^{TM} e^{-\gamma_p(2h_{p-1}-z-z')} \\
& - \tilde{R}_{p-}^{TM} e^{-\gamma_p(-2h_p+z+z')} + \tilde{R}_{p+}^{TM}\tilde{R}_{p-}^{TM} (e^{-\gamma_p(2d_p-z+z')} - e^{-\gamma_p(2d_p+z-z')})]\}.
\end{aligned} \tag{1.57}$$

If the source and field points are in different dielectric layers, the derivation of the spectral-domain expressions for the Green's functions needs to apply the concept of the generalized transmission coefficients. When the field point is in Layer i , the source point is in Layer p , and $i < p$, the components of Green's functions are

$$\begin{aligned}
\tilde{G}_{xx}^{A(ip)} = & \frac{\mu_i}{2\gamma_p} \tilde{T}_{pi}^{TE} \tilde{M}_p^{TE} [e^{-\gamma_p(-h_i+z)} \\
& + \tilde{R}_{i-}^{TE} e^{-\gamma_i(-2h_{i-1}-h_i-z)}] [e^{-\gamma_p(h_{p-1}-z')} + \tilde{R}_{p-}^{TE} e^{-\gamma_p(h_{p-1}-2h_p+z')}],
\end{aligned} \tag{1.58}$$

$$\begin{aligned}
\tilde{G}_{zx}^{A(ip)} = & \frac{\mu_p}{j2\gamma_p} \frac{k_x}{\omega^2\varepsilon_p\mu_p + \gamma_p^2} \{\gamma_p \tilde{T}_{pi}^{TM} \tilde{M}_p^{TM} [e^{-\gamma_i(-h_i+z)} \\
& + \tilde{R}_{i-}^{TM} e^{-\gamma_i(2h_{i-1}-h_i-z)}] [e^{-\gamma_p(-h_{p-1}-z')} + \tilde{R}_{p-}^{TM} e^{-\gamma_p(h_{p-1}-2h_p+z')}] \\
& - \gamma_i \tilde{T}_{pi}^{TE} \tilde{M}_p^{TE} \frac{\mu_i}{\mu_p} [-e^{-\gamma_i(-h_i+z)} + \tilde{R}_{i+}^{TE} e^{-\gamma_i(2h_{i-1}-h_i-z)}] \\
& [e^{-\gamma_p(h_{p-1}-z')} + \tilde{R}_{p-}^{TE} e^{-\gamma_p(h_{p-1}-2h_p+z')}]\},
\end{aligned} \tag{1.59}$$

$$\begin{aligned}
\tilde{G}_h^{\phi(ip)} = & \frac{1}{j\varepsilon_p\gamma_p} \frac{1}{\omega^2\varepsilon_i\mu_i + \gamma_i^2} \left\{ \tilde{T}_{pi}^{TE} \tilde{M}_p^{TE} \frac{\omega^2\varepsilon_i\mu_i^2}{\mu_p} [e^{-\gamma_i(-h_i+z)} \right. \\
& + \tilde{R}_{i+}^{TE} e^{-\gamma_i(-2h_{i-1}-h_i-z)}] [e^{-\gamma_p(2h_{p-1}-z')} + \tilde{R}_{p-}^{TE} e^{-\gamma_p(h_{p-1}-2h_p+z')}] \\
& + \gamma_p\gamma_i \tilde{T}_{pi}^{TM} \tilde{M}_p^{TM} [-e^{-\gamma_i(-h_i+z)} \\
& \left. + \tilde{R}_{i+}^{TM} e^{-\gamma_i(-2h_{i-1}-h_i-z)}] [-e^{-\gamma_p(h_{p-1}-z')} + \tilde{R}_{p-}^{TM} e^{-\gamma_p(h_{p-1}-2h_p+z')}] \right\}, \tag{1.60}
\end{aligned}$$

$$\begin{aligned}
\tilde{G}_{zz}^{A(ip)} = & \frac{\mu_i}{2\gamma_p} \tilde{T}_{pi}^{TM} \tilde{M}_p^{TM} [e^{-\gamma_p(-h_{p-1}-z')} \\
& + \tilde{R}_{p-}^{TM} e^{-\gamma_p(h_{p-1}-2h_p+z')}] [e^{-\gamma_i(-h_i+z)} + \tilde{R}_{i+}^{TM} e^{-\gamma_i(2h_{i-1}-h_i-z)}], \tag{1.61}
\end{aligned}$$

$$\begin{aligned}
\tilde{G}_v^{\phi(ip)} = & -\frac{\gamma_i}{2\varepsilon_p\gamma_p} \tilde{T}_{pi}^{TM} \tilde{M}_p^{TM} [e^{-\gamma_p(h_{p-1}-z')} \\
& - \tilde{R}_{p-}^{TM} e^{-\gamma_p(h_{p-1}-2h_p+z')}] [-e^{-\gamma_i(-h_i+z)} + \tilde{R}_{i+}^{TM} e^{-\gamma_i(2h_{i-1}-h_i-z)}]. \tag{1.62}
\end{aligned}$$

When the field point is in Layer j , the source point is in Layer p , and $j > p$, the components of Green's functions are

$$\begin{aligned}
\tilde{G}_{xx}^{A(jp)} = & \frac{\mu_j}{2\gamma_p} \tilde{T}_{pj}^{TE} \tilde{M}_p^{TE} [e^{-\gamma_j(-h_{j-1}-z)} \\
& + \tilde{R}_{j-}^{TE} e^{-\gamma_j(h_{j-1}-2h_j+z)}] [e^{-\gamma_p(-h_p+z')} + \tilde{R}_{p-}^{TE} e^{-\gamma_p(2h_{p-1}-h_p-z')}], \tag{1.63}
\end{aligned}$$

$$\begin{aligned}
\tilde{G}_{zx}^{A(jp)} = & \frac{\mu_p}{j2\gamma_p} \frac{k_x}{\omega^2\varepsilon_p\mu_p + \gamma_p^2} \left\{ \gamma_p \tilde{T}_{pj}^{TM} \tilde{M}_p^{TM} [e^{-\gamma_j(-h_{j-1}-z)} \right. \\
& + \tilde{R}_{j-}^{TM} e^{-\gamma_j(2h_{j-1}-2h_j+z)}] [e^{-\gamma_p(-h_p+z')} - \tilde{R}_{p+}^{TM} e^{-\gamma_p(2h_{p-1}-h_p-z')}] \\
& - \gamma_j \tilde{T}_{pj}^{TE} \tilde{M}_p^{TE} \frac{\mu_j}{\mu_p} [-e^{-\gamma_j(h_{j-1}-z)} - \tilde{R}_{j-}^{TE} e^{-\gamma_j(h_{j-1}-2h_j+z)}] \\
& \left. [e^{-\gamma_p(-h_p+z')} + \tilde{R}_{p+}^{TE} e^{-\gamma_p(2h_{p-1}-h_p-z')}] \right\}, \tag{1.64}
\end{aligned}$$

$$\begin{aligned}
\tilde{G}_h^{\phi(jp)} = & \frac{1}{2\varepsilon_p \gamma_p} \frac{1}{\omega^2 \varepsilon_j \mu_j + \gamma_j^2} \left\{ \tilde{T}_{pj}^{TE} \tilde{M}_p^{TE} \frac{\omega^2 \varepsilon_j \mu_j^2}{\mu_p} [e^{-\gamma_j(h_{j-1}-z)} \right. \\
& + \tilde{R}_{j-}^{TE} e^{-\gamma_j(h_{j-1}-2h_j+z)}][e^{-\gamma_p(-h_p+z')} + \tilde{R}_{p+}^{TE} e^{-\gamma_p(2h_{p-1}-h_p-z')}] \\
& + \gamma_p \gamma_j \tilde{T}_{pj}^{TM} \tilde{M}_p^{TM} [-e^{-\gamma_j(-h_{j-1}-z)} \\
& \left. - \tilde{R}_{j-}^{TM} e^{-\gamma_j(h_{j-1}-2h_j+z)}][-e^{-\gamma_p(-h_p+z')} - \tilde{R}_{p+}^{TM} e^{-\gamma_p(2h_{p-1}-h_p-z')}] \right\}, \tag{1.65}
\end{aligned}$$

$$\begin{aligned}
\tilde{G}_z^{A(ip)} = & \frac{\mu_p}{2\gamma_p} \tilde{T}_{pj}^{TM} \tilde{M}_p^{TM} [e^{-\gamma_p(-h_p+z')} \\
& + \tilde{R}_{p+}^{TM} e^{-\gamma_p(2h_{p-1}-h_p-z')}] [e^{-\gamma_j(h_{j-1}-z)} + \tilde{R}_{j-}^{TM} e^{-\gamma_j(h_{j-1}-2h_j+z)}], \tag{1.66}
\end{aligned}$$

$$\begin{aligned}
\tilde{G}_v^{\phi(jp)} = & -\frac{\gamma_j}{2\varepsilon_p \gamma_p^2} \tilde{T}_{pj}^{TM} \tilde{M}_p^{TM} [-e^{-\gamma_p(-h_p+z')} \\
& - \tilde{R}_{p+}^{TM} e^{-\gamma_p(2h_{p-1}-h_p-z')}] [e^{-\gamma_j(h_{j-1}-z)} - \tilde{R}_{j-}^{TM} e^{-\gamma_j(h_{j-1}-2h_j+z)}], \tag{1.67}
\end{aligned}$$

1.2.5. Analytic Integration of Some Components of the Green's Functions.

The spectral-domain expressions of Green's functions are the functions of z and z' . If the source point is on a vertical surface, z varies within the appropriate cell. Similarly if the field point is on a vertical surface, z' varies within the appropriate cell. The spectral-domain Green's functions have to be calculated and the inverse Fourier transform needs to be performed for every combination of z and z' . The computational burden will be very large. The solution is to carry out the integration of the spectral domain Green's functions multiplied with the test and/or basis functions, which can be implemented analytically over z and/or z' . So the inverse Fourier transform needs to be performed only once for every vertical cell.

If

$$\int \mathcal{F}^{-1}(\tilde{f}_n(\vec{r}) \otimes (\tilde{G} \cdot \tilde{f}_n(\vec{r}')))) ds \tag{1.68}$$

is uniformly convergent, the order of integration of inner product terms

$$\langle G \otimes \tilde{f}_n(\vec{r}'), \tilde{f}_n(\vec{r}) \rangle \tag{1.69}$$

can be interchanged. It has been proved that (1.68) is uniformly convergent when the expansion and testing functions satisfy the following criteria: (i) In the direction of the polarization of the current, the sum of the order of the differentiability of the expansion

and the testing functions must be equal to or greater than one; (ii) in the orthogonal direction of the polarization of the current, any piecewise continuous function or even functions with singularities of the order of less than one are admissible [21] [22]. The basis functions for a vertical surface are rooftop basis functions, consisting of a triangular function in the direction of polarization and a pulse function in the direction orthogonal to the polarization of the current. Similarly, it can be shown that the RWG basis functions used for a horizontal surface have the same property. Therefore the order of integration of (1.69) can be interchanged. The spectral domain Green's functions are integrated over z direction and cast into closed form via the Sommerfield identity.

The analytic integration results for the quasi-static approximation are listed below:

$$2\gamma \int_{z_{q1}}^{z_{q2}} \tilde{G}_z^*(\vec{r}, \vec{r}') dz' = \begin{cases} F_1(z, z_{q2}) - F_1(z, z_{q1}) + SF_1, & i = p, \\ F_1(z, z_{q2}) - F_1(z, z_{q1}), & i \neq p. \end{cases} \quad (1.70)$$

When the source and the field points are in the same dielectric Layer i ,

$$F_1(z, z') = \begin{cases} \frac{\tilde{M}_i^{TM}}{\epsilon_i \gamma} [-\tilde{R}_{i+}^{TM} e^{-\gamma(2h_{i-1}-z-z')} + \tilde{R}_{i-}^{TM} e^{-\gamma(-2h_i+z+z')} + \tilde{R}_{i+}^{TM} \tilde{R}_{i-}^{TM} (e^{-\gamma(2d_i-z+z')} + e^{-\gamma(2d_i+z-z')})], & \gamma \neq 0, \\ \frac{1}{\epsilon_i} z' [1 - \tilde{M}_i^{TM} (\tilde{R}_{i+}^{TM} + \tilde{R}_{i-}^{TM} - 2\tilde{R}_{i+}^{TM} \tilde{R}_{i-}^{TM})], & \gamma = 0. \end{cases} \quad (1.71)$$

$$SF_1 = \begin{cases} \frac{1}{\epsilon_i \gamma} (e^{-\gamma(z_{q1}-z)} - e^{-\gamma(z_{q2}-z)}), & z_{q1} \geq z \quad \text{and} \quad \gamma \neq 0 \\ \frac{1}{\epsilon_i \gamma} (e^{-\gamma(z-z_{q2})} - e^{-\gamma(z-z_{q1})}), & z_{q2} \leq z \quad \text{and} \quad \gamma \neq 0 \\ \frac{1}{\epsilon_i \gamma} (2 - e^{-\gamma(z-z_{q1})} - e^{-\gamma(z_{q2}-z)}), & z_{q1} < z < z_{q2} \quad \text{and} \quad \gamma \neq 0 \\ 0, & \gamma = 0 \end{cases} \quad (1.72)$$

When the field point is in Layer i , the source point is in Layer p , and $i < p$,

$$F_1(z, z') = \begin{cases} \frac{\tilde{T}_{pi}^{TM} \tilde{M}_p^{TM}}{\varepsilon_p \gamma} [e^{-\gamma(2h_{p-1}-z')} + \tilde{R}_{p-}^{TM} e^{-\gamma(h_{p-1}-2h_p+z')}] \\ [e^{-\gamma(-h_i+z)} - \tilde{R}_{i+}^{TM} e^{-\gamma(2h_{i-1}-h_i-z)}], & \gamma \neq 0, \\ \frac{1}{\varepsilon_p} z' \tilde{T}_{pi}^{TM} \tilde{M}_p^{TM} [1 - \tilde{R}_{p+}^{TM}] [1 - \tilde{R}_{i+}^{TM}], & \gamma = 0. \end{cases} \quad (1.73)$$

When the field point is in Layer j , the source point is in Layer p , and $j > p$,

$$F_1(z, z') = \begin{cases} -\frac{\tilde{T}_{pj}^{TM} \tilde{M}_p^{TM}}{\varepsilon_p \gamma} [e^{-\gamma(2h_{j-1}-z)} - \tilde{R}_{j-}^{TM} e^{-\gamma(h_{j-1}-2h_j+z)}] \\ [e^{-\gamma(-h_p+z')} - \tilde{R}_{p+}^{TM} e^{-\gamma(2h_{p-1}-h_p-z')}], & \gamma \neq 0, \\ \frac{1}{\varepsilon_p} z' \tilde{T}_{pj}^{TM} \tilde{M}_p^{TM} [1 - \tilde{R}_{j+}^{TM}] [1 - \tilde{R}_{p+}^{TM}], & \gamma = 0. \end{cases} \quad (1.74)$$

$$2\gamma \int_{z_{p1}}^{z_{p2}} \int_{z_{q1}}^{z_{q2}} \tilde{G}_z^\phi(\vec{r}, \vec{r}') dz' dz = \begin{cases} F_2(z_{p2}, z_{q2}) - F_2(z_{p2}, z_{q1}) \\ -F_2(z_{p1}, z_{q2}) + F_2(z_{p1}, z_{q1}) + SF_2, & i = p, \\ F_2(z_{p2}, z_{q2}) - F_2(z_{p2}, z_{q1}) \\ -F_2(z_{p1}, z_{q2}) + F_2(z_{p1}, z_{q1}), & i \neq p. \end{cases} \quad (1.75)$$

When the source and the field points are in the same dielectric Layer i , the assistant integral functions are

$$F_2(z, z') = \begin{cases} \frac{\tilde{M}_i^{TM}}{\varepsilon_i \gamma^2} [-\tilde{R}_{i+}^{TM} e^{-\gamma(2h_{i-1}-z-z')} + \tilde{R}_{i-}^{TM} e^{-\gamma(-2h_i+z+z')}] \\ \tilde{R}_{i+}^{TM} \tilde{R}_{i-}^{TM} (-e^{-\gamma(2d_i-z+z')} - e^{-\gamma(2d_i+z-z')}], & \gamma \neq 0, \\ \frac{1}{\varepsilon_i} z z' [1 - \tilde{M}_i^{TM} (\tilde{R}_{i+}^{TM} + \tilde{R}_{i-}^{TM} - 2\tilde{R}_{i+}^{TM} \tilde{R}_{i-}^{TM})], & \gamma = 0. \end{cases} \quad (1.76)$$

$$SF_2 = \begin{cases} \frac{1}{\varepsilon_i \gamma^2} (e^{-\gamma(z_{q2}-z_{p1})} + e^{-\gamma(z_{q1}-z_{p2})}) \\ -e^{-\gamma(z_{q2}-z_{p2})} - e^{-\gamma(z_{q1}-z_{p1})}), & z_{q2} > z_{p2} \quad \text{and} \quad \gamma \neq 0, \\ \frac{1}{\varepsilon_i \gamma^2} (e^{-\gamma(z_{p2}-z_{q1})} + e^{-\gamma(z_{p1}-z_{q2})}) \\ -e^{-\gamma(z_{p2}-z_{q2})} - e^{-\gamma(z_{p1}-z_{q1})}), & z_{q2} < z_{p2} \quad \text{and} \quad \gamma \neq 0, \\ \frac{2}{\varepsilon_i \gamma} (z_{p2} - z_{p1}) + \frac{1}{\varepsilon_i \gamma^2} (e^{-\gamma(z_{p2}-z_{q1})} - e^{-\gamma(z_{p1}-z_{q1})}) \\ -e^{-\gamma(z_{q2}-z_{p2})} + e^{-\gamma(z_{q2}-z_{p1})}), & z_{q1} = z_{q2} \quad \text{and} \quad \gamma \neq 0, \\ 0, & \gamma = 0. \end{cases} \quad (1.77)$$

When the field point is in Layer i , the source point is in Layer p , and $i < p$,

$$F_2(z, z') = \begin{cases} -\frac{\tilde{T}_{pi}^{TM} \tilde{M}_p^{TM}}{\varepsilon_p \gamma} [e^{-\gamma(2h_{p-1}-z')} + \tilde{R}_{p-}^{TM} e^{-\gamma(h_{p-1}-2h_p+z')}] \\ [e^{-\gamma(-h_i+z)} + \tilde{R}_{i+}^{TM} e^{-\gamma(2h_{i-1}-h_i-z)}], & \gamma \neq 0, \\ -\frac{1}{\varepsilon_p} z z' \tilde{T}_{pi}^{TM} \tilde{M}_p^{TM} [1 - \tilde{R}_{p+}^{TM}] [1 - \tilde{R}_{i+}^{TM}], & \gamma = 0. \end{cases} \quad (1.78)$$

When the field point is in Layer j , the source point is in Layer p , and $j > p$, the assistant integral functions are

$$F_2(z, z') = \begin{cases} -\frac{\tilde{T}_{pj}^{TM} \tilde{M}_p^{TM}}{\epsilon_p \gamma} [e^{-\gamma(2h_{j-1}-z)} + \tilde{R}_{j-}^{TM} e^{-\gamma(h_{j-1}-2h_j+z)}] \\ [e^{-\gamma(-h_p+z')} + \tilde{R}_{p+}^{TM} e^{-\gamma(2h_{p-1}-h_p-z')}], & \gamma \neq 0, \\ -\frac{1}{\epsilon_p} z z' \tilde{T}_{pj}^{TM} \tilde{M}_p^{TM} [1 - \tilde{R}_{p+}^{TM}] [1 - \tilde{R}_{j-}^{TM}], & \gamma = 0. \end{cases} \quad (1.79)$$

$$2\gamma \int_{z_{p1}}^{z_{p2}} \tilde{G}_x^\phi(\bar{r}, \bar{r}') dz = \begin{cases} F_3(z_{p2}, z') - F_3(z_{p1}, z') + SF_3 & i = p \\ F_3(z_{p2}, z') - F_3(z_{p1}, z') & i \neq p \end{cases} \quad (1.80)$$

When the source and the field points are in the same dielectric Layer i ,

$$F_3(z, z') = \begin{cases} \frac{\tilde{M}_i^{TM}}{\epsilon_i \gamma} [-\tilde{R}_{i+}^{TM} e^{-\gamma(2h_{i-1}-z-z')} + \tilde{R}_{i-}^{TM} e^{-\gamma(-2h_i+z+z')}] \\ + \tilde{R}_{i+}^{TM} \tilde{R}_{i-}^{TM} (e^{-\gamma(2d_i-z+z')} + e^{-\gamma(2d_i+z-z')})], & \gamma \neq 0, \\ \frac{1}{\epsilon_i} z [1 - \tilde{M}_i^{TM} (\tilde{R}_{i+}^{TM} + \tilde{R}_{i-}^{TM} - 2\tilde{R}_{i+}^{TM} \tilde{R}_{i-}^{TM})], & \gamma = 0. \end{cases} \quad (1.81)$$

$$SF_3 = \begin{cases} \frac{1}{\epsilon_i \gamma} (e^{-\gamma(z_{p1}-z')} - e^{-\gamma(z_{p2}-z')}), & z_{p1} \geq z' \quad \text{and} \quad \gamma \neq 0, \\ \frac{1}{\epsilon_i \gamma} (e^{-\gamma(z'-z_{p2})} - e^{-\gamma(z'-z_{p1})}), & z_{p2} \leq z' \quad \text{and} \quad \gamma \neq 0, \\ \frac{1}{\epsilon_i \gamma} (2 - e^{-\gamma(z'-z_{p1})} - e^{-\gamma(z_{p2}-z')}), & z_{p1} < z' < z_{p2} \quad \text{and} \quad \gamma \neq 0, \\ 0, & \gamma = 0. \end{cases} \quad (1.82)$$

When the field point is in Layer i , the source point is in Layer p , and $i < p$, the assistant integral functions are

$$F_3(z, z') = \begin{cases} -\frac{\tilde{T}_{pi}^{TM} \tilde{M}_p^{TM}}{\varepsilon_p \gamma} [e^{-\gamma(2h_{p-1}-z')} - \tilde{R}_{p-}^{TM} e^{-\gamma(h_{p-1}-2h_p+z')}] \\ [e^{-\gamma(-h_i+z)} - \tilde{R}_{i+}^{TM} e^{-\gamma(2h_{i-1}-h_i-z)}], & \gamma \neq 0, \\ \frac{1}{\varepsilon_p} z \tilde{T}_{pi}^{TM} \tilde{M}_p^{TM} [1 - \tilde{R}_{p-}^{TM}] [1 - \tilde{R}_{i+}^{TM}], & \gamma = 0. \end{cases} \quad (1.83)$$

When the field point is in Layer j , the source point is in Layer p , and $j > p$,

$$F_3(z, z') = \begin{cases} \frac{\tilde{T}_{pj}^{TM} \tilde{M}_p^{TM}}{\varepsilon_p \gamma} [e^{-\gamma(2h_{j-1}-z)} + \tilde{R}_{j-}^{TM} e^{-\gamma(h_{j-1}-2h_j+z)}] \\ [e^{-\gamma(-h_p+z')} - \tilde{R}_{p+}^{TM} e^{-\gamma(2h_{p-1}-h_p-z')}], & \gamma \neq 0, \\ \frac{1}{\varepsilon_p} z \tilde{T}_{pj}^{TM} \tilde{M}_p^{TM} [1 - \tilde{R}_{j-}^{TM}] [1 - \tilde{R}_{p+}^{TM}], & \gamma = 0. \end{cases} \quad (1.84)$$

$$2\gamma \int_{z_{p1}}^{z_{p2}} \int_{z_{q1}}^{z_{q2}} \tilde{G}_{zz}^A(\vec{r}, \vec{r}') (z - z_p)(z' - z_q) dz' dz = \begin{cases} F_4(z_{p2}, z_{q2}) - F_4(z_{p2}, z_{q1}) \\ -F_4(z_{p1}, z_{q2}) + F_4(z_{p1}, z_{q1}) + SF_4, & i = p, \\ F_4(z_{p2}, z_{q2}) - F_4(z_{p2}, z_{q1}) \\ -F_4(z_{p1}, z_{q2}) + F_4(z_{p1}, z_{q1}), & i \neq p. \end{cases} \quad (1.85)$$

When the source and the field points are in the same dielectric Layer i , the assistant integral functions are

$$\begin{aligned}
F_4(z, z') = & \left\{ \begin{aligned} & \frac{\mu_i \tilde{M}_i^{TM}}{\gamma^2} \left[\tilde{R}_{i+}^{TM} \left(z' - z_q - \frac{1}{\gamma} \right) \left(z - z_p - \frac{1}{\gamma} \right) e^{-\gamma(2h_1 - z - z')} \right. \\ & + \tilde{R}_{i-}^{TM} \left(z' - z_q + \frac{1}{\gamma} \right) \left(z - z_p + \frac{1}{\gamma} \right) e^{-\gamma(-2h_1 + z + z')} \\ & + \tilde{R}_{i+}^{TM} \tilde{R}_{i-}^{TM} \left((-z' + z_q - \frac{1}{\gamma}) \left(z - z_p - \frac{1}{\gamma} \right) e^{-\gamma(2d_1 - z + z')} \right. \\ & \left. \left. - (z' - z_q - \frac{1}{\gamma}) \left(z - z_p + \frac{1}{\gamma} \right) e^{-\gamma(2d_1 + z - z')} \right] \right\}, \quad \gamma \neq 0, \\ & \mu_i z z' [1 - \tilde{M}_i^{TM} (\tilde{R}_{i+}^{TM} + \tilde{R}_{i-}^{TM} - 2\tilde{R}_{i+}^{TM} \tilde{R}_{i-}^{TM})], \quad \gamma = 0. \end{aligned} \right. \quad (1.86)
\end{aligned}$$

$$\begin{aligned}
SF_4 = & \left\{ \begin{aligned} & SF_5(z_{p2}, z_{q2}) + SF_5(z_{p1}, z_{q1}) \\ & - SF_5(z_{p2}, z_{q1}) - SF_5(z_{p1}, z_{q2}), \quad z_{q2} > z_{p2} \quad \text{and} \quad \gamma \neq 0, \\ & SF_6(z_{p2}, z_{q2}) + SF_6(z_{p1}, z_{q1}) \\ & - SF_6(z_{p2}, z_{q1}) - SF_6(z_{p1}, z_{q2}), \quad z_{q2} < z_{p2} \quad \text{and} \quad \gamma \neq 0, \\ & 2\mu_i \left(\frac{z_{p2}^3 - z_{p1}^3}{3} - (z_p + z_q) \frac{z_{p2}^2 - z_{p1}^2}{2} \right. \\ & + z_p z_q (z_{p2} - z_{p1}) \frac{1}{\gamma} - ((z_{p2} - z_p) e^{-\gamma(z_{p2} - z_{q2})} \\ & - (z_{p1} - z_p) e^{-\gamma(z_{q2} - z_{p1})}) (z_{q2} - z_q) \frac{1}{\gamma^2} + (e^{-\gamma(z_{q2} - z_{p2})} \\ & - e^{-\gamma(z_{q2} - z_{p1})}) (z_{q2} - z_q) \frac{1}{\gamma^3} - ((z_{q2} - z_p) e^{-\gamma(z_{q2} - z_{p2})} \\ & - e^{-\gamma(z_{q2} - z_{p1})}) (z_{p1} - z_p) \frac{1}{\gamma^3} \\ & + (e^{-\gamma(z_{q2} - z_{p2})} - e^{-\gamma(z_{q1} - z_{p2})} \\ & - e^{-\gamma(z_{q2} - z_{p1})} + e^{-\gamma(z_{q1} - z_{p1})}) \frac{1}{\gamma^4} \\ & + ((z_{p2} - z_p) e^{\gamma(z_{q1} - z_{p2})} - (z_{p1} - z_p) e^{\gamma(z_{q1} - z_{p1})}) \frac{z_{q1} - z_q}{\gamma^2} \\ & + (e^{\gamma(z_{q1} - z_{p2})} + e^{\gamma(z_{q1} - z_{p1})}) \frac{z_{q1} - z_q}{\gamma^3} - ((z_{p2} - z_p) e^{\gamma(z_{q1} - z_{p2})} \\ & - (z_{p1} - z_p) e^{\gamma(z_{q1} - z_{p1})}) \frac{1}{\gamma^3}, \quad z_{q1} = z_{q2} \quad \text{and} \quad \gamma \neq 0, \\ & 0, \quad \gamma = 0. \end{aligned} \right. \quad (1.87)
\end{aligned}$$

$$SF_5(z, z') = -\mu_i((z'-z_q)(z-z_p) - \frac{z'-z_q}{\gamma} + \frac{z-z_p}{\gamma} - \frac{1}{\gamma^2}) \frac{e^{-\gamma(z'-z)}}{\gamma^2}. \quad (1.88)$$

$$SF_6(z, z') = -\mu_i((z'-z_q)(z-z_p) + \frac{z'-z_q}{\gamma} - \frac{z-z_p}{\gamma} - \frac{1}{\gamma^2}) \frac{e^{\gamma(z'-z)}}{\gamma^2}. \quad (1.89)$$

When the field point is in Layer i , the source point is in Layer p , and $i < p$,

$$F_4(z, z') = \begin{cases} \frac{\mu_p \tilde{T}_{pi}^{TM} \tilde{M}_p^{TM}}{\gamma^2} [(z' - z_q - \frac{1}{\gamma}) e^{-\gamma(2h_{p-1}-z')} \\ - \tilde{R}_{p-}^{TM} (z' - z_q + \frac{1}{\gamma}) e^{-\gamma(h_{p-1}-2h_p+z')}] [(-z + z_p - \frac{1}{\gamma}) e^{-\gamma(-h_i+z)} \\ + \tilde{R}_{i+}^{TM} (z - z_p - \frac{1}{\gamma}) e^{-\gamma(2h_{i-1}-h_i-z)}], & \gamma \neq 0, \\ \mu_p \frac{(z - z_p)^2 (z' - z_q)^2}{4} \tilde{T}_{pi}^{TM} \tilde{M}_p^{TM} [1 + \tilde{R}_{i+}^{TM}] [1 + \tilde{R}_{p-}^{TM}], & \gamma = 0. \end{cases} \quad (1.90)$$

When the field point is in Layer j , the source point is in Layer p , and $j > p$,

$$F_4(z, z') = \begin{cases} \frac{\mu_p \tilde{T}_{pj}^{TM} \tilde{M}_p^{TM}}{\gamma^2} [(z - z_q - \frac{1}{\gamma}) e^{-\gamma(2h_{j-1}-z)} \\ + \tilde{R}_{j-}^{TM} (-z + z_p - \frac{1}{\gamma}) e^{-\gamma(h_{j-1}-2h_j+z)}] [(-z' + z_q - \frac{1}{\gamma}) e^{-\gamma(-h_p+z')} \\ + \tilde{R}_{p+}^{TM} (z' - z_q - \frac{1}{\gamma}) e^{-\gamma(2h_{p-1}-h_p-z')}], & \gamma \neq 0, \\ \mu_p \frac{(z - z_p)^2 (z' - z_q)^2}{4} \tilde{T}_{pj}^{TM} \tilde{M}_p^{TM} [1 + \tilde{R}_{j-}^{TM}] [1 + \tilde{R}_{p+}^{TM}], & \gamma = 0. \end{cases} \quad (1.91)$$

$$2\gamma \int_{z_{p1}}^{z_{p2}} (z - z_p) \frac{\tilde{G}_{zx}^A(\vec{r}, \vec{r}')}{-jk_x} dz = F_5(z_{p2}, z') - F_5(z_{p1}, z'). \quad (1.92)$$

When the source and the field points are in the same dielectric Layer i , the assistant integral functions are

$$\begin{aligned}
F_5(z, z') = & \frac{\mu_i \tilde{M}_i^{TM}}{\gamma^2} \left[\tilde{R}_{i+}^{TM} \left(-z + z_p + \frac{1}{\gamma} \right) e^{-\gamma(2h_{i-1} - z - z')} - \tilde{R}_{i-}^{TM} \left(z - z_p + \frac{1}{\gamma} \right) e^{-\gamma(-2h_i + z + z')} \right. \\
& + \tilde{R}_{i+}^{TM} \tilde{R}_{i-}^{TM} \left(\left(z - z_p - \frac{1}{\gamma} \right) e^{-\gamma(2d_i - z + z')} + \left(z - z_p + \frac{1}{\gamma} \right) e^{-\gamma(2d_i + z - z')} \right) \Big] \\
& + \tilde{M}_i^{TE} \left[\tilde{R}_{i+}^{TE} \left(-z + z_p + \frac{1}{\gamma} \right) e^{-\gamma(2h_{i-1} - z - z')} - \tilde{R}_{i-}^{TE} \left(z - z_p + \frac{1}{\gamma} \right) e^{-\gamma(-2h_i + z + z')} \right. \\
& + \tilde{R}_{i+}^{TE} \tilde{R}_{i-}^{TE} \left(\left(-z + z_p - \frac{1}{\gamma} \right) e^{-\gamma(2d_i - z' + z)} - \left(z - z_p - \frac{1}{\gamma} \right) e^{-\gamma(2d_i - z + z')} \right) \Big].
\end{aligned} \tag{1.93}$$

When the field point is in Layer i, the source point is in Layer p, and $i < p$,

$$\begin{aligned}
F_5(z, z') = & \frac{\mu_p \tilde{T}_{pi}^{TM} \tilde{M}_p^{TM}}{\gamma^2} \left[\left(-z + z_p - \frac{1}{\gamma} \right) e^{-\gamma(-h_i + z)} + \tilde{R}_{i+}^{TM} \left(z - z_p - \frac{1}{\gamma} \right) e^{-\gamma(2h_{i-1} - h_i - z)} \right] \\
& \left[e^{-\gamma(2h_{p-1} - z')} + \tilde{R}_{p-}^{TM} e^{-\gamma(h_{p-1} - 2h_p + z')} \right] \\
& - \frac{\mu_i \tilde{T}_{pi}^{TE} \tilde{M}_p^{TE}}{\gamma^2} \left[\left(z - z_p + \frac{1}{\gamma} \right) e^{-\gamma(-h_i + z)} + \tilde{R}_{i+}^{TE} \left(z - z_p - \frac{1}{\gamma} \right) e^{-\gamma(-2h_{i-1} - h_i - z)} \right] \\
& \left[e^{-\gamma(h_{p-1} - z')} + \tilde{R}_{p-}^{TE} e^{-\gamma(h_{p-1} - 2h_p + z')} \right].
\end{aligned} \tag{1.94}$$

When the field point is in Layer j, the source point is in Layer p, and $j > p$,

$$\begin{aligned}
F_5(z, z') = & \frac{\mu_p \tilde{T}_{pj}^{TM} \tilde{M}_p^{TM}}{\gamma^2} \left[\left(z - z_p - \frac{1}{\gamma} \right) e^{-\gamma(-h_{j-1} - z)} \right. \\
& + \tilde{R}_{j-}^{TM} \left(z - z_p + \frac{1}{\gamma} \right) e^{-\gamma(h_{j-1} - 2h_j + z)} \Big] \\
& \left[e^{-\gamma(-h_p + z')} - \tilde{R}_{p+}^{TM} e^{-\gamma(2h_{p-1} - h_p - z')} \right] \\
& - \frac{\mu_i \tilde{T}_{pi}^{TE} \tilde{M}_p^{TE}}{\gamma^2} \left[\left(z - z_p + \frac{1}{\gamma} \right) e^{-\gamma(-h_i + z)} \right. \\
& + \tilde{R}_{i+}^{TE} \left(z - z_p - \frac{1}{\gamma} \right) e^{-\gamma(-2h_{i-1} - h_i - z)} \Big] \\
& \left[e^{-\gamma(h_{p-1} - z')} + \tilde{R}_{p-}^{TE} e^{-\gamma(h_{p-1} - 2h_p + z')} \right].
\end{aligned} \tag{1.95}$$

$$\begin{aligned}
& 2\gamma \int_{z_{q1}}^{z_{q2}} \tilde{G}_{xx}^A(\vec{r}, \vec{r}') dz' \\
& = \begin{cases} F_6(z, z_{q2}) - F_6(z, z_{q1}) + SF_6, & i = p, \\ F_6(z, z_{q2}) - F_6(z, z_{q1}), & i \neq p. \end{cases} \quad (1.96)
\end{aligned}$$

When the source and field points are in the same dielectric Layer p,

$$\begin{aligned}
F_6(z, z') & = \frac{\mu_p}{\gamma} \tilde{M}_p^{TE} \tilde{R}_{p+}^{TE} e^{-\gamma(2h_{p-1}-z-z')} \\
& \quad - \frac{\mu_p}{\gamma} \tilde{M}_p^{TE} \tilde{R}_{p-}^{TE} e^{-\gamma(-2h_p+z+z')} + \frac{\mu_p}{\gamma} \tilde{M}_p^{TE} \tilde{R}_{p+}^{TE} \tilde{R}_{p-}^{TE} e^{-\gamma(2d_p+z-z')} \\
& \quad - \frac{\mu_p}{\gamma} \tilde{M}_p^{TE} \tilde{R}_{p+}^{TE} \tilde{R}_{p-}^{TE} e^{-\gamma(2d_p-z+z')}, \quad \gamma \neq 0, \\
& = \mu_p [\tilde{M}_p^{TE} (\tilde{R}_{p+}^{TE} + \tilde{R}_{p-}^{TE} + 2\tilde{R}_{p+}^{TE} \tilde{R}_{p-}^{TE})] z', \quad \gamma = 0.
\end{aligned} \quad (1.97)$$

$$SF_6 = \begin{cases} \frac{\mu_p}{\gamma} (e^{-\gamma(z_{q1}-z)} - e^{-\gamma(z_{q2}-z)}), & z_{q1} \geq z \quad \text{and} \quad \gamma \neq 0, \\ \frac{\mu_p}{\gamma} (e^{-\gamma(z-z_{q2})} - e^{-\gamma(z-z_{q1})}), & z_{q2} \leq z \quad \text{and} \quad \gamma \neq 0, \\ \frac{\mu_p}{\gamma} (2 - e^{-\gamma(z-z_{q1})} - e^{-\gamma(z_{q2}-z)}) & z_{q1} < z < z_{q2} \quad \text{and} \quad \gamma \neq 0, \\ \mu_p (z_{q2} - z_{q1}) & \gamma = 0. \end{cases} \quad (1.98)$$

When the field point is in Layer i, the source point is in Layer p, and $i < p$,

$$F_6(z, z') = \begin{cases} \mu_i \tilde{T}_{pi}^{TE} \tilde{M}_p^{TE} (1 + \tilde{R}_{i+}^{TE})(1 + \tilde{R}_{p-}^{TE}) z', & \gamma = 0, \\ \mu_i \tilde{T}_{pi}^{TE} \tilde{M}_p^{TE} [e^{-\gamma(z-h_i)} + \tilde{R}_{i+}^{TE} e^{-\gamma(2h_{i-1}-h_i-z)}] \\ \quad \left[\frac{1}{\gamma} e^{-\gamma(h_{p-1}-z')} - \frac{\tilde{R}_{p-}^{TE}}{\gamma} e^{-\gamma(z'+h_{p-1}-2h_p)} \right], & \gamma \neq 0. \end{cases} \quad (1.99)$$

When the field point is in Layer j, the source point is in Layer p, and $j > p$,

$$F_6(z, z') = \begin{cases} \mu_j \tilde{T}_{pj}^{TE} \tilde{M}_p^{TE} (1 + \tilde{R}_{j-}^{TE})(1 + \tilde{R}_{p+}^{TE}) z', & \gamma = 0, \\ \mu_j \tilde{T}_{pj}^{TE} \tilde{M}_p^{TE} [e^{-\gamma(-z+h_{j-1})} + \tilde{R}_{j-}^{TE} e^{-\gamma(h_{j-1}-2h_j+z)}] \\ \quad \left[-\frac{1}{\gamma} e^{-\gamma(-h_p+z')} + \frac{\tilde{R}_{p+}^{TE}}{\gamma} e^{-\gamma(2h_{p-1}-z'-h_p)} \right], & \gamma \neq 0. \end{cases} \quad (1.100)$$

$$2\gamma \int_{z_{p1}}^{z_{p2}} \tilde{G}_{xx}^A(\bar{r}, \bar{r}') dz = \begin{cases} F_7(z_{p2}, z') - F_7(z_{p1}, z') + SF_7, & i = p, \\ F_7(z_{p2}, z') - F_7(z_{p1}, z'), & i \neq p. \end{cases} \quad (1.101)$$

$$F_7(z, z') = \begin{cases} \frac{\mu_p}{\gamma} \tilde{M}_p^{TE} \tilde{R}_{p+}^{TE} e^{-\gamma(2h_{p-1}-z-z')} \\ - \frac{\mu_p}{\gamma} \tilde{M}_p^{TE} \tilde{R}_{p-}^{TE} e^{-\gamma(-2h_p+z+z')} \\ - \frac{\mu_p}{\gamma} \tilde{M}_p^{TE} \tilde{R}_{p+}^{TE} \tilde{R}_{p-}^{TE} e^{-\gamma(2d_p+z-z')} \\ + \frac{\mu_p}{\gamma} \tilde{M}_p^{TE} \tilde{R}_{p+}^{TE} \tilde{R}_{p-}^{TE} e^{-\gamma(2d_p-z+z')}, & \gamma \neq 0, \\ \mu_p [\tilde{M}_p^{TE} (\tilde{R}_{p+}^{TE} + \tilde{R}_{p-}^{TE} + 2\tilde{R}_{p+}^{TE} \tilde{R}_{p-}^{TE})] z, & \gamma = 0. \end{cases} \quad (1.102)$$

$$SF_7 = \begin{cases} \frac{\mu_p}{\gamma} (e^{-\gamma(z_{p1}-z')} - e^{-\gamma(z_{p2}-z')}), & z_{p1} \geq z' \quad \text{and} \quad \gamma \neq 0, \\ \frac{\mu_p}{\gamma} (e^{-\gamma(z'-z_{p2})} - e^{-\gamma(z'-z_{p1})}), & z_{p2} \leq z' \quad \text{and} \quad \gamma \neq 0, \\ \frac{\mu_p}{\gamma} (2 - e^{-\gamma(z'-z_{p1})} - e^{-\gamma(z_{p2}-z')}) & z_{p1} < z < z_{p2} \quad \text{and} \quad \gamma \neq 0, \\ \mu_p (z_{p2} - z_{p1}), & \gamma = 0. \end{cases} \quad (1.103)$$

When the field point is in Layer i , the source point is in Layer p , and $i < p$,

$$F_7(z, z') = \begin{cases} \mu_i \tilde{T}_{pi}^{TE} \tilde{M}_p^{TE} (1 + \tilde{R}_{i+}^{TE})(1 + \tilde{R}_{p-}^{TE}) z, & \gamma = 0, \\ \mu_i \tilde{T}_{pi}^{TE} \tilde{M}_p^{TE} \left[-\frac{1}{\gamma} e^{-\gamma(z-h_i)} + \frac{\tilde{R}_{i+}^{TE}}{\gamma} e^{-\gamma(2h_{i-1}-h_i-z)} \right] \\ \quad [e^{-\gamma(h_{p-1}-z')} + \tilde{R}_{p-}^{TE} e^{-\gamma(z'+h_{p-1}-2h_p)}], & \gamma \neq 0. \end{cases} \quad (1.104)$$

When the field point is in Layer j , the source point is in Layer p , and $j > p$, the assistant integral functions are

$$F_7(z, z') = \begin{cases} \mu_j \tilde{T}_{pj}^{TE} \tilde{M}_p^{TE} (1 + \tilde{R}_{j-}^{TE})(1 + \tilde{R}_{p+}^{TE}) z, & \gamma = 0, \\ \mu_j \tilde{T}_{pj}^{TE} \tilde{M}_p^{TE} \left[\frac{1}{\gamma} e^{-\gamma(-z+h_{j-1})} - \frac{\tilde{R}_{j-}^{TE}}{\gamma} e^{-\gamma(h_{j-1}-2h_i+z)} \right] \\ \quad [e^{-\gamma(-h_p+z')} + \tilde{R}_{p+}^{TE} e^{-\gamma(2h_{p-1}-z'-h_p)}], & \gamma \neq 0. \end{cases} \quad (1.105)$$

$$2\gamma \int_{z_{p1}}^{z_{p2}} \int_{z_{q1}}^{z_{q2}} \tilde{G}_{xx}^A(\bar{r}, \bar{r}') dz' dz = \begin{cases} F_8(z_{p2}, z_{q2}) - F_8(z_{p2}, z_{q1}) - F_8(z_{p1}, z_{q2}) + F_8(z_{p1}, z_{q1}) + SF_8, & i = p, \\ F_8(z_{p2}, z_{q2}) - F_8(z_{p2}, z_{q1}) - F_8(z_{p1}, z_{q2}) + F_8(z_{p1}, z_{q1}), & i \neq p. \end{cases} \quad (1.106)$$

When the source and field points are in the same dielectric Layer p,

$$F_8(z, z') = \begin{cases} \frac{\mu_p}{\gamma^2} \tilde{M}_p^{TE} \tilde{R}_{p+}^{TE} e^{-\gamma(2h_{p-1}-z-z')} \\ \quad + \frac{\mu_p}{\gamma^2} \tilde{M}_p^{TE} \tilde{R}_{p-}^{TE} e^{-\gamma(-2h_p+z+z')} \\ \quad - \frac{\mu_p}{\gamma^2} \tilde{M}_p^{TE} \tilde{R}_{p+}^{TE} \tilde{R}_{p-}^{TE} e^{-\gamma(2d_p+z-z')} \\ \quad - \frac{\mu_p}{\gamma^2} \tilde{M}_p^{TE} \tilde{R}_{p+}^{TE} \tilde{R}_{p-}^{TE} e^{-\gamma(2d_p-z+z')}, & \gamma \neq 0, \\ \mu_p [\tilde{M}_p^{TE} (\tilde{R}_{p+}^{TE} + \tilde{R}_{p-}^{TE} + 2\tilde{R}_{p+}^{TE} \tilde{R}_{p-}^{TE})] z' z, & \gamma = 0. \end{cases} \quad (1.107)$$

$$SF_8 = \begin{cases} \frac{\mu_p}{\gamma^2} (e^{-\gamma(z_{q1}-z)} - e^{-\gamma(z_{q2}-z)}) \Big|_{z_{p1}}^{z_{p2}}, & z_{q2} > z_{p2} \quad \text{and} \quad \gamma \neq 0, \\ -\frac{\mu_p}{\gamma^2} (e^{-\gamma(z-z_{q2})} - e^{-\gamma(z-z_{q1})}) \Big|_{z_{p1}}^{z_{p2}}, & z_{q2} < z_{p2} \quad \text{and} \quad \gamma \neq 0, \\ \frac{\mu_p}{\gamma^2} (e^{-\gamma(z-z_{q1})} - e^{-\gamma(z_{q2}-z)}) \Big|_{z_{p1}}^{z_{p2}}, & z_{q2} = z_{p2} \quad \text{and} \quad \gamma \neq 0, \\ \mu_p (z_{q2} - z_{q1})(z_{p2} - z_{p1}), & \gamma = 0. \end{cases} \quad (1.108)$$

When the field point is in Layer i, the source point is in Layer p, and $i < p$, the assistant integral functions are

$$F_8(z, z') = \begin{cases} \mu_i \tilde{T}_{pi}^{TE} \tilde{M}_p^{TE} (1 + \tilde{R}_{i+}^{TE})(1 + \tilde{R}_{p-}^{TE})]zz', & \gamma = 0, \\ \mu_i \tilde{T}_{pi}^{TE} \tilde{M}_p^{TE} \left[-\frac{1}{\gamma} e^{-\gamma(z-h_i)} + \frac{\tilde{R}_{i+}^{TE}}{\gamma} e^{-\gamma(2h_{i-1}-h_i-z)} \right] & \\ \left[\frac{1}{\gamma} e^{-\gamma(h_{p-1}-z')} - \frac{\tilde{R}_{p-}^{TE}}{\gamma} e^{-\gamma(z'+h_{p-1}-2h_p)} \right], & \gamma \neq 0. \end{cases} \quad (1.109)$$

When the field point is in Layer j, the source point is in Layer p, and $j > p$, the assistant integral functions are

$$F_8(z, z') = \begin{cases} \mu_j \tilde{T}_{pj}^{TE} \tilde{M}_p^{TE} (1 + \tilde{R}_{j-}^{TE})(1 + \tilde{R}_{p+}^{TE})]zz', & \gamma = 0, \\ \mu_j \tilde{T}_{pj}^{TE} \tilde{M}_p^{TE} \left[\frac{1}{\gamma} e^{-\gamma(-z+h_{j-1})} - \frac{\tilde{R}_{j-}^{TE}}{\gamma} e^{-\gamma(h_{j-1}-2h_i+z)} \right] & \\ \left[-\frac{1}{\gamma} e^{-\gamma(-h_p+z')} + \frac{\tilde{R}_{p+}^{TE}}{\gamma} e^{-\gamma(2h_{p-1}-z'-h_p)} \right], & \gamma \neq 0. \end{cases} \quad (1.110)$$

$$\begin{aligned} & \int_{z_{p1}}^{z_{p2}} \int_{z_{q1}}^{z_{q2}} (Z - Z_p) [G_{zx}^A(\vec{r}, \vec{r}') \bar{\rho}_q(\vec{r}') \cdot \hat{x} + G_{zy}^A(\vec{r}, \vec{r}') \bar{\rho}_q(\vec{r}') \cdot \hat{y}] dz' dz \\ & = \nabla_{xy} \cdot \mathcal{F}^{-1} \left[\int_{z_{p1}}^{z_{p2}} \int_{z_{q1}}^{z_{q2}} (Z - Z_p) \frac{\tilde{G}_{zx}^A(\vec{r}, \vec{r}')}{-jk_x} dz' dz \right] \cdot \bar{\rho}_q(\vec{r}'). \end{aligned} \quad (1.111)$$

$$\begin{aligned} & 2\gamma \int_{z_{p1}}^{z_{p2}} \int_{z_{q1}}^{z_{q2}} (Z - Z_p) \frac{\tilde{G}_{zx}^A(\vec{r}, \vec{r}')}{-jk_x} dz' dz \\ & = F_9(z_{p2}, z_{q2}) - F_9(z_{p2}, z_{q1}) - F_9(z_{p1}, z_{q2}) + F_9(z_{p1}, z_{q1}). \end{aligned} \quad (1.112)$$

When the source and field points are in the same dielectric Layer i, the assistant integral functions are

$$\begin{aligned}
F_9(z, z') = & \frac{\mu_i}{\gamma^2} \left\{ \tilde{M}_i^{TM} \left[\frac{\tilde{R}_{i+}^{TM}}{\gamma} \left(z_p - z + \frac{1}{\gamma} \right) e^{-\gamma(2h_{i-1}-z-z')} \right. \right. \\
& + \frac{\tilde{R}_{i-}^{TM}}{\gamma} \left(-z_p + z + \frac{1}{\gamma} \right) e^{-\gamma(-2h_i+z+z')} \\
& + \frac{\tilde{R}_{i+}^{TM} \tilde{R}_{i-}^{TM}}{-\gamma} \left(-z_p + z - \frac{1}{\gamma} \right) e^{-\gamma(2d_i-z+z')} \\
& \left. + \frac{\tilde{R}_{i+}^{TM} \tilde{R}_{i-}^{TM}}{\gamma} \left(-z_p + z + \frac{1}{\gamma} \right) e^{-\gamma(2d_i+z-z')} \right] \\
& + \tilde{M}_i^{TE} \left[\frac{\tilde{R}_{i+}^{TE}}{\gamma} \left(z_p - z + \frac{1}{\gamma} \right) e^{-\gamma(2h_{i-1}-z-z')} \right. \\
& + \frac{\tilde{R}_{i-}^{TE}}{\gamma} \left(-z_p + z + \frac{1}{\gamma} \right) e^{-\gamma(-2h_i+z+z')} \\
& + \frac{\tilde{R}_{i+}^{TE} \tilde{R}_{i-}^{TE}}{\gamma} \left(z_p - z - \frac{1}{\gamma} \right) e^{-\gamma(2d_i+z-z')} \\
& \left. + \frac{\tilde{R}_{i+}^{TE} \tilde{R}_{i-}^{TE}}{\gamma} \left(-z_p + z - \frac{1}{\gamma} \right) e^{-\gamma(2d_i-z+z')} \right]. \tag{1.113}
\end{aligned}$$

When the field point is in Layer i, the source point is in Layer p, and $i < p$,

$$\begin{aligned}
F_9(z, z') = & -\frac{\mu_p}{\gamma^2} \tilde{T}_{pi}^{TM} \tilde{M}_p^{TM} \left[\left(z_p - z - \frac{1}{\gamma} \right) e^{-\gamma(z-h_i)} \right. \\
& \left. + \tilde{R}_{i+}^{TM} \left(-z_p + z - \frac{1}{\gamma} \right) e^{-\gamma(2h_{i-1}-h_i-z)} \right]. \\
& \left[\frac{1}{\gamma} e^{-\gamma(h_{p-1}-z')} + \frac{\tilde{R}_{p-}^{TM}}{\gamma} e^{-\gamma(h_{p-1}-2h_p+z')} \right] \\
& -\frac{\mu_i}{\gamma^2} \tilde{T}_{pi}^{TE} \tilde{M}_p^{TE} \left[\left(-z_p + z + \frac{1}{\gamma} \right) e^{-\gamma(z-h_i)} \right. \\
& \left. + \tilde{R}_{i+}^{TE} \left(-z_p + z - \frac{1}{\gamma} \right) e^{-\gamma(2h_{i-1}-h_i-z)} \right]. \\
& \left[\frac{1}{\gamma} e^{-\gamma(h_{p-1}-z')} - \frac{\tilde{R}_{p-}^{TE}}{\gamma} e^{-\gamma(h_{p-1}-2h_p+z')} \right]. \tag{1.114}
\end{aligned}$$

When the field point is in Layer j, the source point is in Layer p, and $j > p$, the assistant integral functions are

$$\begin{aligned}
F_9(z, z') = & -\frac{\mu_p}{\gamma^2} \tilde{T}_{pj}^{TM} \tilde{M}_p^{TM} \left[(-z_p + z - \frac{1}{\gamma}) e^{-\gamma(-z+h_{j-1})} \right. \\
& \left. - \tilde{R}_{j-}^{TM} (-z_p + z + \frac{1}{\gamma}) e^{-\gamma(h_{j-1}+2h_j+z)} \right] \\
& \left[-\frac{1}{\gamma} e^{-\gamma(-h_p+z')} + \frac{\tilde{R}_{p+}^{TM}}{\gamma} e^{-\gamma(2h_{p-1}-h_p-z')} \right] \\
& -\frac{\mu_i}{\gamma^2} \tilde{T}_{pj}^{TE} \tilde{M}_p^{TE} \left[(-z_p + z - \frac{1}{\gamma}) e^{-\gamma(-z+h_{j-1})} \right. \\
& \left. + \tilde{R}_{j-}^{TE} (-z_p + z + \frac{1}{\gamma}) e^{-\gamma(-2h_j+h_{j-1}+z)} \right] \\
& \left[\frac{1}{\gamma} e^{-\gamma(-h_p+z')} + \frac{\tilde{R}_{p+}^{TE}}{\gamma} e^{-\gamma(2h_{p-1}-h_p-z')} \right].
\end{aligned} \tag{1.115}$$

1.3. NUMERICAL RESULTS

In this section, numerical results are presented to illustrate the role of transverse current in via modeling and the results of CEMPIE modeling with the improved basis functions.

Figure 1.7 shows a via transition on a 6-layer printed circuit board. The stackup of the board is shown in Figure 1.7(a). The top, third, fourth, and bottom layer are signal layers, while the second and fifth layer are power/ground layers. There are two PCB cores with thickness of 6.04 mils and the thickness of pre-preg between top/bottom layer and cores are 4.1 mils. The pre-preg layer between two cores is 9.2mil thick. The dielectric constant of all layers is approximately 4.0 with 0.02 loss tangent. The size of the board is 30 mm by 20 mm. A via is located at the coordinates (10,10) and connected to two 50Ω-microstrip traces on the top and the bottom signal layers. The radius of the via is 10 mils and the radius of the via pad is 16 mils. The diameter of the anti-pad is 37 mils. Two microstrip stubs located on the top and bottom layers have 39.4mil length.

To simulate the S-parameters of this via transition, two lumped ports were set at the edge the microstrip stubs. The structure may be considered as three two-layer structures, while the top structure and bottom structure are exactly same. These three two-layer structures are designated as “Block A”, “Block D” and “Block A” respectively. If the magnetic coupling between three blocks around the via is neglected, the entire

geometry may be modeled separately as three two-layer boards. The original CEMPIE code, which enforced the current flow vertically along vertical surfaces, was used to model each block individually. S-parameters of each block were then transformed to ABCD matrices. Subsequently, the three ABCD matrices were multiplied to acquire the ABCD matrix when three blocks cascaded together. Finally the ABCD matrixes of the cascaded blocks were transformed back to S-parameters. Figure 1.8 compares cascaded modeling results with direct CEMPIE modeling of the entire geometry. The blue curve is the magnitude of S_{11} modeled by the original CEMPIE code, while the red curve shows the results when three blocks were modeled separately and cascaded together. It is clear that the peaks of magnitude of S_{11} matched very well, which is due to resonance of the board, but the null associated with via inductance and board capacitance cannot match. Further simulation showed that if a 0.16 nH inductor was put between the every two blocks as shown in Figure 1.9, the cascaded result, green curve, would match the simulation results of entire geometry. At the same time, the magnitude of S_{21} does not show the obvious difference as shown in Figure 1.10.

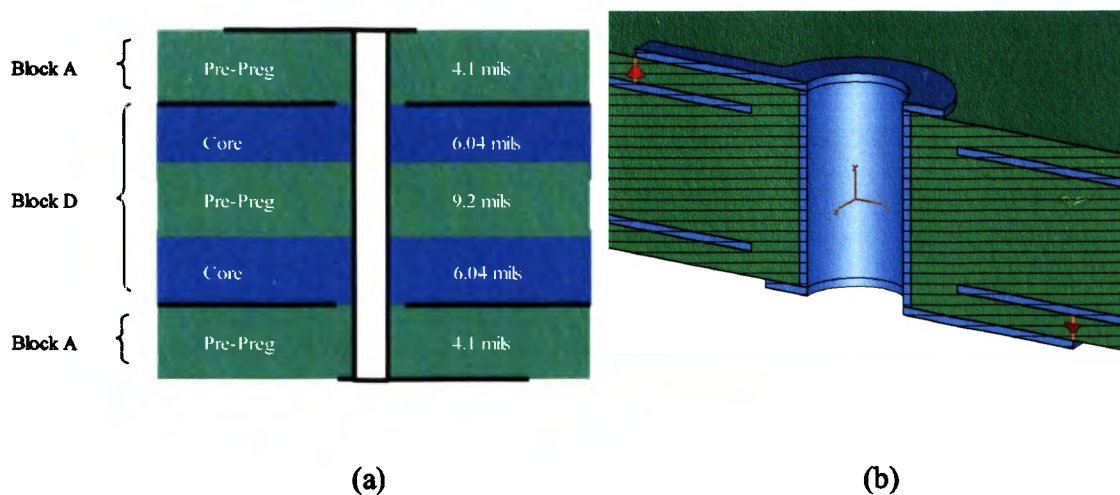


Figure 1.7. A via transition on a 6-layer board, (a) side view, (b) perspective view.

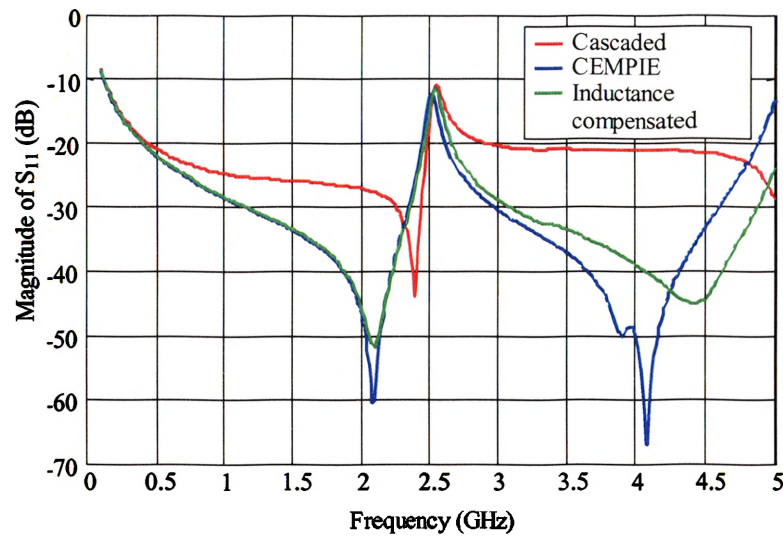


Figure 1.8. Modeling results— S_{11} using CEMPIE without horizontal current components on the vertical surface.

The reason for this discrepancy in the magnitude of S_{11} is that the original CEMPIE's basis functions cannot describe the transverse current along the via. So it enforces the current flow vertically along the via body. However, the real current distribution has transverse current components to keep the loop inductance as small as possible as shown in Figure 1.11. Therefore, the inductance associated with via was not modeled accurately using the original CEMPIE. In fact, it produced a larger value of via inductance. That is the reason why cascaded results with compensation inductors can match the CEMPIE simulation results.

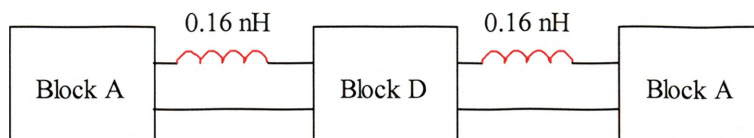


Figure 1.9. Cascaded blocks with compensation inductors.

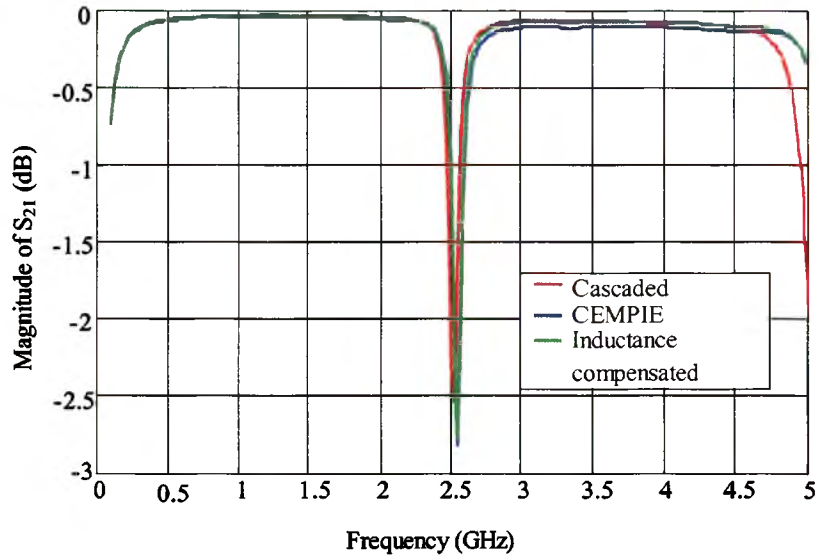


Figure 1.10. Modeling results— S_{21} using CEMPIE without horizontal current components on the vertical surface.

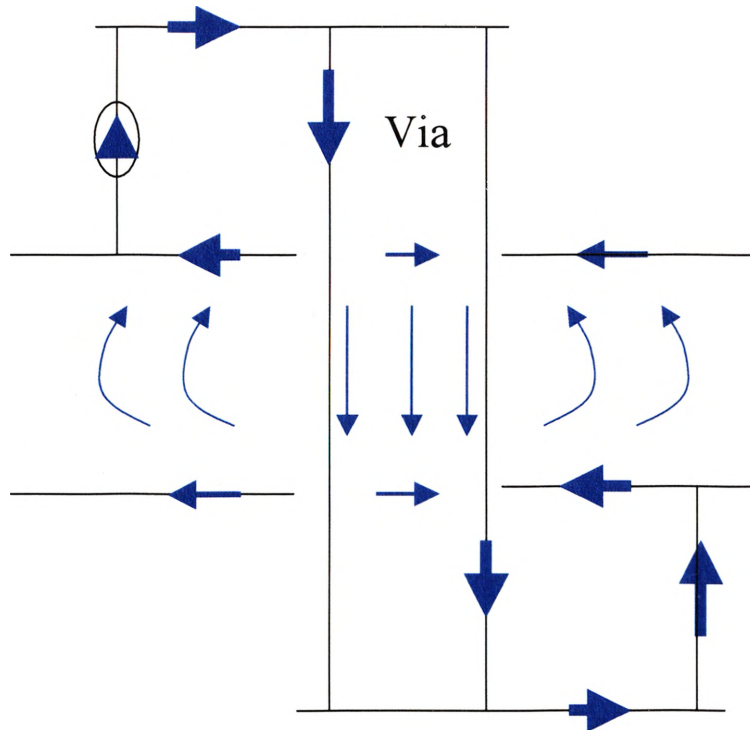


Figure 1.11. Current distribution of the test case in Figure 1.7.

The simulation results using CEMPIE with improved basis functions are shown in Figure 1.12 and Figure 1.13. From the figure, one observes that the simulation results for the entire geometry and the cascaded results matched very well with 3dB difference for S_{11} and less than 0.05 dB for S_{21} . Figure 1.12 and Figure 1.13 also compare the CEMPIE simulation results with another commercial full-wave tool using the finite integral technique. There is a very good agreement between these two full-wave simulation results.

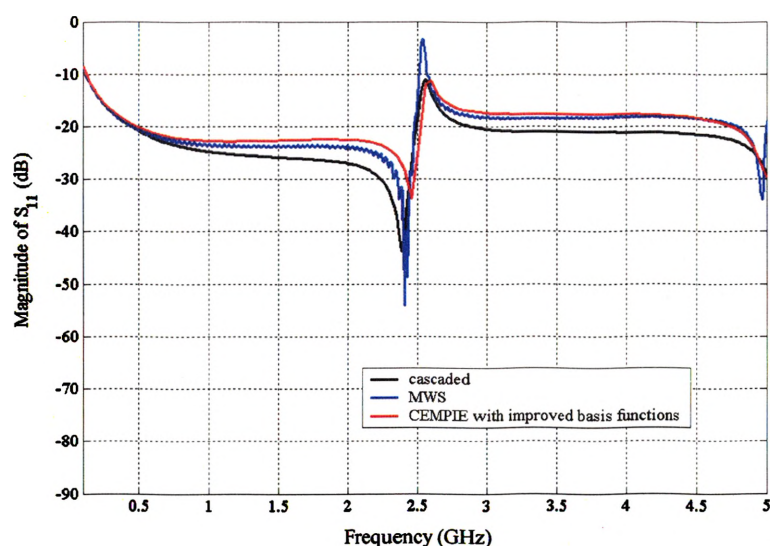


Figure 1.12. Modeling results— S_{11} using CEMPIE with the improved basis functions.

1.4. CONCLUSION

CEMPIE is a full-wave simulation algorithm for layered media. A set of improved basis functions has been proposed and by using the improved basis functions CEMPIE may model the transverse components of currents on vertical conductive surfaces. The role of the transverse currents on vertical conductive surfaces has been studied. It was found that for the models of via transitions on PCBs, the parasitic inductance associated with vias is strongly affected by the accuracy of modeling the

current path. The improved basis functions provide the ability to model the current path more accurately. Agreement between different simulation results for a via transition using CEMPIE and a full-wave finite integral integration method has been exhibited.

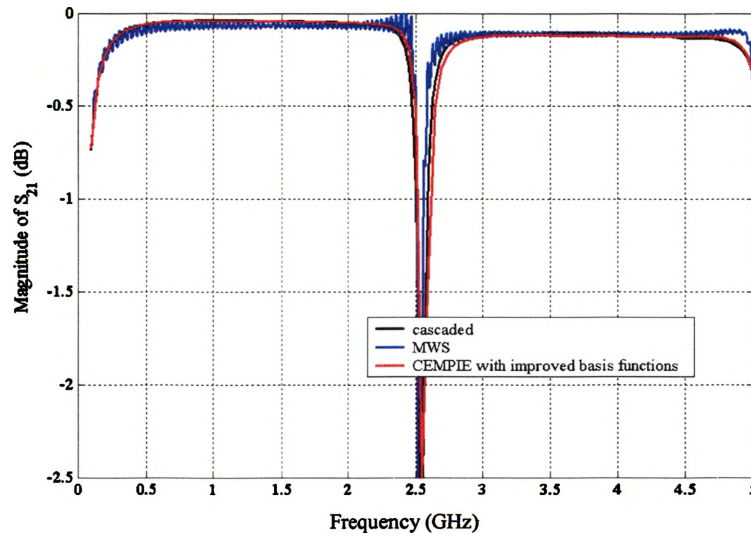


Figure 1.13. Modeling results— S_{21} using CEMPIE with the improved basis functions.

2. VIA MODELS FOR SINGLE-ENDED SIGNALING

In high-speed digital design, signal via transitions on PCBs are becoming an important signal integrity issue. When the data rate exceeds a giga-bit per second, via transitions may distort and degrade the signal. Efficient and accurate models for via transitions are necessary to analyze high bit-rate digital circuit system designs. These models should be compatible with fast simulation tools. The goal of this study is an engineering level SPICE-compatible circuit model for via transitions. This section discusses how to model the signal via transition for single-ended signaling.

2.1. INTRODUCTION

Prior work focused on the impact of a via on signal quality [21] - [25]. The equivalent circuit of a via which connected two semi-infinitely long transmission lines through a circular hole in a ground plane were modeled as a π -shape equivalent circuit and the elements of the circuit were calculated by the method of moments from a set of integral equations [26]. In [27], an integral equation-based quasi-static method is used for calculating the capacitance of multilayer board vias. More recent efforts have studied the physics-based circuit model of complex via hole structures [28]. The via hole is modeled as a cascaded combination of capacitance and inductance matrices. The capacitance values are computed using an electrostatic solver while inductance values are computed from a 2-D quasi-TEM solver. In this section, a procedure for building a SPICE model library for via transitions is proposed. Using this library, SPICE models for various vias on a specified PCB stack-up are constructed by cascading building blocks, consisting of SPICE models for elements of the via structure. A full-wave numerical approach, CEMPIE (Circuit Extraction based on Mixed Potential Integral Equation) [1], was used to extract the lumped element parameters of those building blocks.

An example of a four-layer board with a via transition was measured and simulated using CEMPIE to check the validity as a full-wave simulation tool for via transition in multi-layer PCBs. For multi-layer PCBs, there are several internal solid planes such as power bus structures. These internal solid planes can be seen as natural separations for the building blocks. The objective is to model every part separated by

internal solid planes independently. This method is called the peeling and partitioning process in this section. An inductance and capacitance circuit model in a π -shape topology was used to model the building block for an example of via transitions. In digital design, time-domain simulations are more common than frequency domain simulations. The effect of the via transition in the time domain simulation was investigated also. A library matrix was constructed for single-ended signaling on a 10-layer printed circuit board. Furthermore, the library matrix showed how to use the model blocks to build a complete SPICE model for an entire via transition.

At high frequencies, the geometry of a parallel plane power bus and the position of the via affect the distributive behavior of a via. In this situation, a simple capacitive model is not sufficient to model the power bus. An equivalent circuit with transformers from cavity models may model the distributive behavior of a rectangular board. Furthermore, the input impedance of an irregular shaped board can be calculated with a segmentation or desegmentation method. Then the input impedance of a powerbus can be put in the SPICE model for a via transition instead of a simple capacitive model.

2.2. MODELING A VIA WITH CEMPIE AND SPICE

To simplify the modeling of via transitions, a multi-layer board was viewed as many two-layer board elements laminated together. Then each two-layer board element was modeled independently, forming a building block. The magnetic coupling between the blocks around the via was neglected in this procedure. The model for the entire via transition was constructed by cascading building blocks. To demonstrate the procedure mentioned above, an example of a via transition was investigated. The geometry of this example is shown in Figure 2.1. FR4 ($\epsilon_r=4.5$) material was used between two solid planes. First, the entire geometry was peeled and partitioned into three building blocks. The blocks above and below the solid planes are the same. Thus, only two blocks were modeled independently. A SPICE model was constructed for each block. Then the SPICE model for the entire geometry was formed from the cascaded blocks, as shown in Figure 2.2. To obtain the element values of each SPICE model, a nodal-based admittance matrix was acquired from a CEMPIE simulation. Consequently, the Z-matrix for two external ports was derived from it. Also, the Z-matrix for the external ports can be

obtained from the SPICE model. Comparing these two Z-matrices, the lumped element parameters in the SPICE model can be calculated [29]. Initial values of the lumped elements were guessed. Then, the Matlab function FMINSEARCH was used to find a local minimum of the evaluation function, which is the sum of the squares of the differences between the S-parameter from a SPICE model and from a CEMPIE simulation. As an example, those parameters for blocks above and below the solid planes were found to be

$$\begin{aligned} L_s &= 1.17\text{nH}, \\ C_s &= 0.295\text{pF}, \\ G_s &= 0.00494\text{pS/rad}, \\ C_p &= 505\text{pF} \quad \text{and} \\ G_p &= 10.2\text{pS/rad}. \end{aligned}$$

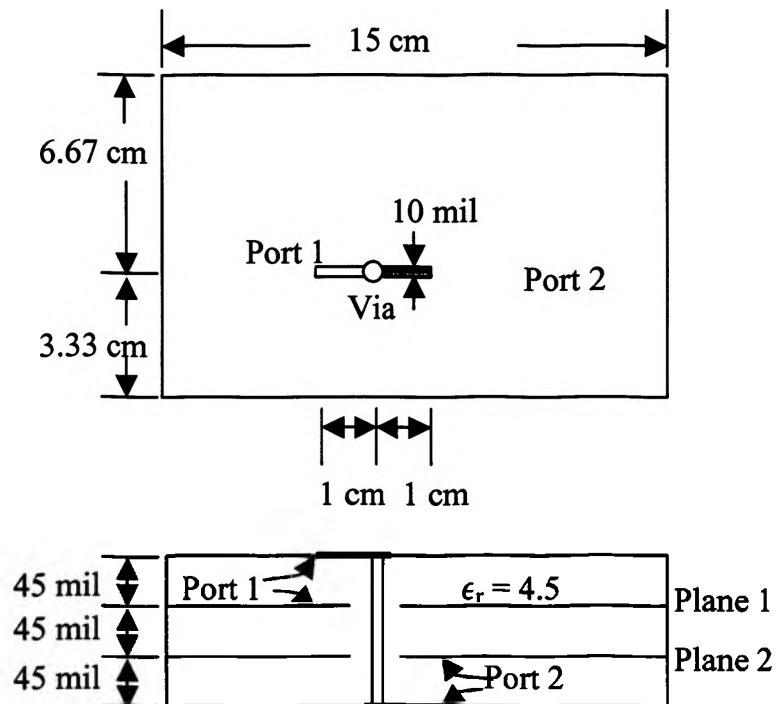


Figure 2.1. Geometry of a via transition for model extraction.

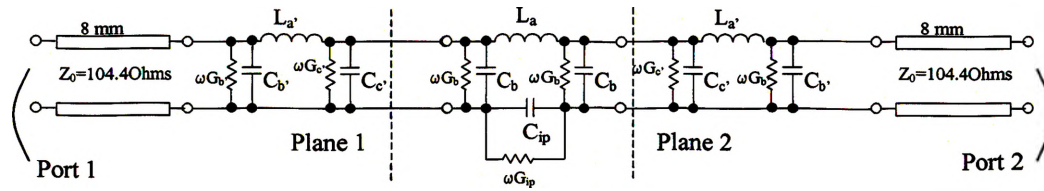


Figure 2.2. Complete SPICE model for the entire via transition shown in Figure 2.1.

The block between the two solid planes was modeled using the same method. S-parameters calculated using the CEMPIE simulation and the entire SPICE model agree closely as shown in Figure 2.3. The difference of $|S_{21}|$ is less than 1 dB up to 4 GHz. These results match well because the characteristic impedance of the transmission line is

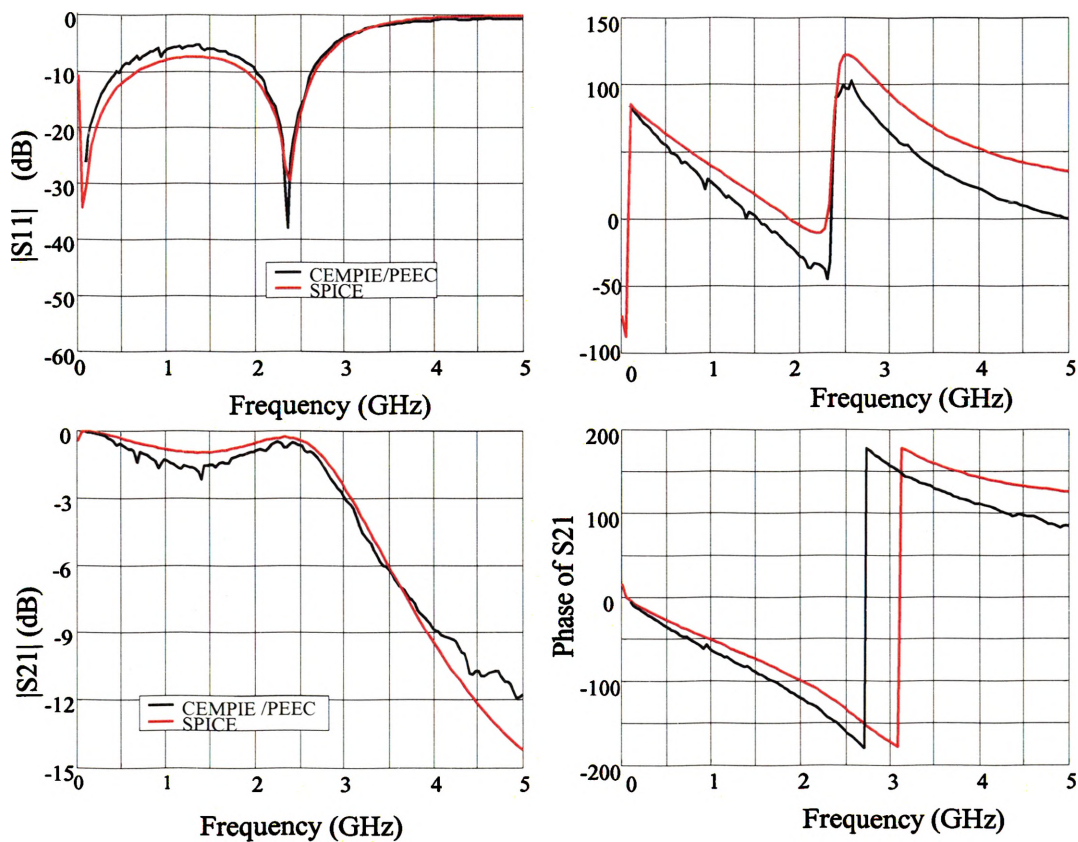


Figure 2.3. Comparison of modeled results for the geometry shown in Figure 2.1.

104 Ohms. So these two segments of transmission line dominate the behavior of the S-parameter. Had the characteristic impedance been 50 Ohm or had microstrip stubs been short, there would have been difficulties, which will be discussed in the following section.

2.3. LIBRARY MATRIX

An example of the library matrix for the standard 0.062'' 10-layer board was constructed for use in the procedure above in a real design environment. There are 6 building blocks shown in Figure 2.4.

Table 2.1 shows how to assemble the building blocks to model a particular via. As an example, consider a via connecting two signal lines located in Layer 3 and Layer 8. The model for this via can be constructed from Block E, B, C, B and E. Building block E, for example, only has one port and so it can only be assembled in one way. Building block A, in contrast, has two ports. The symbol A refers to a configuration in which port 1 is the external port connected to the microstrip traces and port 2 is the internal port connected to other via building blocks. The symbol \underline{A} denotes the same block connected so that port 1 acts as the external port and port 2 acts as the internal port as shown in Figure 2.5. Building block B contains three ports. The various connections to block B are denoted by a combination of superscripts and underscores. Specifically B^1 refers to a configuration for which ports 1 and 2 are in the signal path, while B^2 refers to a configuration for which ports 1 and 3 are in the signal path. Without an underscore (e.g. B^1), port 1 is assumed to be the input port. With an underscore (e.g. \underline{B}^2), port 1 is assumed to be an output port. These definitions are also shown in Figure 2.5.

2.4. PEELING PROCESS AND CHALLENGES

A π -network inductance and capacitance model was used to model building blocks. Only one inductor was used in each building block. The value of this inductor depends on the current distribution along the via body. However when a building block

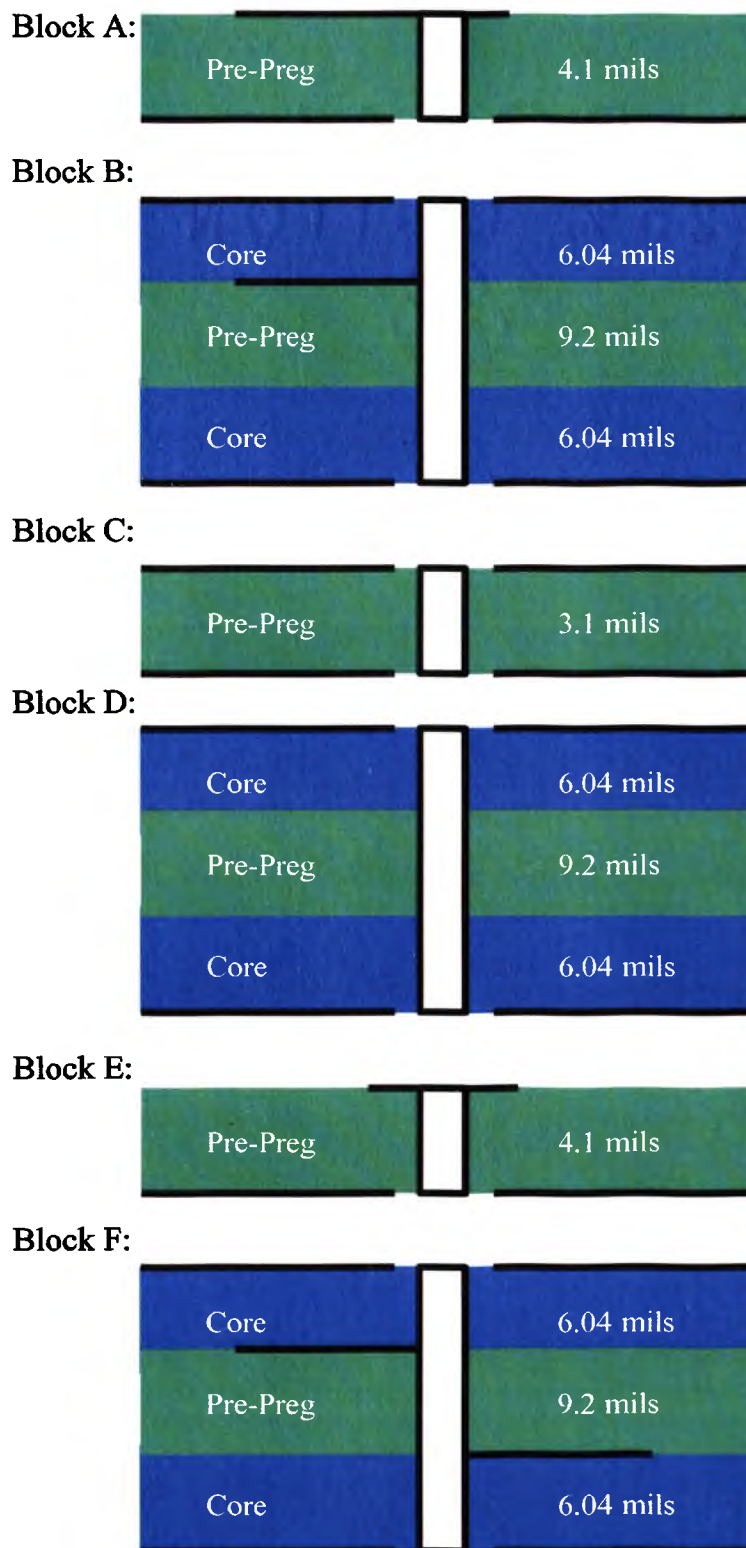


Figure 2.4. Building blocks for a standard 0.062" board.

Table 2.1. Library matrix for a 0.062" thick 10-layer printed circuit board

	1	3	4	7	8	10
1		AB^1CDE	AB^2CDE	$ADCB^1E$	$ADCB^2E$	$ADCDA$
3			$EFCDE$	EB^1CB^1E	EB^1CB^2E	$EBCDA$
4				EB^2CB^1E	EB^2CB^2E	$EBCDA$
7					$EDCFE$	$EDCB^1A$
8						$EDCB^2A$
10						

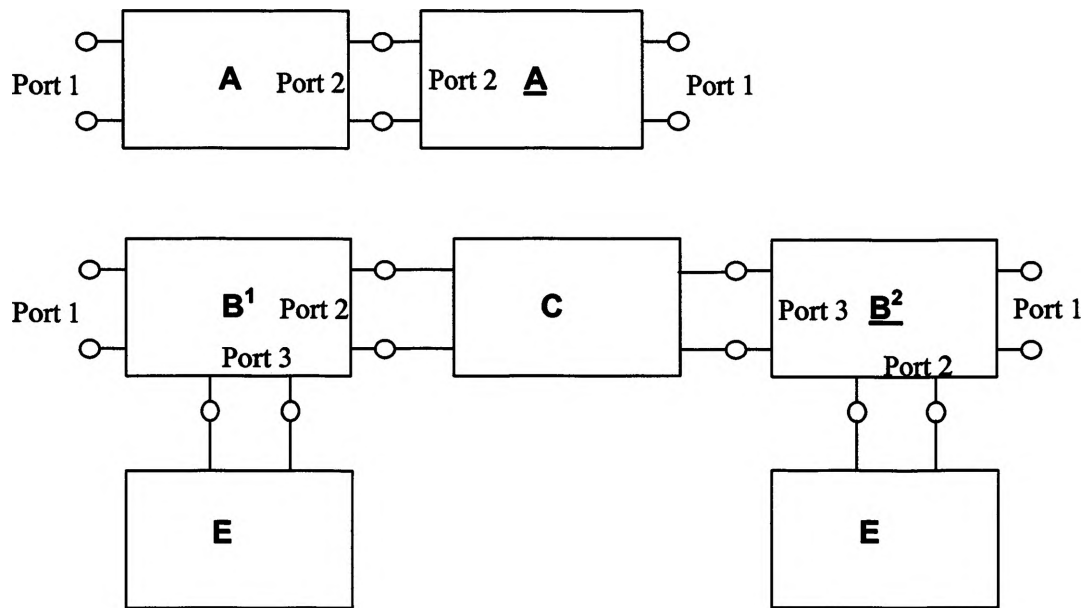


Figure 2.5. The meanings of underline and superscript in the library matrix.

was modeled independently, almost all the current flows vertically along the via body. The original CEMPIE with simplified basis functions, which forced the current flow vertically along vertical metal surfaces, could model these building blocks accurately.

When different building blocks are cascaded together, the current distribution will be different than with an isolated building block. When the original CEMPIE code was used to model the entire via transition on a multi-layer board, an artificial inductor had to be put between every two blocks when building blocks were cascaded together to compensate for the effect of current redistribution.

An example of a via transition for single-ended signaling is shown in Figure 2.6. A via passes through all layers of a 4-layer, 3 cm by 2 cm board. Figure 2.6(a) shows the side view of this structure. The mesh patterns used in CEMPIE are shown in Figure 2.6(b) and (c). After every block was modeled independently, compensation inductances were put between every two connected blocks as shown in Figure 2.7.

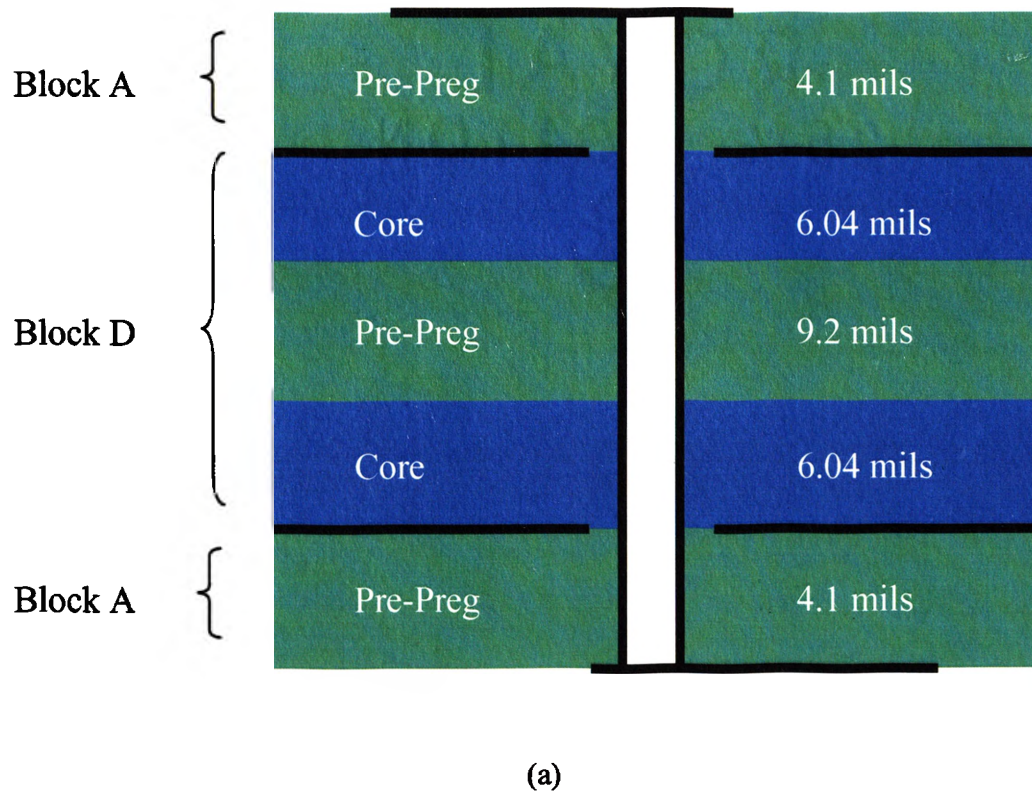
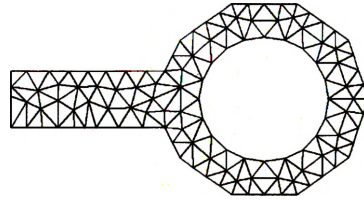
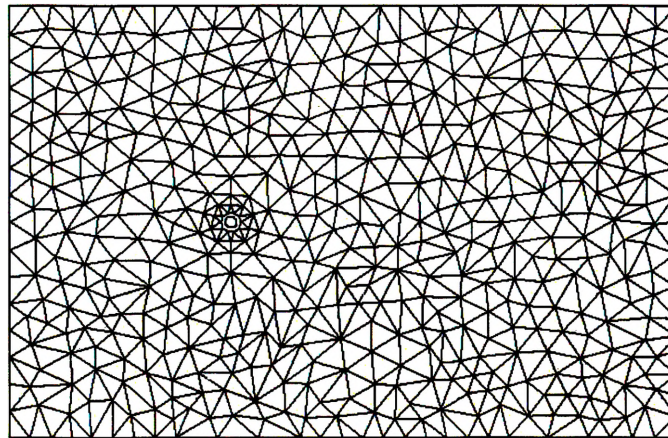


Figure 2.6. Via geometry and mesh patterns, (a) Side view of a via through a four-layer board; (b) Mesh pattern of top and bottom layer; (c) Mesh pattern of two middle layers.



(b)



(c)

Figure 2.6. Via geometry and mesh patterns, (a) Side view of a via through a four-layer board; (b) Mesh pattern of top and bottom layer; (c) Mesh pattern of two middle layers.
(cont.)

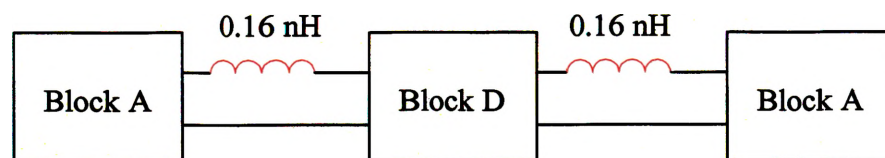


Figure 2.7. Blocks and compensating inductances.

Figure 2.8 shows the simulation results of the original CEMPIE for an entire geometry, a cascaded block A-D-A model without compensating inductance; and the same model with compensating inductances. The value of the compensation inductance was estimated by curve fitting. The cascaded results were calculated from the S-parameters of blocks directly. The cascaded results were calculated from the S-parameters of blocks directly. The S-parameters were transformed to ABCD parameters. Then, ABCD parameters were multiplied together. Finally, The ABCD parameters of combined three blocks were transformed back to S-parameters. S_{11} shows some large differences at the resonant frequencies around 2.1 GHz and 5 GHz.

2.5. SIGNIFICANCE OF THE TRANSVERSE CURRENT

The impact of the transverse current and overall current distribution in the partitioning and peeling process; the relationship between the current distribution along a via body; and the equivalent inductance of the via were investigated. Several cases were also simulated using CST Microwave Studio (MWS) for comparison with the CEMPIE tool being used. The first case had two Block A's (see Figure 2.4(a)) connected together as shown in Figure 2.9. In this case both the input and output signal traces were located on the left side of the via. The magnitude of the magnetic field at 2GHz were simulated for three cross-sections using MWS. Figure 2.10 shows a top view of the magnitude of the H-field at 2 GHz over the cross-section A-A'. Figure 2.11 shows the H-field on the cross-section B-B', and Figure 2.12 shows the H-field on the cross-section C-C'. These three figures illustrate that the current distribution does not change or changes only minutely along the via body in this case. Furthermore, there is no y component of the H-field, i.e., transverse current, along the via body, which is shown in Figure 2.13. This indicates that there is almost not any transverse current in this case. The CEMPIE tool can model this case accurately, because the tool correctly enforces the current flow vertically along the via body. The comparison between the cascaded result and the simulation for the entire geometry agrees well, both with MWS and CEMPIE modeling as shown by the blue and black curves in Figure 2.14.

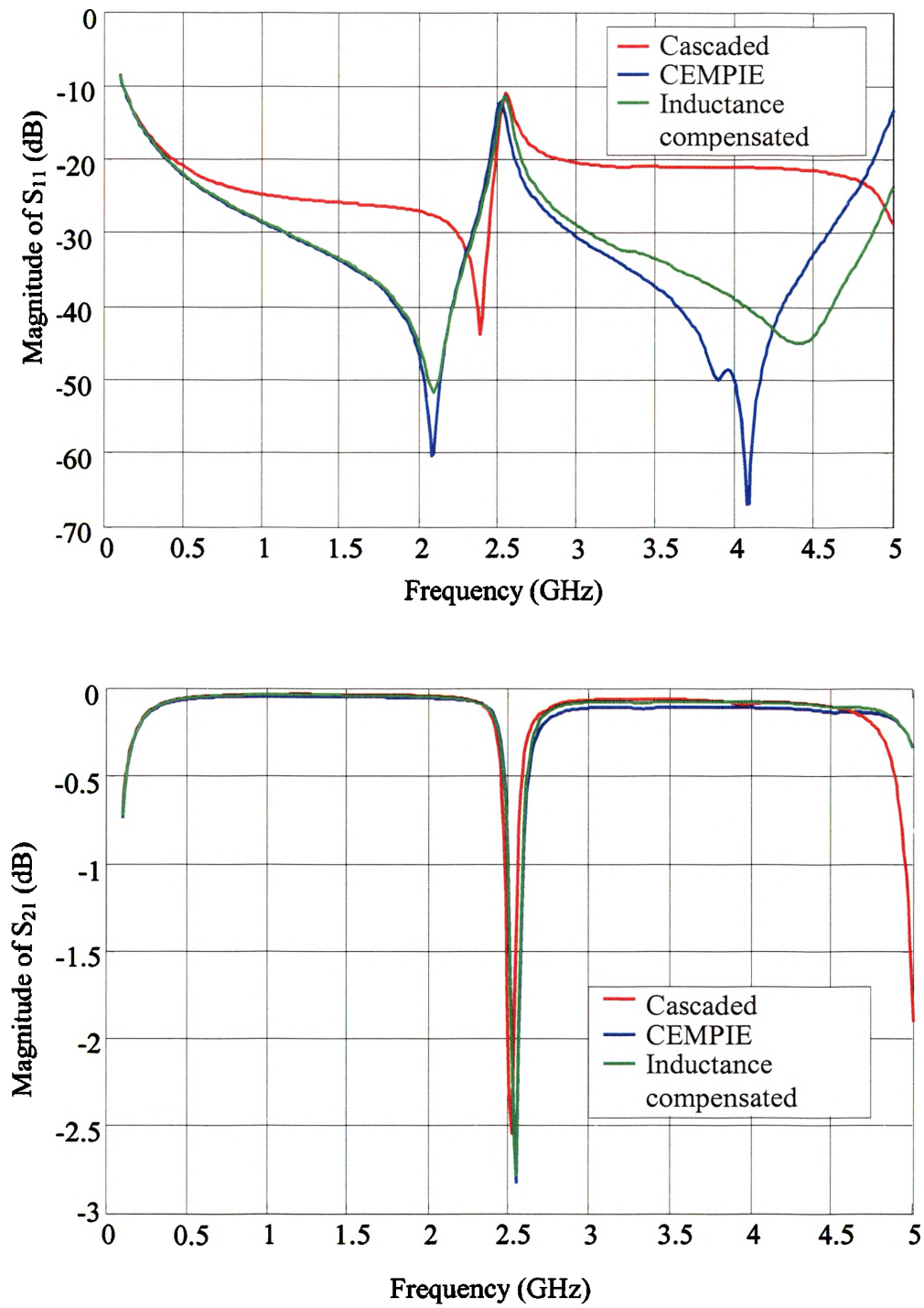


Figure 2.8. Simulation results using the original CEMPIE for single-ended case.

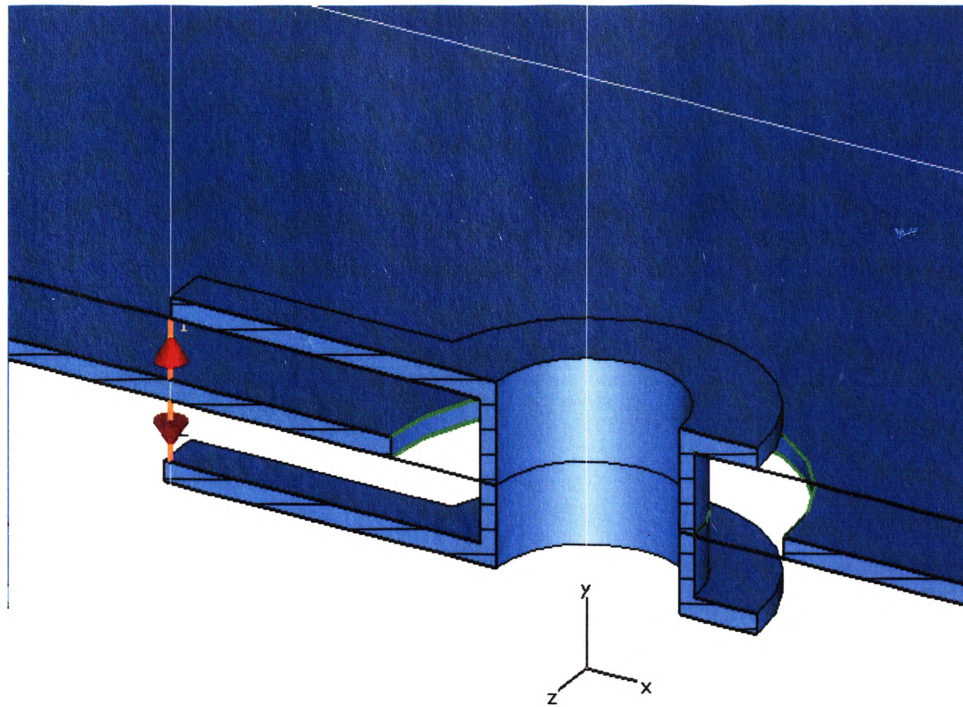
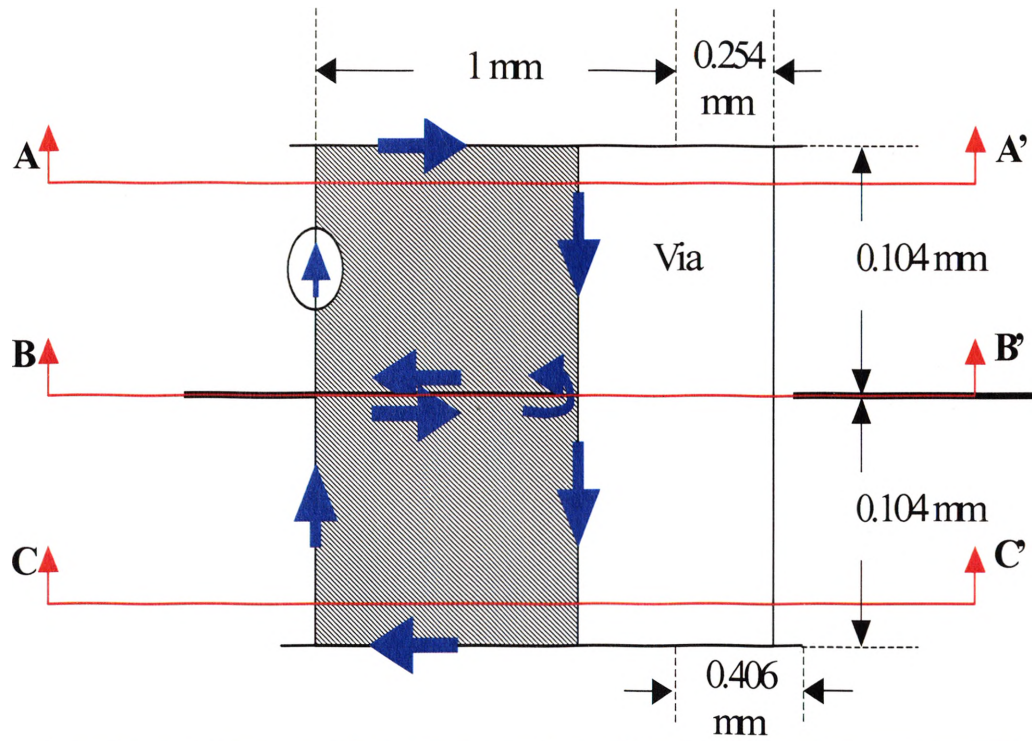


Figure 2.9. Side view of Block A-A (signal from left side goes back to left side of the via).

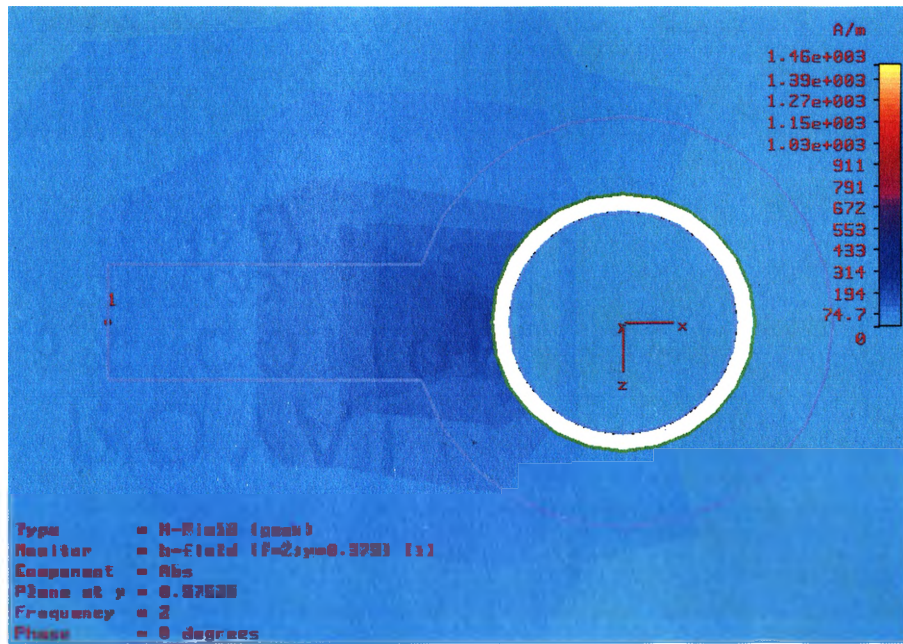


Figure 2.10. Magnitude of H-field at 2 GHz over the cross-section A-A' from MWS.

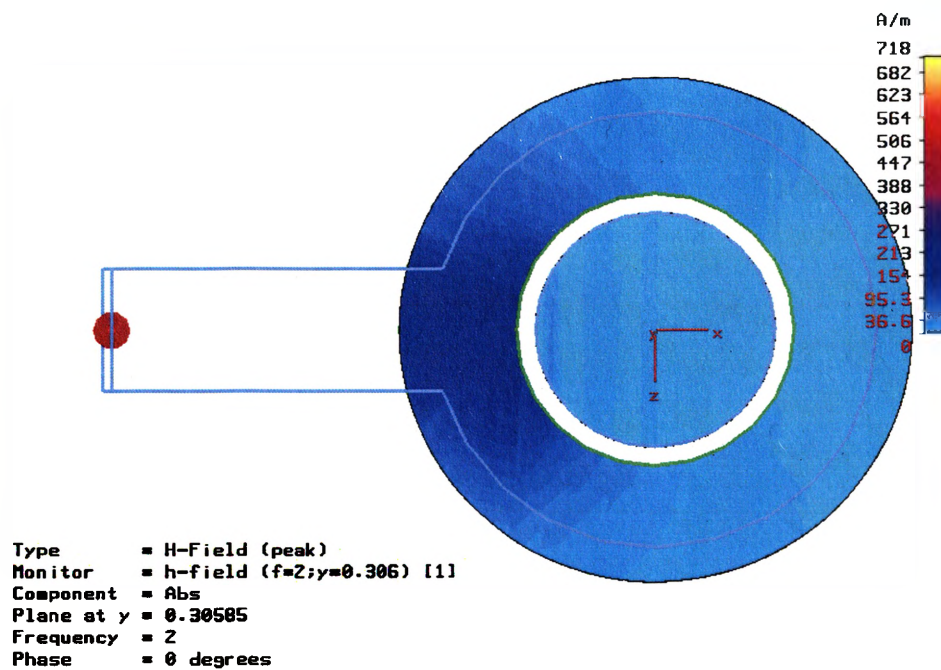


Figure 2.11. Magnitude of H-field at 2 GHz over the cross-section B-B' from MWS.

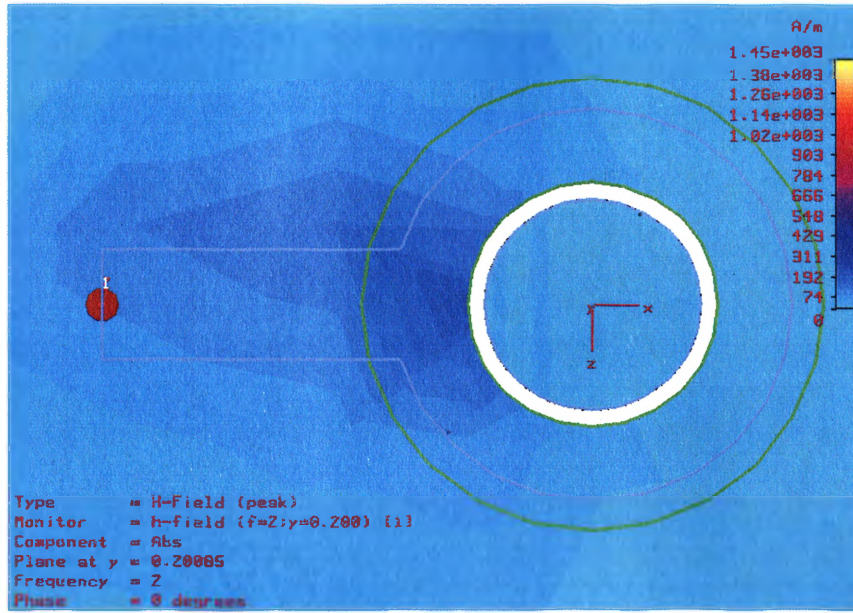


Figure 2.12. Magnitude of H-field at 2 GHz over the cross-section C-C' from MWS.

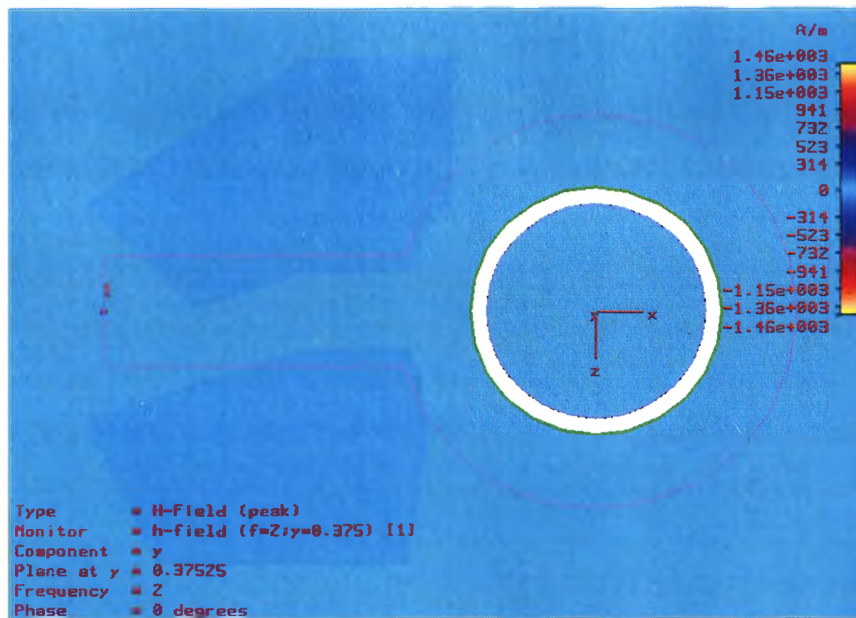


Figure 2.13. Y component of H-field (associated with transverse current) at 2 GHz over the cross-section A-A' from MWS.

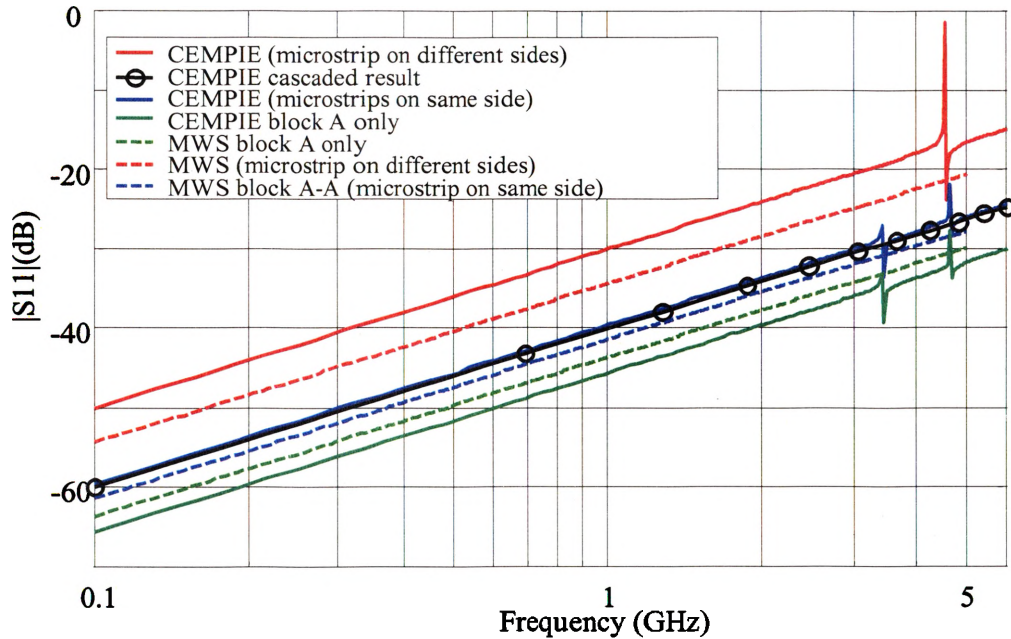


Figure 2.14. Comparison of some simulation results.

However, when the input signal goes in one side and the output exits the via transition on the opposite site, as shown in Figure 2.15, the current distribution changes along the via body as illustrated in Figure 2.16 and Figure 2.17. In the top block, most of the current is concentrated at the left side of the via, while a small part of it flows along the right side of the via. This differs from the current distribution in Figure 2.9, and the current distribution when block A is modeled independently. In this case, the original CEMPIE simulation results in a significant error due to the inaccurate modeling of inductance associated with the via. Figure 2.18 and Figure 2.19 show clearly the horizontal current existing in this case. The original CEMPIE tool did not model this case accurately as shown in Figure 2.14, by the red curves. The difficulty is that the old basis functions in the numerical formulation do allow for transverse currents on planes but not on vertical structures. Further, the analysis of the two cases above clearly demonstrates that an understanding of the current distribution at a discontinuity is critical for model extraction, as can be seen by comparing the black curve for the cascaded result

of two Block A's, with the red and blue curves in Figure 2.14, where the blue curves are for the case with the input and output on the same side, and the red for input and output signal on opposite sides. A partitioning process that does not incorporate the current distribution through the discontinuity correctly will not result in an accurate model.

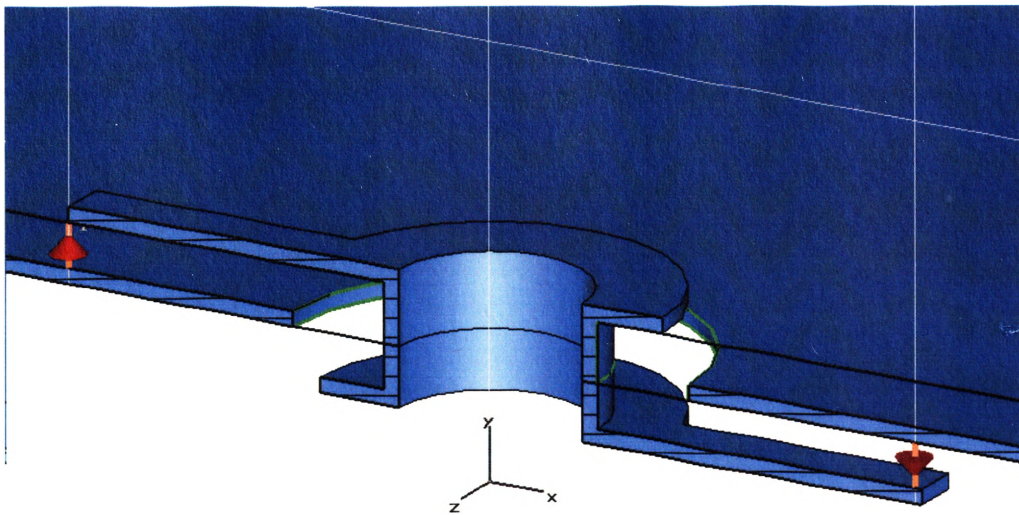
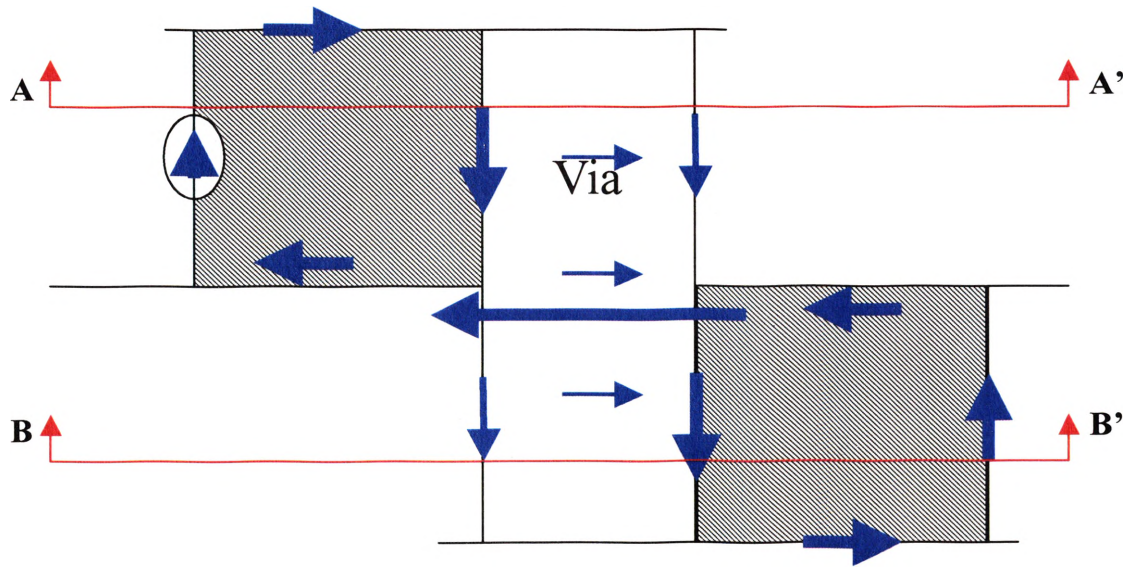


Figure 2.15. Side view of Block A-A (signal from left side goes to right side of the via).

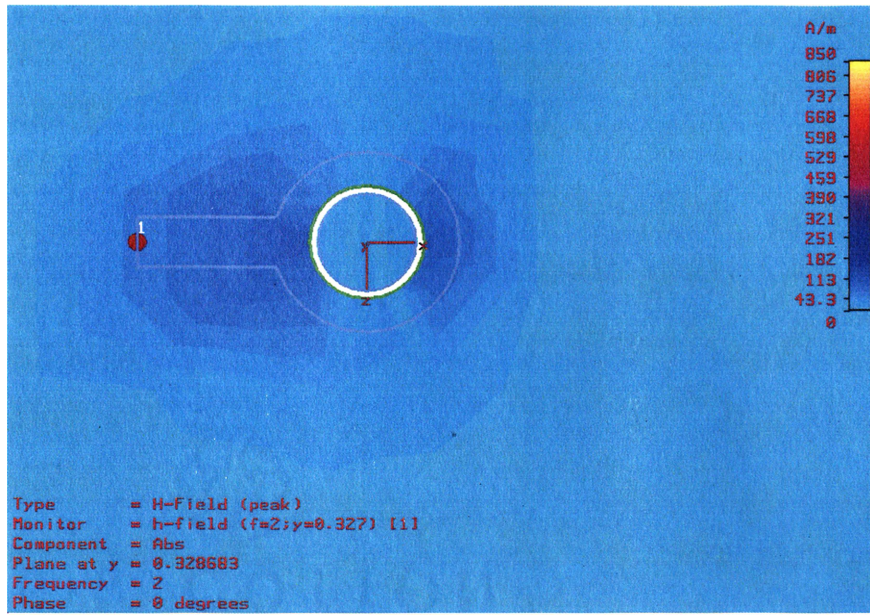


Figure 2.16. Absolute magnitude of H-field at 2 GHz on the cross-section A-A' from MWS.

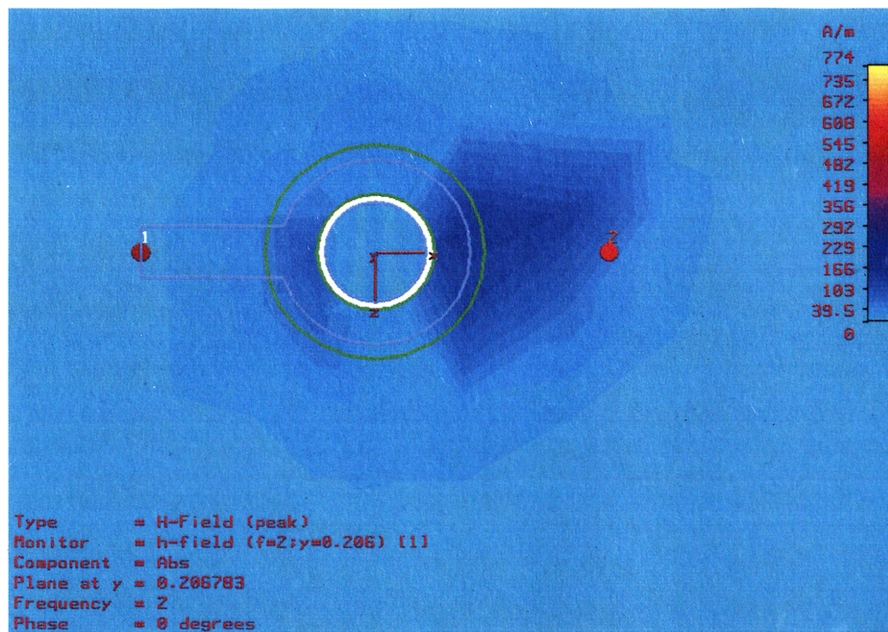


Figure 2.17. Absolute magnitude of H-field at 2 GHz on the cross-section B-B' from MWS.

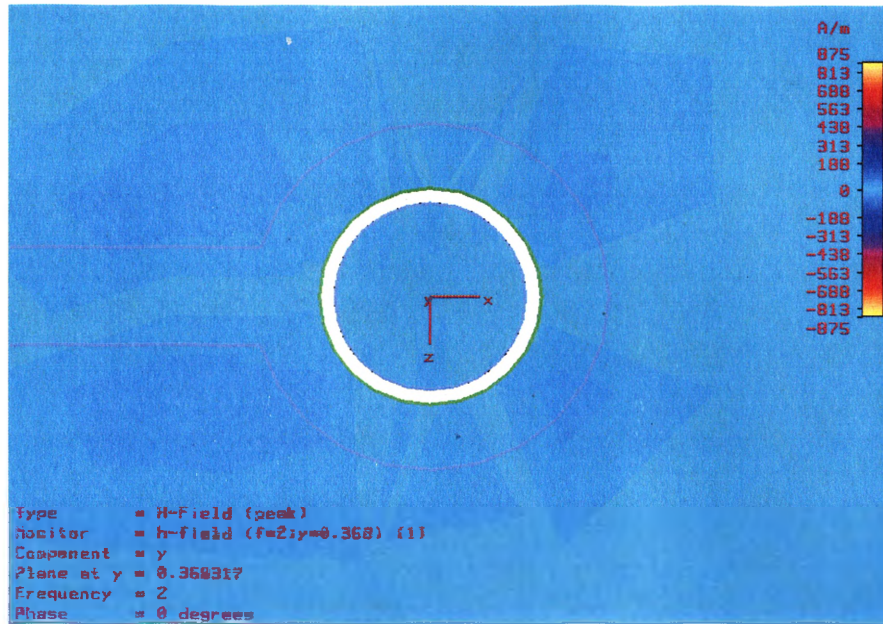


Figure 2.18. Y component of H-field (associated with transverse current) at 2 GHz on the cross-section A-A' from MWS.

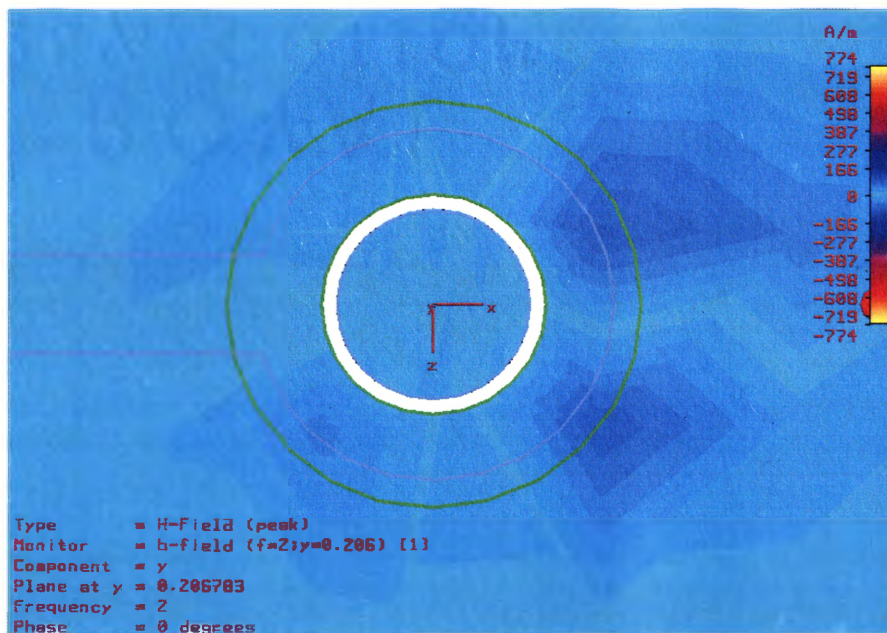


Figure 2.19. Y component of H-field (associated with transverse current) at 2 GHz on the cross-section B-B' from MWS.

The via transition problem investigated above clearly demonstrates that partitioning a discontinuity into constituent blocks requires considerable fidelity in achieving the correct current distribution within each individual block, as compared to that with the overall structure, in order to develop an accurate library.

2.6. NEW BASIS FUNCTIONS FOR CEMPIE

In order to model the transverse current in vertical metal surface to acquire the accurate parasitic inductance associated with via body, an improved basis functions was developed to incorporate the horizontal edges as parts of current basis.

The simulation results using CEMPIE with improved basis functions are shown in Figure 2.20 and Figure 2.21. From the figures, one observes that the simulation results of entire geometry and the cascaded results matched very well with 3dB difference for S_{11} and less than 0.05 dB for S_{21} . Figure 2.20 and Figure 2.21 also compared the CEMPIE simulation results with another commercial full-wave tool using finite integral technique for the validation purpose. There is a very good agreement between these two full-wave simulation results.

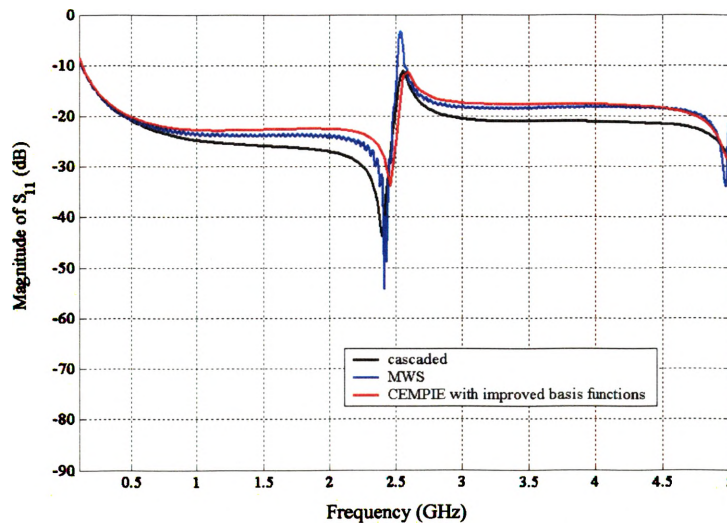


Figure 2.20. Modeling results— S_{11} using CEMPIE with the improved basis functions.

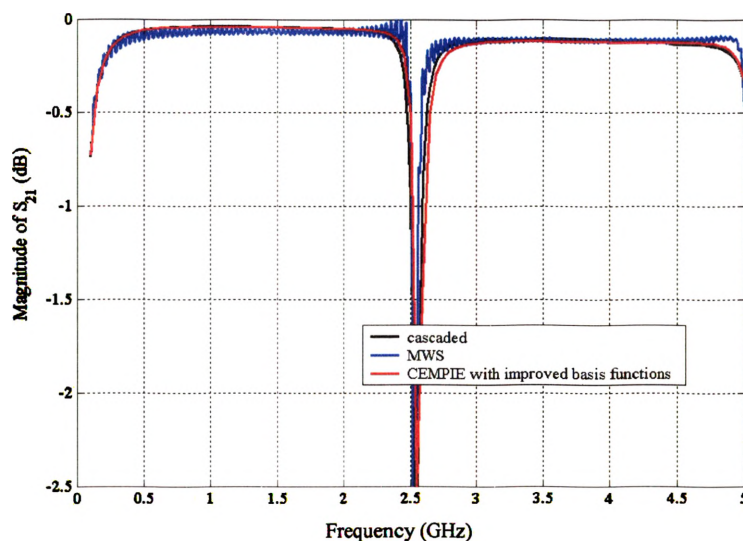


Figure 1.14. Modeling results— S_{21} using CEMPIE with the improved basis functions.

2.7. EYE-DIAGRAM SIMULATION

In practice, time domain simulations are more common in the design of high speed digital data links than frequency domain simulations. Therefore, the effectiveness of the circuit model on a time domain simulation was investigated. Figure 2.22 shows the eye diagrams of via transition in Figure 2.6. The eye diagrams were produced with the 2 GBit/s input bit rate, 50 ps rise time (20%-80%), 3EB05H (comma, comma bar) as the format of bit pattern. The bit pattern formed the pseudo-random bit sequence. Then, it was transformed to the frequency domain and multiplied by the transfer function $F = S_{21}/(1+S_{11})$. The output signal was transformed back to time-domain using inverse discrete Fourier Transform. The eye-diagrams were formed then by cutting and overlapping the time-domain output signal. Here the presumption is that both source termination and load termination are matched. The eye diagrams produced using the above procedure is shown in Figure 2.22. The property of the signal quality can be easily quantified by eye widths, eye openings and the jitter. These results show that the SPICE models in the library matrix are good for engineering studies of the impact of via transition on signal integrity.

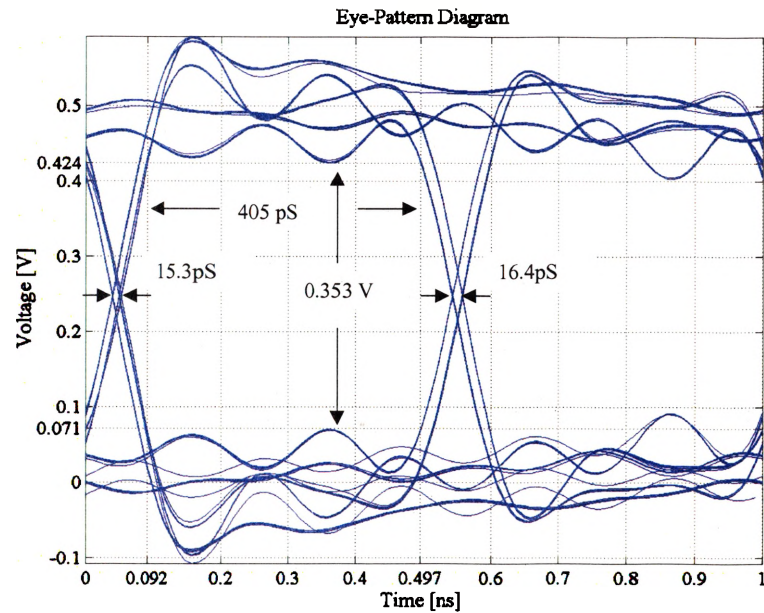


Figure 2.21. Eye-diagram simulated using the circuit model of the via.

2.8. CONCLUSION

In this section, a method to build a SPICE model library for via transition on single-ended signaling has been presented. For a given stackup of PCB, a SPICE model library for via transition can be built using the CEMPIE and every via on the board can be modeled by a few cascaded blocks in this library. It was shown that the transverse current plays a significant role on the modeling of via transition, especially for the estimation of accurate value of parasitic inductance of via body.

3. VIA MODELS FOR DIFFERENTIAL SIGNALING

In high-speed digital designs, signal via transitions on printed circuit boards (PCBs) are becoming an important signal integrity issue. As the data rates increase into the multi-giga-bit per second range, via transitions can degrade the signal. Efficient and accurate models for via transitions are necessary for high bit-rate digital circuit system designs. Further, these models should be compatible with fast simulation tools.

3.1. INTRODUCTION

A number of models for differential vias have been published. The method in [33] and [34] modeled the coupled vias as a cascade of capacitances and inductances. A 3-D electrostatic solver was used to calculate the capacitances while the formula of a bifilar transmission line was applied to computation of the inductance values. Another method in [35] modeled vias in differential transmission lines as transmission line segments. A layer peeling process was proposed to model via transitions of single-ended signaling on multi-layer PCBs in [36] and [37]. In this section, this procedure was used to model the via pair for a differential signal pair. SPICE models for various vias on a specified PCB stackup are constructed by cascading “building blocks”, which are SPICE models for elements of the via structure. Full-wave numerical modeling was used to simulate the 4-port S-parameters of these “building blocks”.

3.2. PEELING AND PARTITIONING METHOD FOR VIA PAIR ON DIFFERENTIAL SIGNALING

It was shown in the previous work that single-ended via transition in the multi-layer PCBs could be modeled using a peeling and partitioning process[36] [37]. A via is segmented into several parts, and each part is modeled as a SPICE passive network. The various via transitions in a practical design can be modeled by putting these basic building blocks together. This method is denoted as a peeling and partitioning process in this paper. The models of these parts are called “building blocks” or “blocks”. Solid planes inside the PCBs were used as natural boundaries for separating the blocks of a via. Similarly, this process was applied to build the via model library for differential

signaling. The main advantage of the layer peeling process is that it has the flexibility to model various via transitions connecting signal lines on different layers using a few SPICE building blocks. It decreases the requirement of time and complexity of full-wave simulation for model extraction. For a through-hole via differential signal pair, the via model library includes only four kinds of building blocks: the transition between coupled microstrip lines and differential via pair (Block A in Figure 3.1), the differential via pair across two solid planes (Block D), the transition between coupled striplines and a differential via pair (Block B), differential via stubs (Block C). At first, simple combinations of blocks associated with the geometry variation were simulated using full-wave tools to acquire n-port S-parameters. Then a physics-based SPICE model for each block was built. The values of these elements were extracted by fitting the mixed-mode S-parameters from full-wave models.

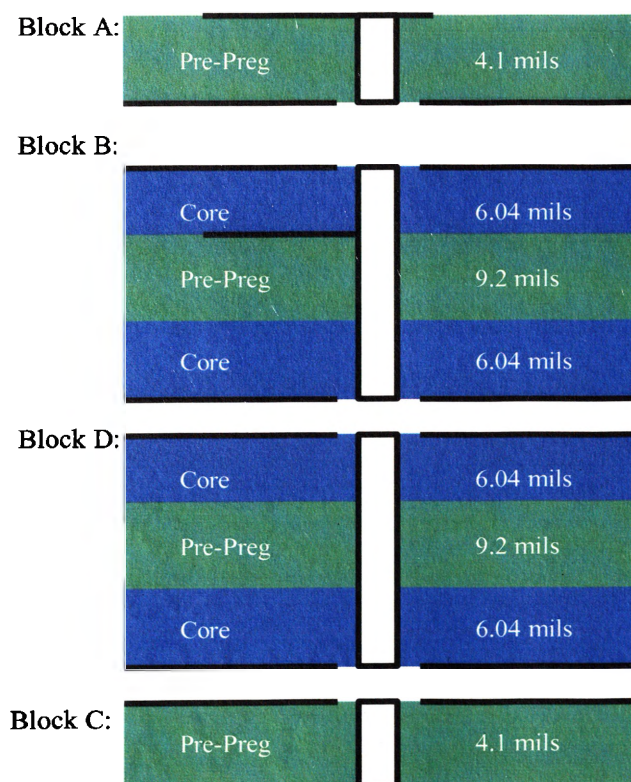


Figure 3.1. Basic blocks for a 10-layer PCB.

3.3. BUILDING BLOCKS AND SPICE MODELS

For a multi-layer PCB, there are four basic blocks, which are shown in Figure 3.1. Block A is the transition between coupled microstrip lines and differential via pair, Block B is the transition between coupled striplines and differential via pair, Block C describes differential via stubs and Block D represents the differential via pair across two solid planes.

The circuit model for Block A is shown in Figure 3.2. Basically it is two coupled π -shape circuit networks. C_1 models the capacitance between the microstrip stub and the reference plane; C_2 represents the capacitance between the via body and reference plane; C_{m1} and C_{m2} model the capacitive coupling between two vias; and M models the inductive coupling between two vias.

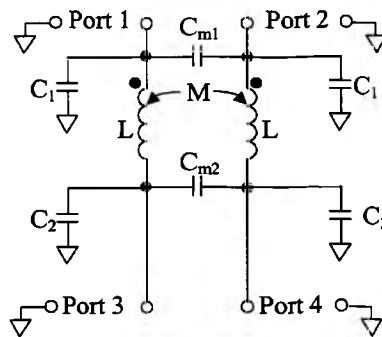


Figure 3.2. Circuit model for Block A.

Because Block B has six ports and two reference planes, it needs two different models. One is for the geometry when signals come from the top layer and the ports on the bottom layer are connected to via stubs as shown in Figure 3.3. Another one is for the situation when signals come from the bottom layer and the ports on the top layer are connected to via stubs as shown in Figure 3.4. In Figure 3.3, Port 1, 2, 5 and Port 6 share one reference plane, and Port 3 and Port 4 use another reference plane. C_{ip} represents the inter-plane capacitance between two solid planes. In Figure 3.4, Port 1 and Port 2 share one reference plane, and Port 3, 4, 5 and Port 6 use another reference plane.

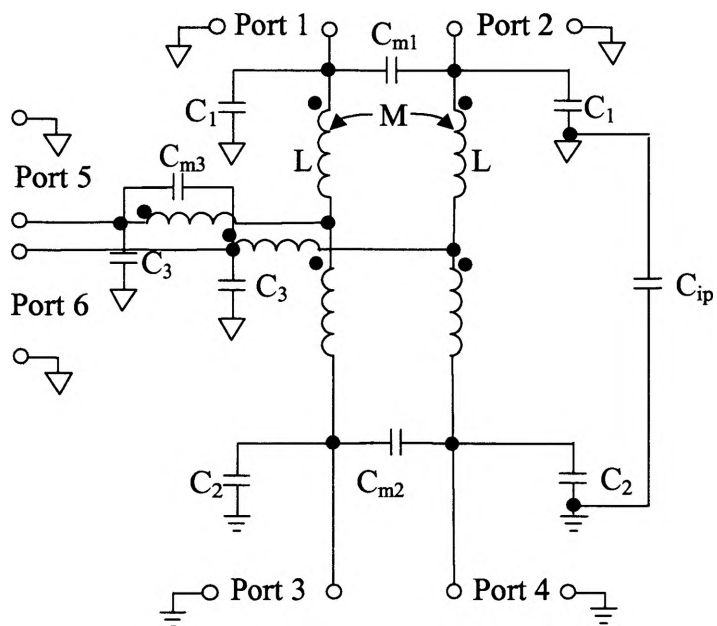


Figure 3.3. Circuit model for Block B when signal makes reference to the top layer.

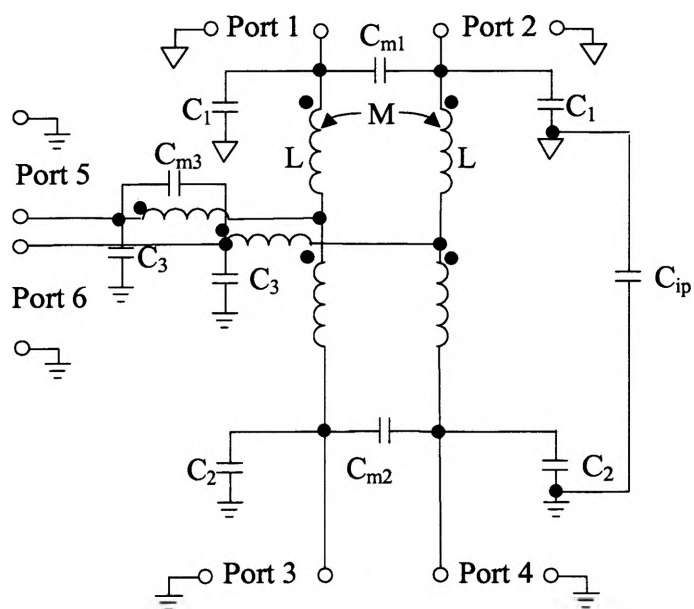


Figure 3.4. Circuit model for Block B when signal makes reference to the bottom layer.

Block C can be seen as Block A with one solid reference plane only. The circuit model is similar to Block A, but the difference is that there are two ports only as shown in Figure 3.5.

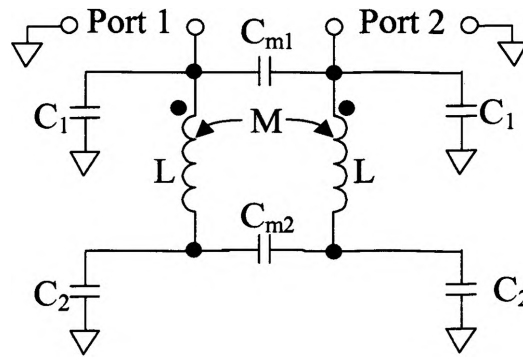


Figure 3.5. Circuit model for Block C.

As discussed in the previous sections, Block D can be model as circuit shown in Figure 3.6. The Z_{in} is the input impedance of two reference planes. If the distributed behaviors of powerbus are neglected, it may be modeled as a capacitor only.

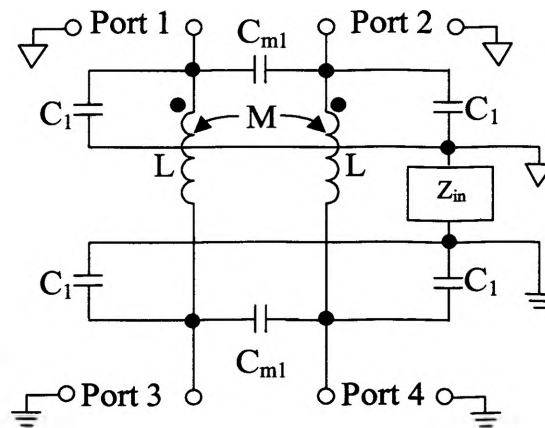


Figure 3.6. Circuit model for Block D.

To minimize the discontinuity of differential signaling, the shape and sizes of anti-pads were engineered using 2-D analysis to set the differential-mode characteristic impedance of the via pair as 100 Ω . Then the geometries of all blocks for the 10-layer board are determined as shown in Table 3.1 and Figure 3.7 -- Figure 3.16.

Table 3.1. Geometry data sheet of blocks

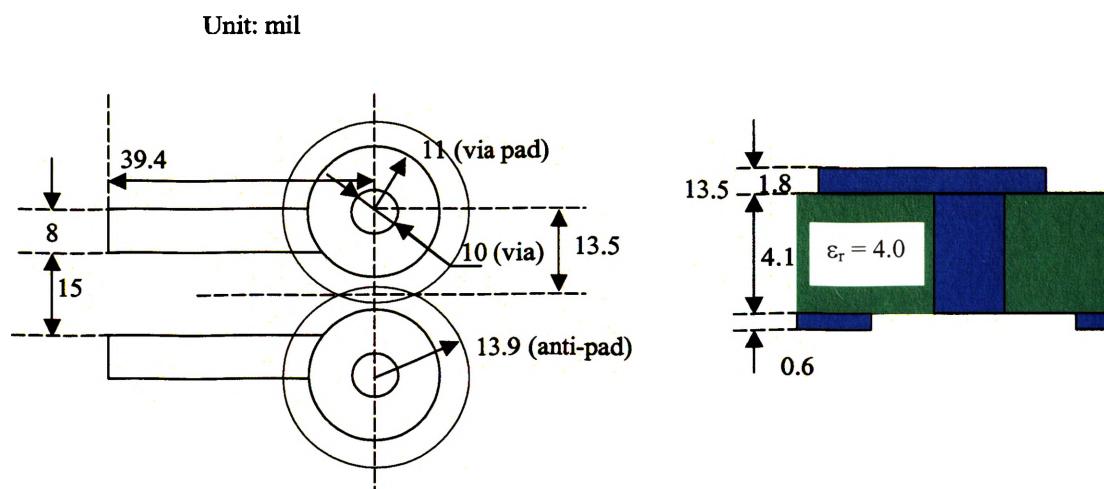
	Through Hole Via Diameters (mils)	Spacing between two vias (mils)	Differential Impedance (Ohm)	index
Block A	10	27	100	1
	16	44	100	2

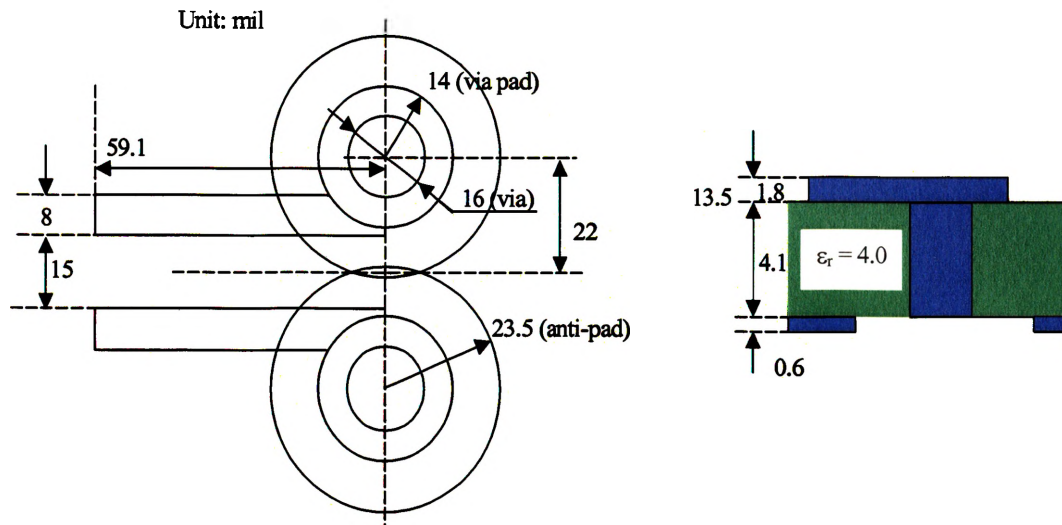
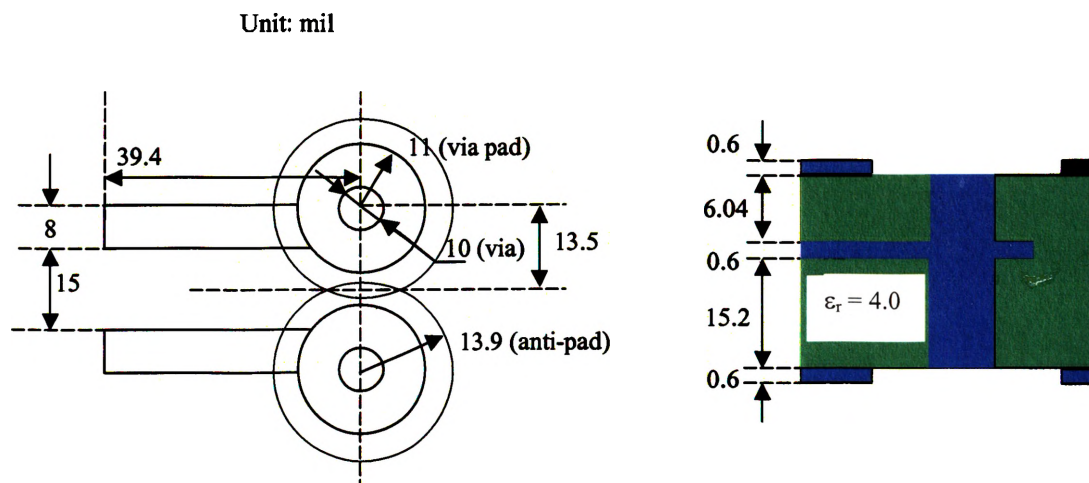
	Through Hole Via Diameters (mils)	Spacing between two vias (mils)	Differential Impedance (Ohm)	index
Block B_up	10	27	100	3
	16	44	100	4

	Through Hole Via Diameters (mils)	Spacing between two vias (mils)	Differential Impedance (Ohm)	index
Block B_down	10	27	100	5
	16	44	100	6

Table 3.1. Geometry data sheet of blocks (cont.)

	Through Hole Via Diameters (mils)	Spacing between two vias (mils)	index	
Block C	10	27	7	
	16	44	8	
	Through Hole Via Diameters (mils)	Spacing between two vias (mils)	Thickness of dielectric layer (mils)	index
Block D	10	27	21.28	9
			3.1	10
	16	44	21.28	11
			3.1	12

Figure 3.7. Geometry of Block A₁.

Figure 3.8. Geometry of Block A₂.Figure 3.9. Geometries of Block B₃ and B₅.

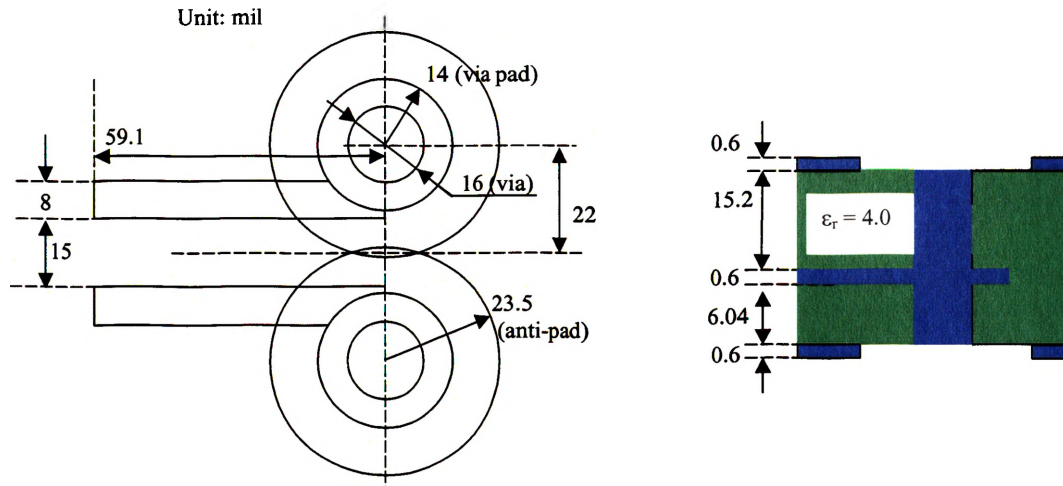


Figure 3.10. Geometries of Block B₄ and B₆.

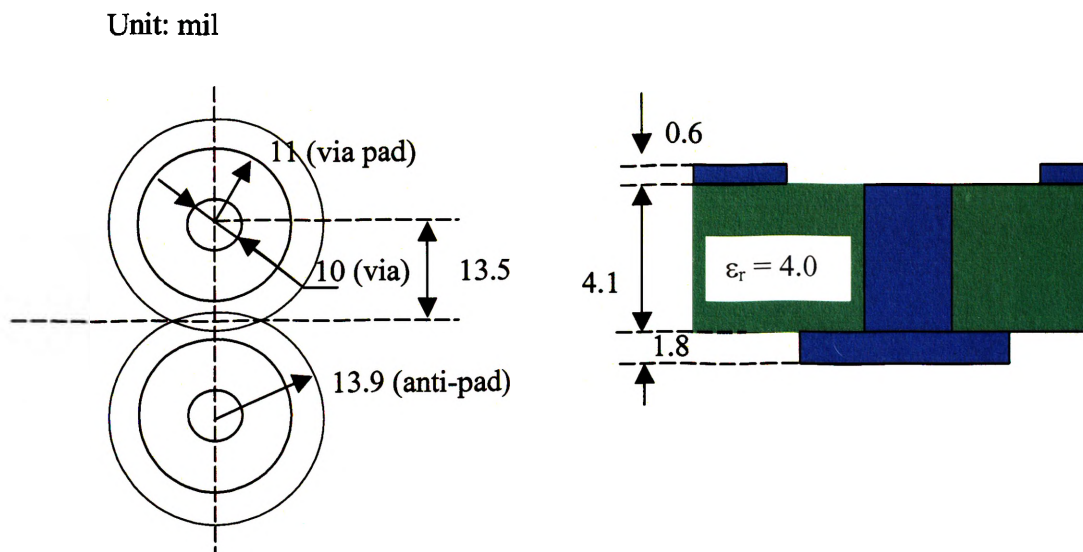
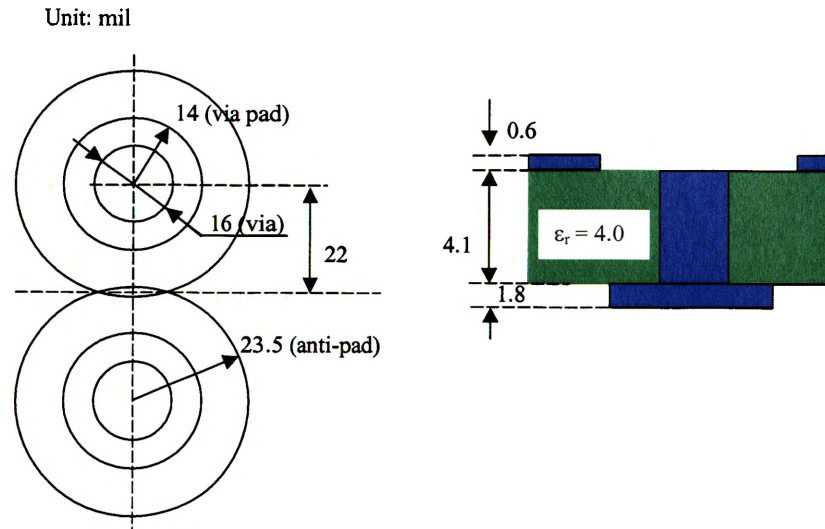
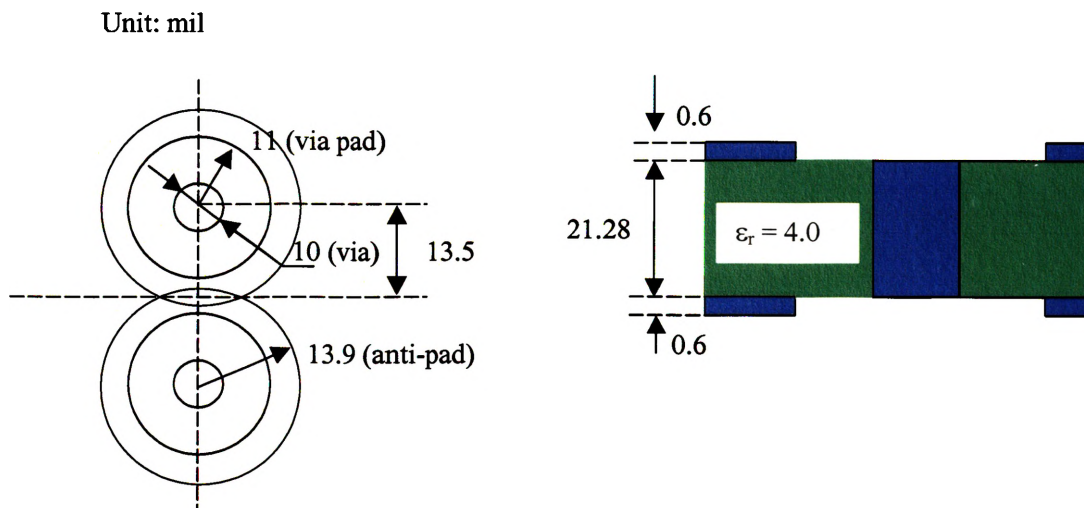
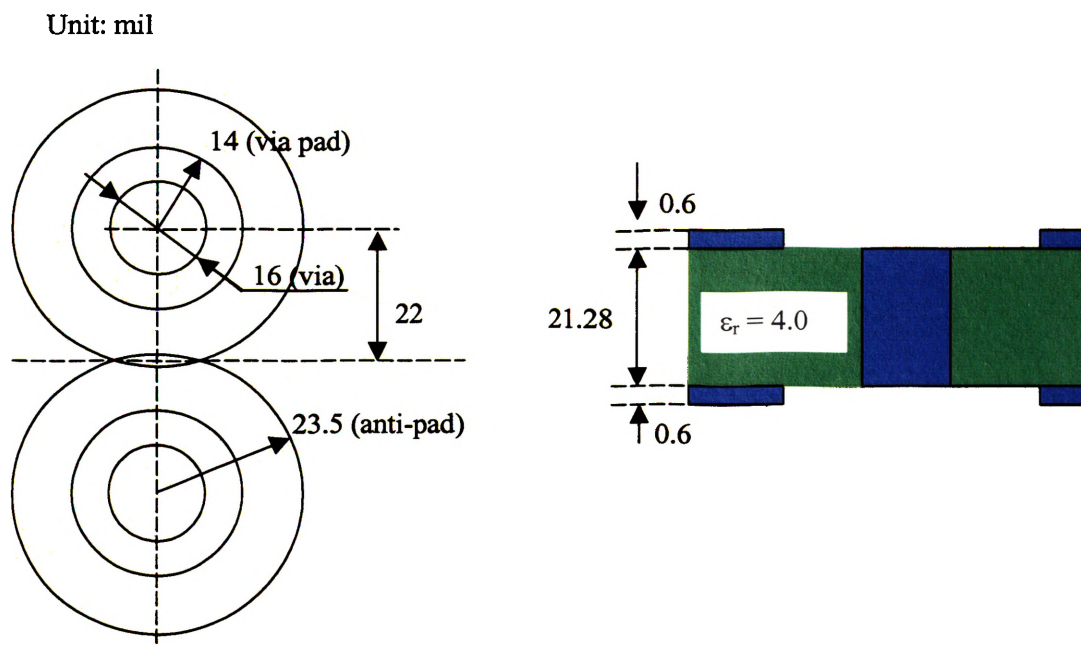
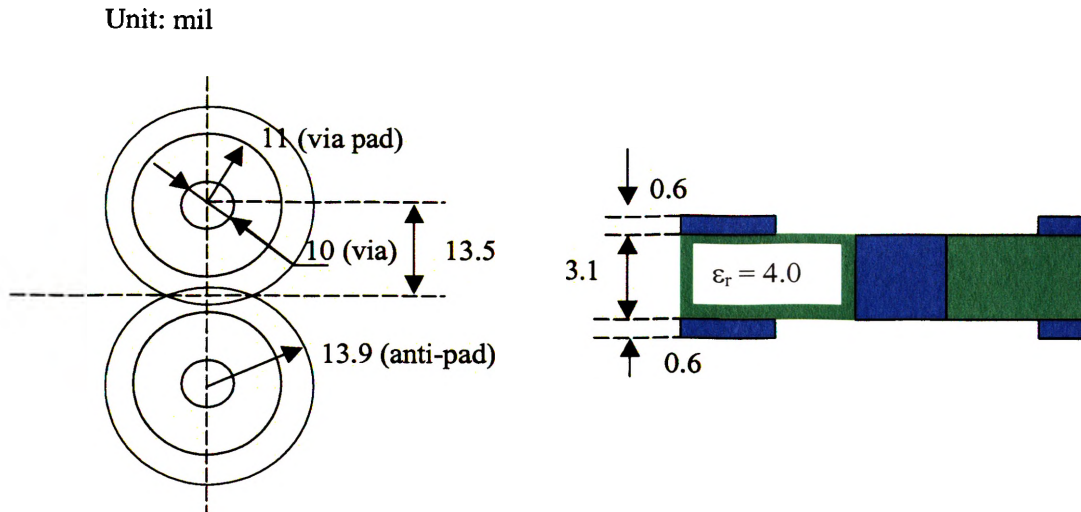


Figure 3.11. Geometry of Block C₇.

Figure 3.12. Geometry of Block C₈.Figure 3.13. Geometry of Block D₉.



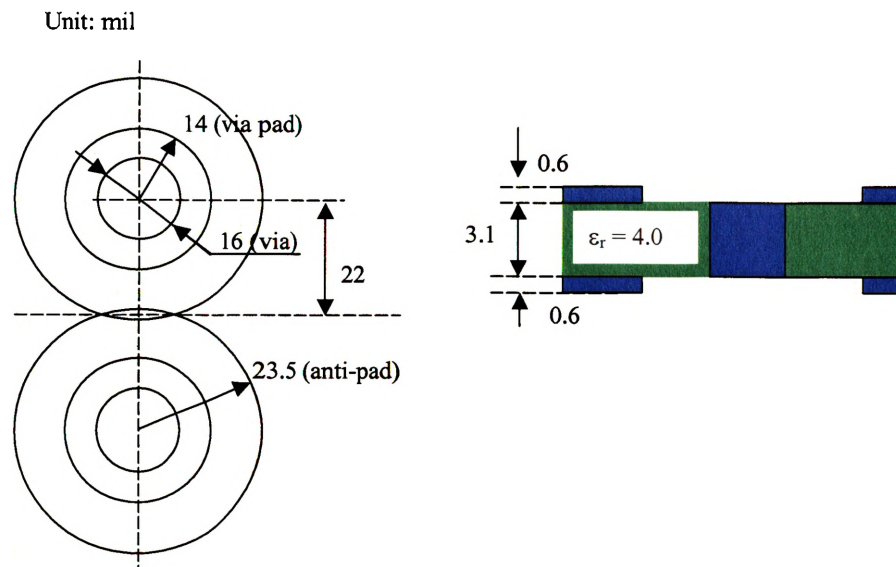


Figure 3.16. Geometries of Block D_{12} .

3.4. EXTRACTION OF MODEL PARAMETERS

The geometry used to extract parameters of Block A_1 is shown in Figure 3.17, which includes two Block A_1 and forms a three-layer structure.

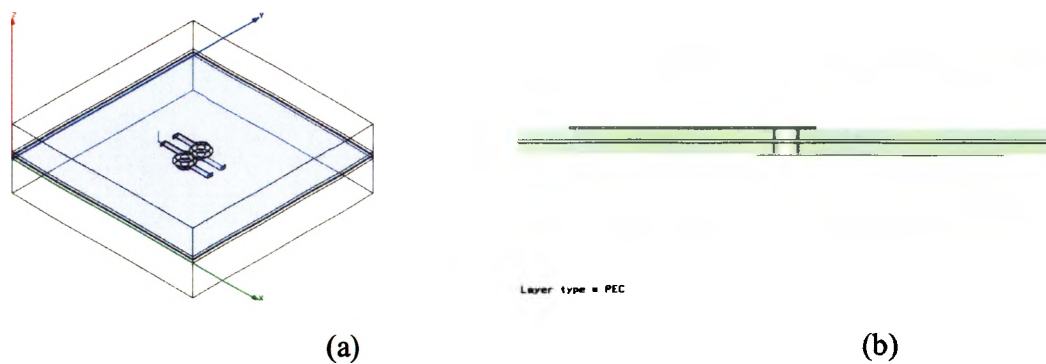


Figure 3.17. The geometry used to extract the parameters of Block A_1 . (a) perspective view, (b) side view.

The objective function used in the optimization procedure is

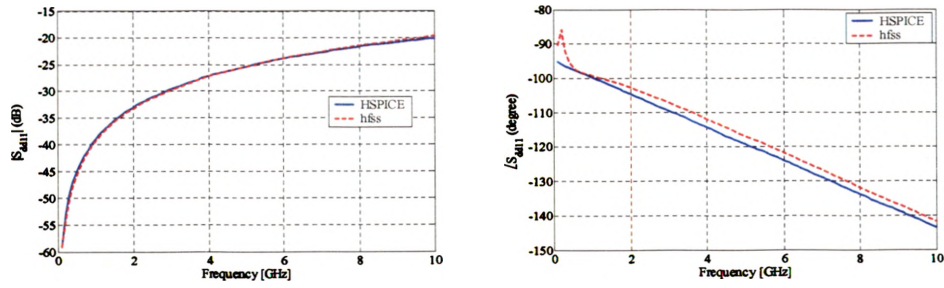
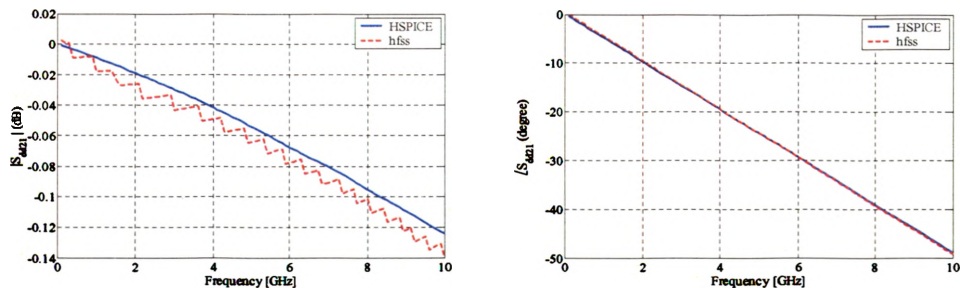
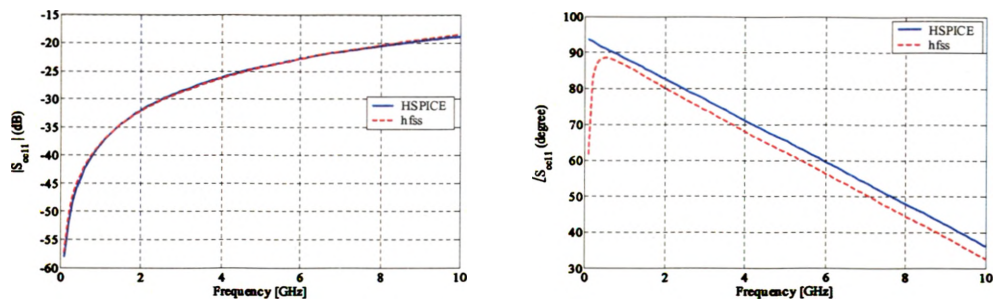
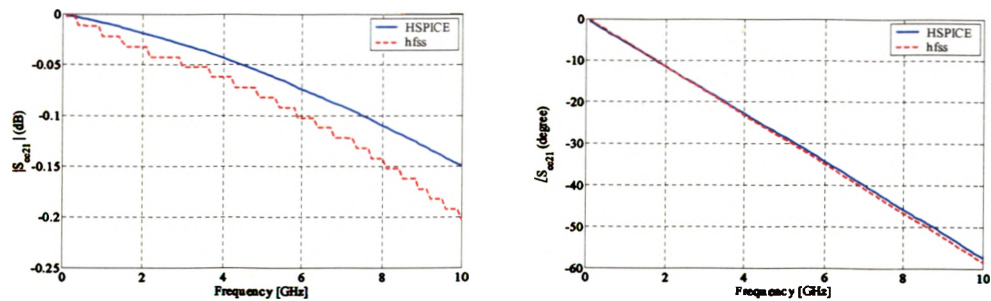
$$\begin{aligned}
 F = & \left(\frac{\text{Re}(S_{dd11}) - \text{Re}(S_{dd11} - \text{spice})}{\text{Re}(S_{dd11})} \right)^2 \\
 & + \left(\frac{\text{Im}(S_{dd11}) - \text{Im}(S_{dd11} - \text{spice})}{\text{Im}(S_{dd11})} \right)^2 \\
 & + 100 * \left(\frac{\text{Re}(S_{dd21}) - \text{Re}(S_{dd21} - \text{spice})}{\text{Re}(S_{dd21})} \right)^2 \\
 & + 100 * \left(\frac{\text{Im}(S_{dd21}) - \text{Im}(S_{dd21} - \text{spice})}{\text{Im}(S_{dd21})} \right)^2 \\
 & + \left(\frac{\text{Re}(S_{cc11}) - \text{Re}(S_{cc11} - \text{spice})}{\text{Re}(S_{cc11})} \right)^2 \\
 & + \left(\frac{\text{Im}(S_{cc11}) - \text{Im}(S_{cc11} - \text{spice})}{\text{Im}(S_{cc11})} \right)^2 \\
 & + 0.1 * \left(\frac{\text{Re}(S_{cc21}) - \text{Re}(S_{cc21} - \text{spice})}{\text{Re}(S_{cc21})} \right)^2 \\
 & + 0.1 * \left(\frac{\text{Im}(S_{cc21}) - \text{Im}(S_{cc21} - \text{spice})}{\text{Im}(S_{cc21})} \right)^2.
 \end{aligned} \tag{3.1}$$

After the curve fitting, the parameters of the HSPICE model were extracted as:

$$\begin{aligned}
 L &= 3.709 \times 10^{-1} \text{ nH}; \\
 C_1 &= 5.947 \times 10^{-2} \text{ pF}; \\
 C_2 &= 7.986 \times 10^{-2} \text{ pF}; \\
 C_{m1} &= 1.099 \times 10^{-17} \text{ pF}; \\
 C_{m2} &= 7.068 \times 10^{-3} \text{ pF}; \\
 M &= 7.660 \times 10^{-2} \text{ nH}.
 \end{aligned}$$

The comparison of mixed mode S-parameters of SPICE model and HFSS simulation results for geometry in Figure 3.17 is shown in Figure 3.18 -- Figure 3.21.

The geometry used to extract parameters of Block D₉ is shown in Figure 3.22, which includes two Block A₁ and one Block D₉.

Figure 3.18. Comparison of S_{dd11} .Figure 3.19. Comparison of S_{dd21} .Figure 3.20. Comparison of S_{cc11} .Figure 3.21. Comparison of S_{cc21} .

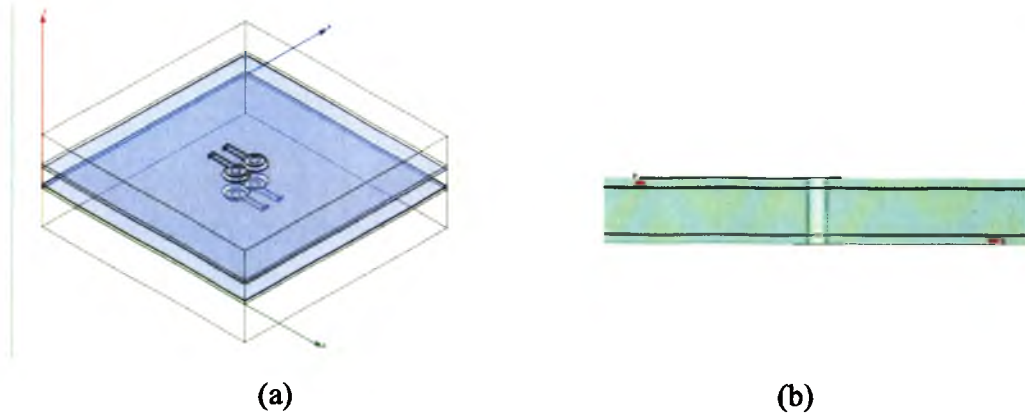


Figure 3.22. The geometry used to extract the parameters of Block D₉. (a) perspective view, (b) side view.

The objective function used in the optimization procedure is

$$\begin{aligned}
 F = & 10 * \left(\frac{\text{Re}(S_{dd11}) - \text{Re}(S_{dd11} - \text{spice})}{\text{Re}(S_{dd11})} \right)^2 \\
 & + 10 * \left(\frac{\text{Im}(S_{dd11}) - \text{Im}(S_{dd11} - \text{spice})}{\text{Im}(S_{dd11})} \right)^2 \\
 & + \left(\frac{\text{Re}(S_{dd21}) - \text{Re}(S_{dd21} - \text{spice})}{\text{Re}(S_{dd21})} \right)^2 \\
 & + \left(\frac{\text{Im}(S_{dd21}) - \text{Im}(S_{dd21} - \text{spice})}{\text{Im}(S_{dd21})} \right)^2 \\
 & + \left(\frac{\text{Re}(S_{cc11}) - \text{Re}(S_{cc11} - \text{spice})}{\text{Re}(S_{cc11})} \right)^2 \\
 & + \left(\frac{\text{Im}(S_{cc11}) - \text{Im}(S_{cc11} - \text{spice})}{\text{Im}(S_{cc11})} \right)^2 \\
 & + 0.1 * \left(\frac{\text{Re}(S_{cc21}) - \text{Re}(S_{cc21} - \text{spice})}{\text{Re}(S_{cc21})} \right)^2 \\
 & + 0.1 * \left(\frac{\text{Im}(S_{cc21}) - \text{Im}(S_{cc21} - \text{spice})}{\text{Im}(S_{cc21})} \right)^2.
 \end{aligned} \tag{3.2}$$

After the curve fitting the parameters of the HSPICE model of Block D₉ was extracted as:

$$L = 5.521 \times 10^{-2} \text{ nH};$$

$$C_1 = 1.004 \times 10^{-1} \text{ pF};$$

$$C_{m1} = 1.653 \times 10^{-16} \text{ pF};$$

$$M = 1.852 \times 10^{-2} \text{ nH}.$$

The comparison of mixed mode S-parameters of HSPICE model and MWS simulation results for geometry in Figure 3.22 is shown in Figure 3.23 -- Figure 3.26.

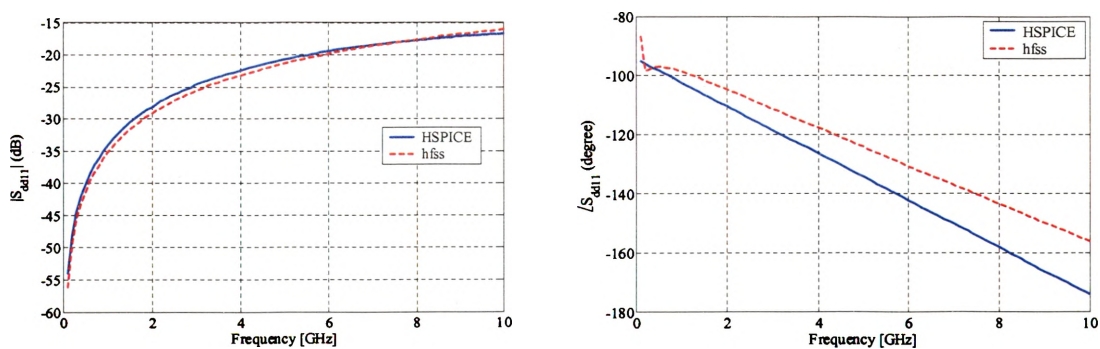


Figure 3.23. Comparison of S_{dd11} .

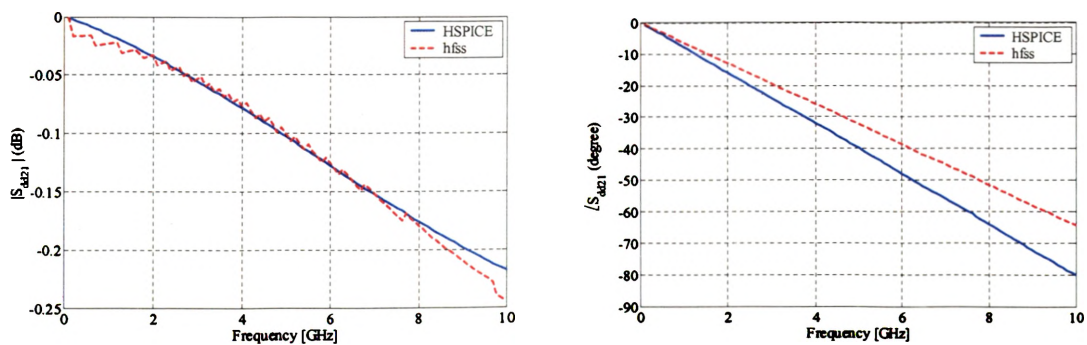


Figure 3.24. Comparison of S_{dd21} .

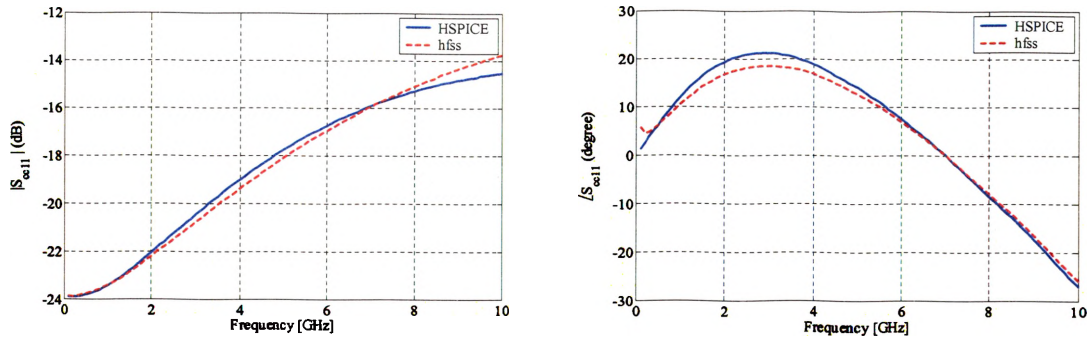


Figure 3.25. Comparison of S_{cc11}.

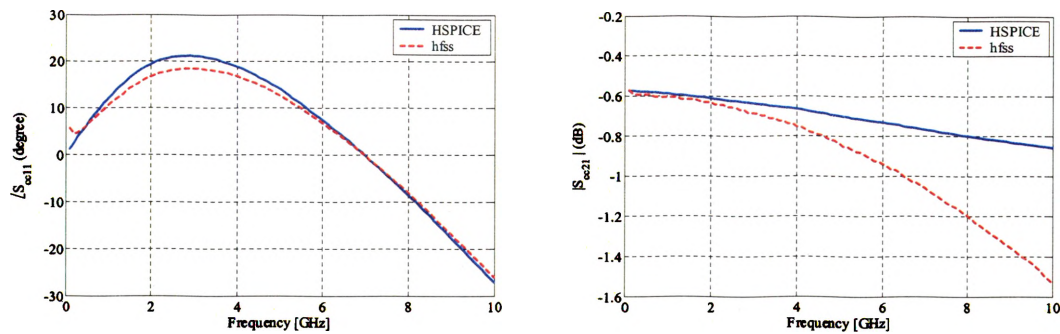
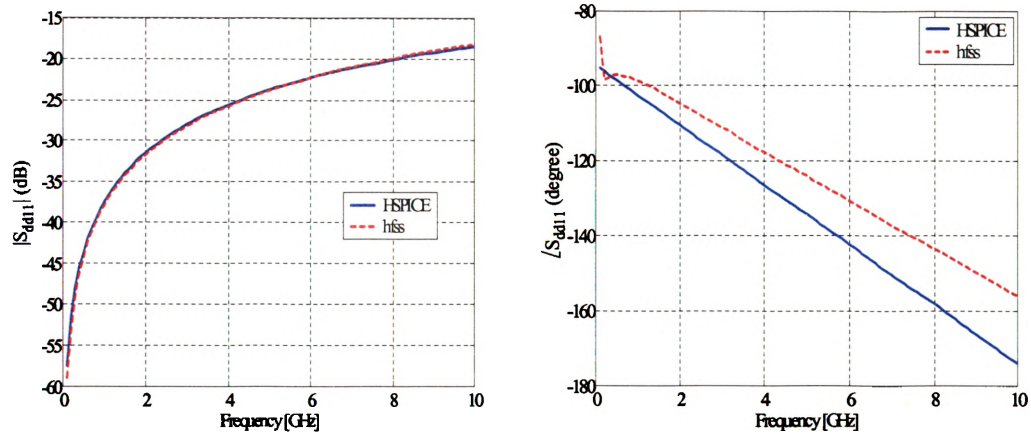
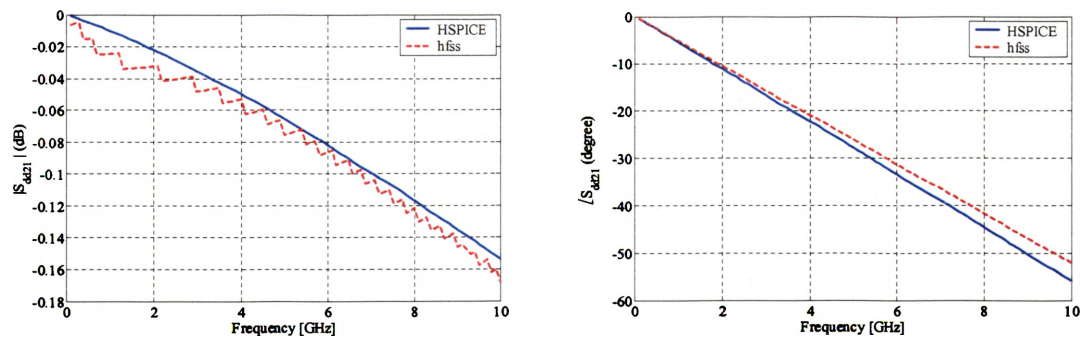
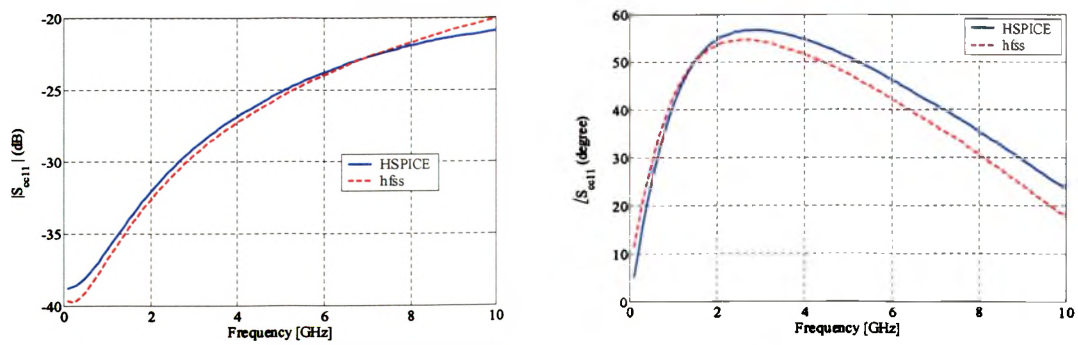


Figure 3.26. Comparison of S_{cc21}.

Similarly, the geometry used to extract Block D₁₀ is similar to the geometry in Figure 3.22. The different is the thickness of the middle dielectric layer. After the curve fitting, the parameters of the HSPICE model were extracted as:

$$\begin{aligned}
 L &= 9.010 \times 10^{-2} \text{ nH}; \\
 C_1 &= 2.260 \times 10^{-2} \text{ pF}; \\
 C_{m1} &= 2.508 \times 10^{-17} \text{ pF}; \\
 M &= 1.073 \times 10^{-2} \text{ nH}.
 \end{aligned}$$

The comparison of mixed mode S-parameters of HSPICE model and HFSS simulation results is shown in Figure 3.27 -- Figure 3.30.

Figure 3.27. Comparison of S_{dd11} .Figure 3.28. Comparison of S_{dd21} .Figure 3.29. Comparison of S_{cc11} .

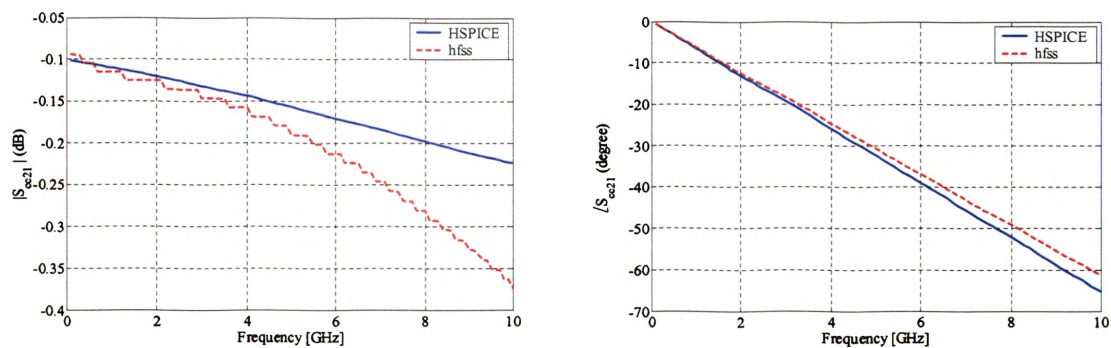


Figure 3.30. Comparison of S_{cc21} .

The geometry used to extract parameters of Block C_7 is shown in Figure 3.31, which includes one Block A_1 and a Block C_7 .

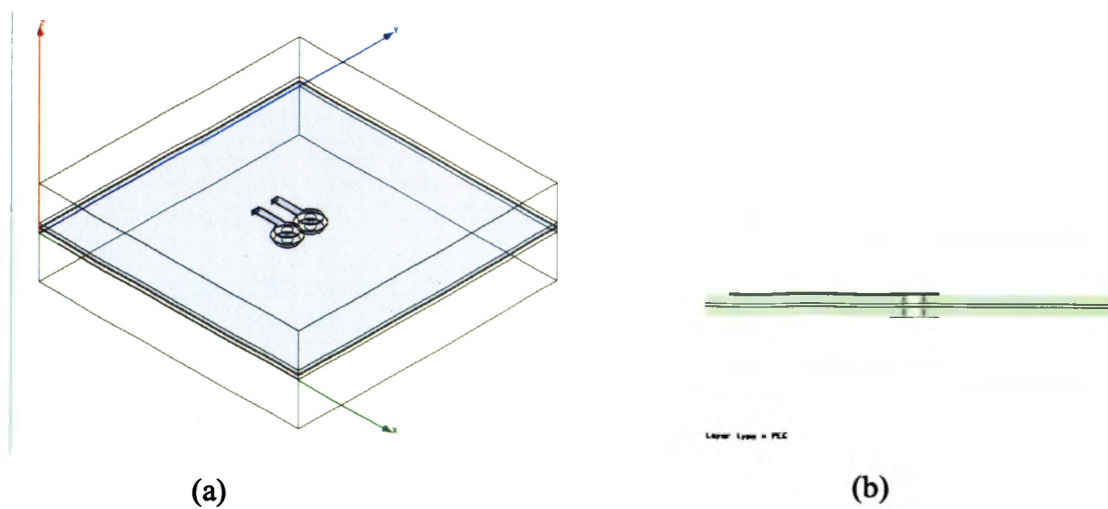


Figure 3.31. The geometry used to extract the parameters of Block C_7 . (a) perspective view, (b) side view.

The objective function used in the optimization procedure is

$$\begin{aligned}
 F = & \left(\frac{\text{Re}(S_{11}) - \text{Re}(S_{11_spice})}{\text{Re}(S_{dd11})} \right)^2 \\
 & + \left(\frac{\text{Im}(S_{11}) - \text{Im}(S_{11_spice})}{\text{Im}(S_{11})} \right)^2 \\
 & + \left(\frac{\text{Re}(S_{21}) - \text{Re}(S_{21_spice})}{\text{Re}(S_{21})} \right)^2 \\
 & + \left(\frac{\text{Im}(S_{21}) - \text{Im}(S_{21_spice})}{\text{Im}(S_{21})} \right)^2.
 \end{aligned} \tag{3.3}$$

After the curve fitting, the parameters of the HSPICE model were extracted as:

$$C_{c1} = 2.55\text{e-}9 \text{ pF};$$

$$C_{cm1} = 1.19\text{e-}2 \text{ pF};$$

$$C_{c2} = 1.21\text{e-}2 \text{ pF};$$

$$C_{cm2} = 2.60\text{e-}3 \text{ pF};$$

$$L_c = 8.17\text{e-}5 \text{ nH};$$

$$M_c = 5.99\text{e-}8 \text{ nH}.$$

The comparison of S-parameters of HSPICE model and HFSS simulation results is shown in Figure 3.32 and Figure 3.33.

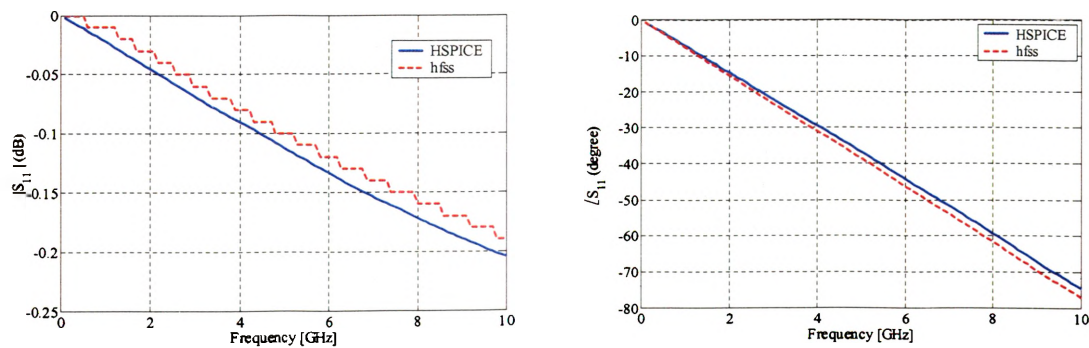


Figure 3.32. Comparison of S_{11} .

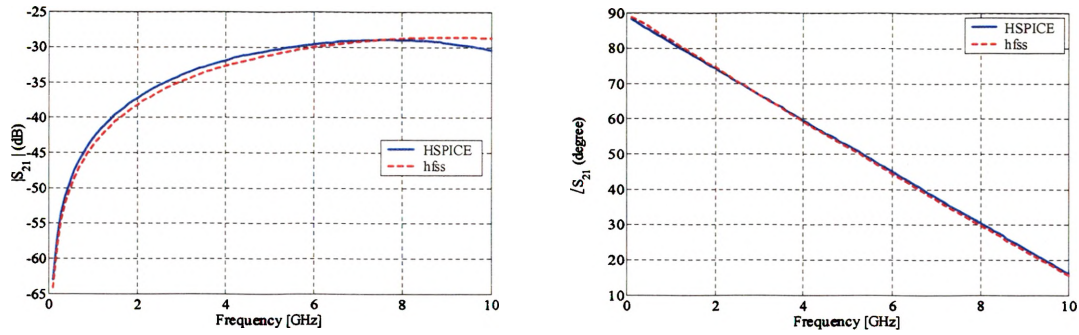


Figure 3.33. Comparison of S_{21} .

The geometry used to extract parameters of Block B_3 is shown in Figure 3.34, which includes one Block A_1 , Block C_7 and a Block B_3 . The differential signal traces are on the top layer and the third layer.

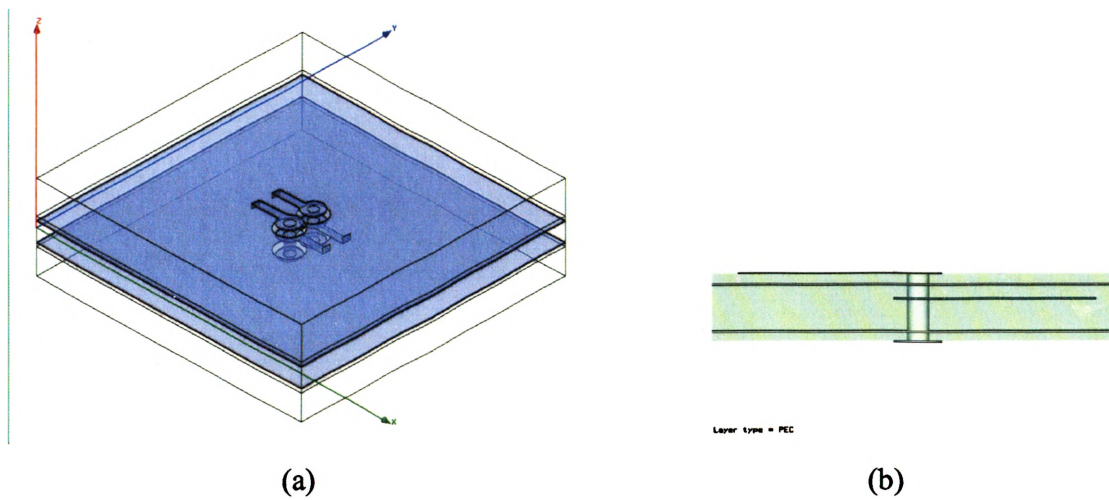


Figure 3.34. The geometry used to extract the parameters of Block B_3 . (a) perspective view, (b) side view.

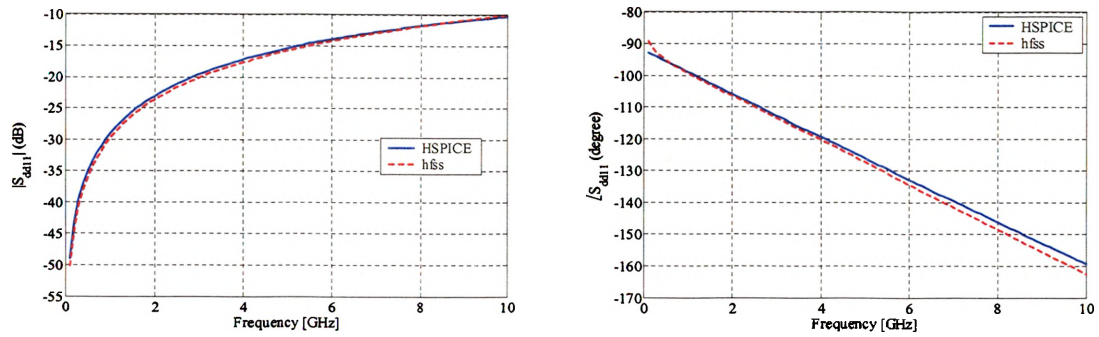
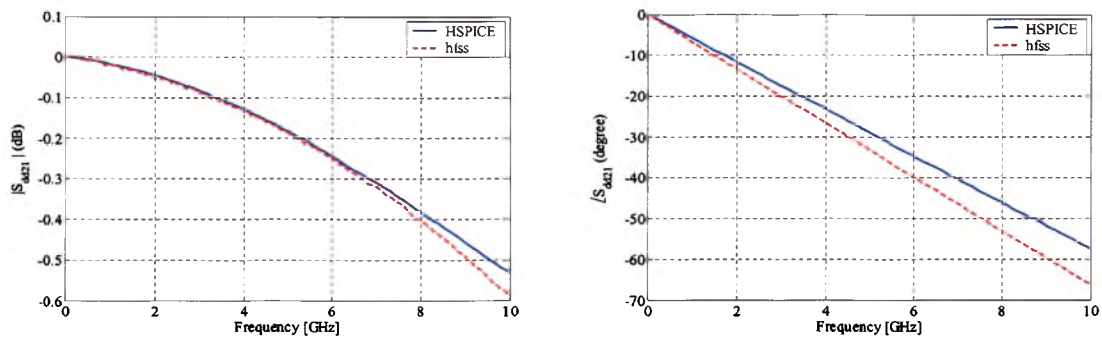
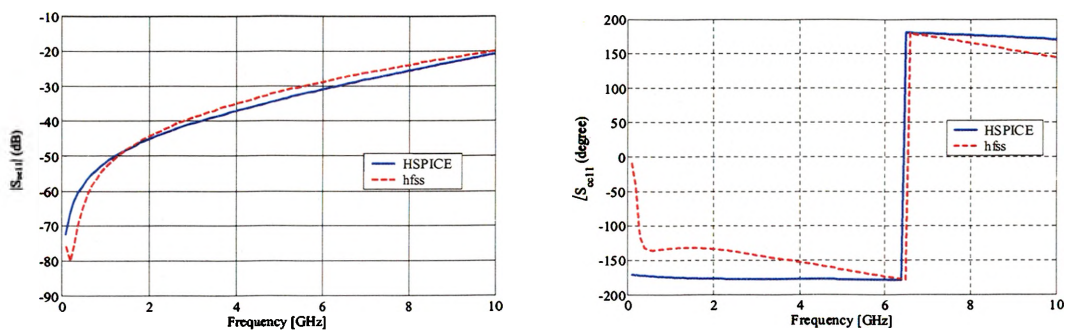
The objective function used in the optimization procedure is

$$\begin{aligned}
 F = & 10 * \left(\frac{\text{Re}(S_{dd11}) - \text{Re}(S_{dd11_spice})}{\text{Re}(S_{dd11})} \right)^2 \\
 & + 10 * \left(\frac{\text{Im}(S_{dd11}) - \text{Im}(S_{dd11_spice})}{\text{Im}(S_{dd11})} \right)^2 \\
 & + 10 * \left(\frac{\text{Re}(S_{dd21}) - \text{Re}(S_{dd21_spice})}{\text{Re}(S_{dd21})} \right)^2 \\
 & + 10 * \left(\frac{\text{Im}(S_{dd21}) - \text{Im}(S_{dd21_spice})}{\text{Im}(S_{dd21})} \right)^2 \\
 & + \left(\frac{\text{Re}(S_{cc11}) - \text{Re}(S_{cc11_spice})}{\text{Re}(S_{cc11})} \right)^2 \\
 & + \left(\frac{\text{Im}(S_{cc11}) - \text{Im}(S_{cc11_spice})}{\text{Im}(S_{cc11})} \right)^2 \\
 & + 0.1 * \left(\frac{\text{Re}(S_{cc21}) - \text{Re}(S_{cc21_spice})}{\text{Re}(S_{cc21})} \right)^2 \\
 & + 0.1 * \left(\frac{\text{Im}(S_{cc21}) - \text{Im}(S_{cc21_spice})}{\text{Im}(S_{cc21})} \right)^2.
 \end{aligned} \tag{3.4}$$

After the curve fitting, the parameters of the HSPICE model were extracted as:

$$\begin{aligned}
 L_1 &= 8.157 \times 10^{-6} \text{ nH}; \\
 M_1 &= 2.843 \times 10^{-6} \text{ nH}; \\
 L_2 &= 1.205 \times 10^{-9} \text{ nH}; \\
 M_2 &= 4.198 \times 10^{-10} \text{ nH}; \\
 L_3 &= 2.417 \times 10^{-1} \text{ nH}; \\
 M_3 &= 3.671 \times 10^{-6} \text{ nH}; \\
 C_1 &= 9.514 \times 10^{-2} \text{ pF}; \\
 C_{m1} &= 2.919 \times 10^{-12} \text{ pF}; \\
 C_2 &= 1.367 \times 10^{-8} \text{ pF}; \\
 C_{m2} &= 2.927 \times 10^{-2} \text{ pF}; \\
 C_3 &= 1.110 \times 10^{-11} \text{ pF}; \\
 C_{m3} &= 4.366 \times 10^{-2} \text{ pF}.
 \end{aligned}$$

The comparison of mixed mode S-parameters of HSPICE model and HFSS simulation results is shown in Figure 3.35 -- Figure 3.38.

Figure 3.35. Comparison of S_{dd11} .Figure 3.36. Comparison of S_{dd21} .Figure 3.37. Comparison of S_{cc11} .

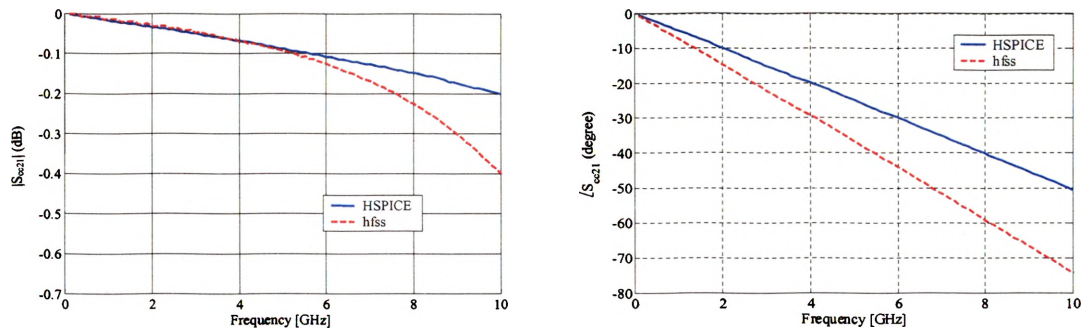


Figure 3.38. Comparison of S_{cc21} .

3.5. MODEL VALIDATION

To check the SPICE results from the extracted circuits, a test case for a differential via transition on a 10-layer board was simulated using full-wave simulation tools as shown in Figure 3.39. It consists of Block A_1 , D_9 , D_{10} , B_3 and C_7 . Differential signal traces on first and seventh layer were connected by a pair of through hole vias. Figure 3.40 - Figure 3.47 shows the comparison of the SPICE model and full-wave simulation results. The difference of magnitudes of S_{dd11} is within 3dB while the difference of magnitudes of S_{dd21} is within 0.05dB.

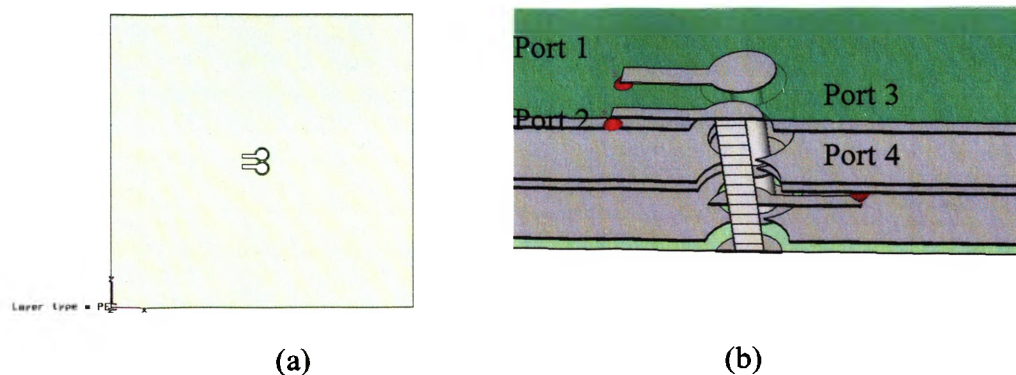
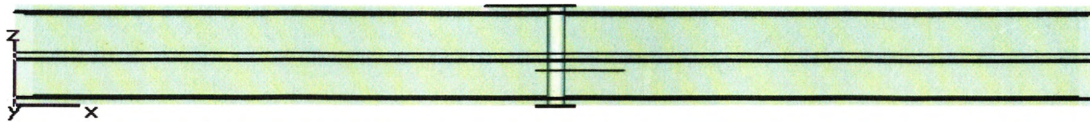


Figure 3.39. A 6-layer structure that consists of Block A_1 , D_9 , D_{10} , B_3 and C_7 . (a) top view, (b) perspective view, (c) side view.



(c)

Figure 3.39. A 6-layer structure that consists of Block A_1 , D_9 , D_{10} , B_3 and C_7 . (a) top view, (b) perspective view, (c) side view.(cont.)

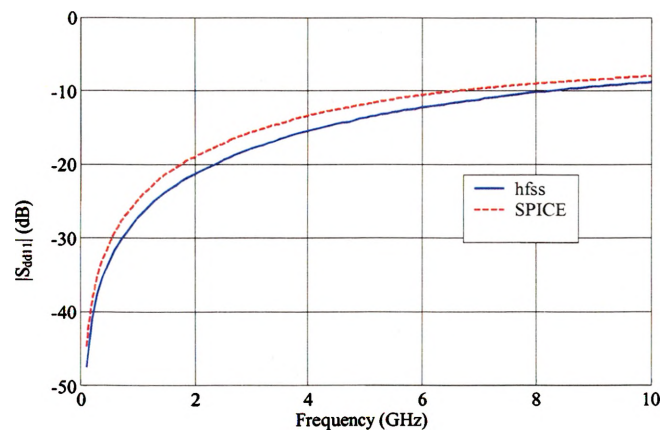


Figure 3.40. Comparison of magnitude of S_{dd11} of HSPICE model and full-wave model.

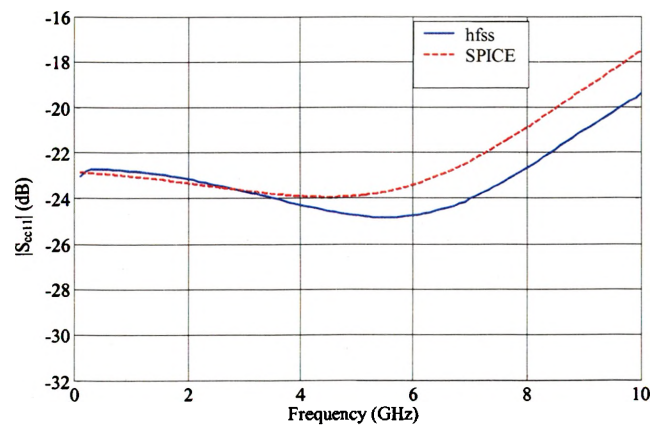


Figure 3.41. Comparison of phase of S_{dd11} of HSPICE model and full-wave model.

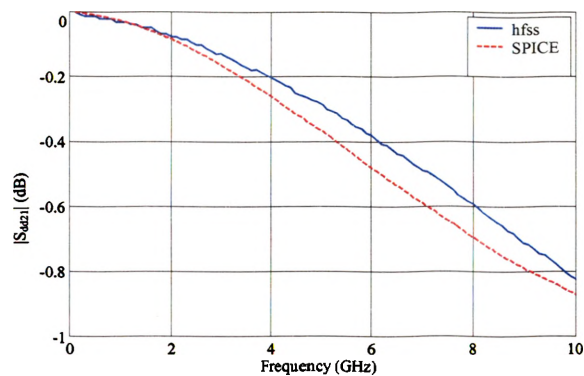


Figure 3.42. Comparison of magnitude of S_{dd21} of HSPICE model and full-wave model.

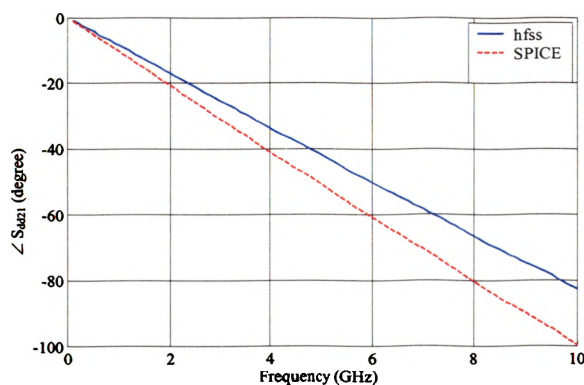


Figure 3.43. Comparison of phase of S_{dd21} of HSPICE model and full-wave model.

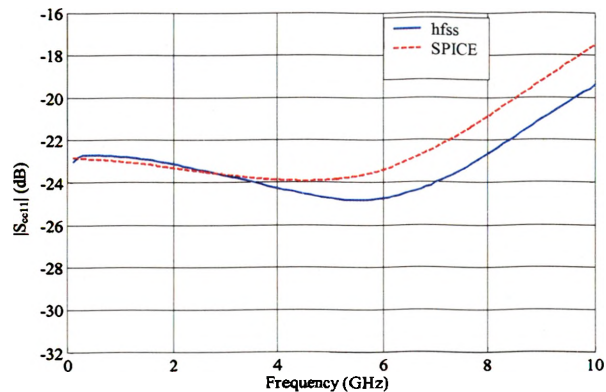


Figure 3.44. Comparison of magnitude of S_{cc11} of HSPICE model and full-wave model.

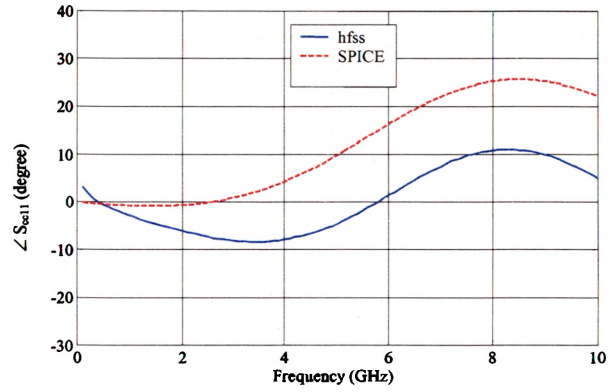


Figure 3.45. Comparison of phase of S_{cc11} of HSPICE model and full-wave model.

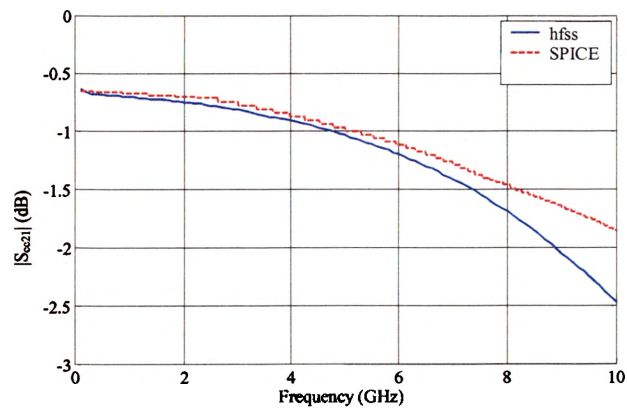


Figure 3.46. Comparison of magnitude of S_{cc21} of HSPICE model and full-wave model.

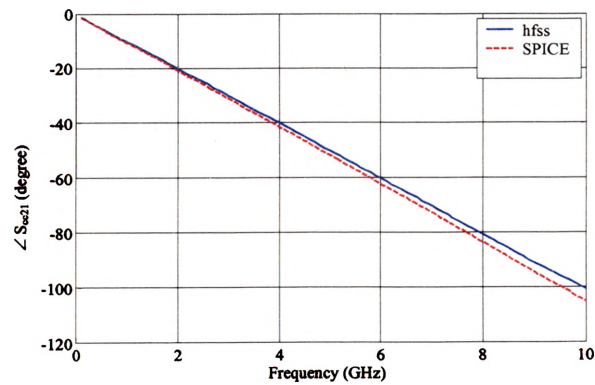


Figure 3.47. Comparison of phase of S_{cc21} of HSPICE model and full-wave model.

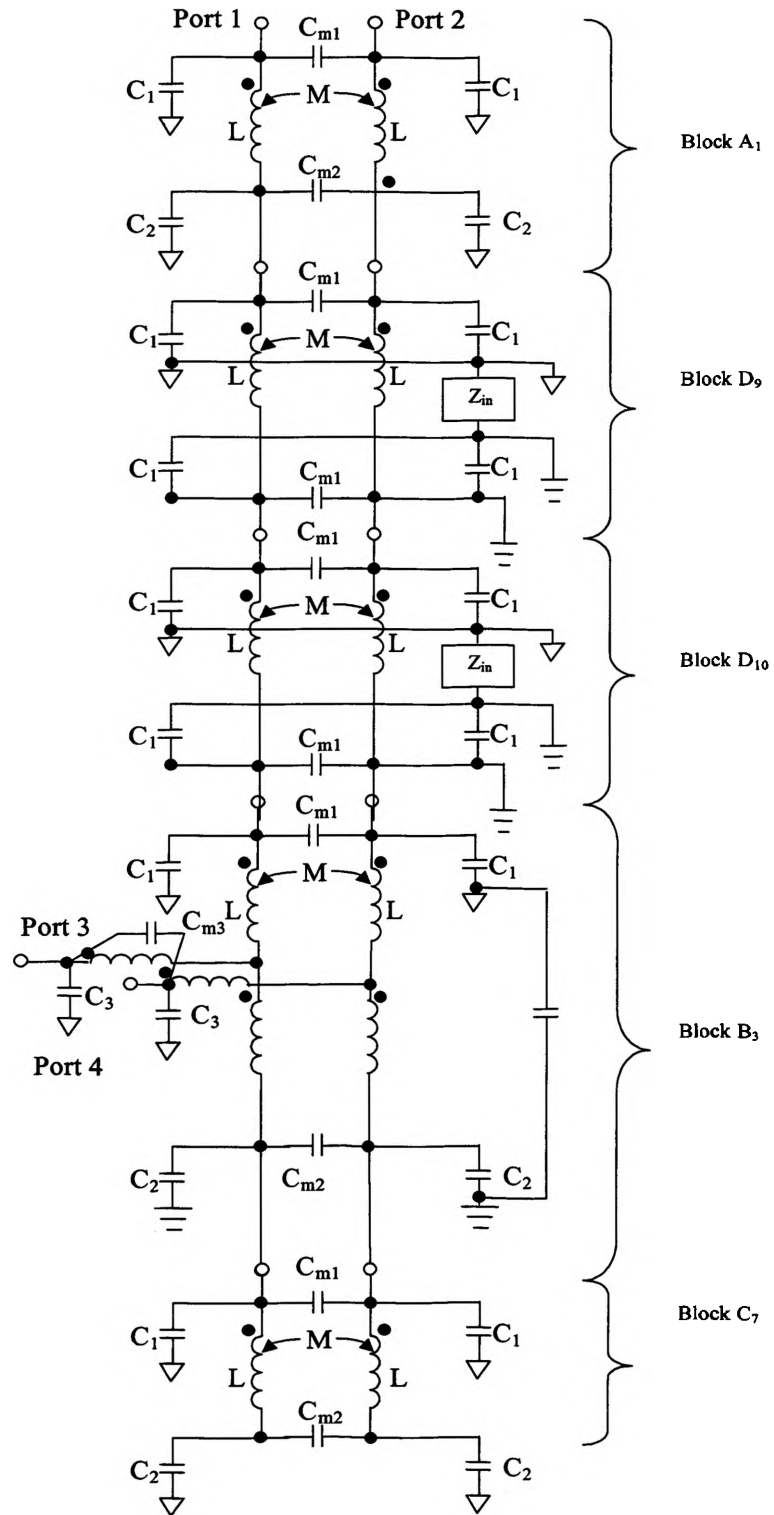


Figure 3.48. HSPICE model for a differential via pair.

3.6. CONCLUSION

With the study in this dissertation, it is shown that, for a given stackup of PCB, a SPICE model library for via transition of differential signaling can be built using the proposed peeling and partitioning method and every pair of vias on the board can be modeled by a few cascaded blocks in this library.

APPENDIX A

SUB-CIRCUIT MODEL OF DIFFERENTIAL VIA TRANSITIONS

*Block A1 model BLOCKA1

*
*
*
*

* Lumped Element Model

.SUBCKT BLOCKA1 1 2 5 6 10

.param La = 3.708967e-010 Ca1 = 5.946958e-014
.param Ca2 = 7.986275e-014 Cam1 = 1.099421e-029
.param Cam2 = 7.068109e-015

C1 1 10 Ca1
C2 2 10 Ca1
C5 5 10 Ca2
C6 6 10 Ca2
C3 1 2 Cam1
C4 5 6 Cam2
L1 1 5 La
L2 2 6 La
K1 L1 L2 2.065392e-001

rc20 1 10 r='1/(6.28*hertz*0.02*Ca1)*1.0'
rc21 2 10 r='1/(6.28*hertz*0.02*Ca1)*1.0'
rc22 5 10 r='1/(6.28*hertz*0.02*Ca2)*1.0'
rc23 6 10 r='1/(6.28*hertz*0.02*Ca2)*1.0'
rc25 1 2 r='1/(6.28*hertz*0.02*Cam1)*1.0'
rc26 5 6 r='1/(6.28*hertz*0.02*Cam2)*1.0'

.ENDS BLOCKA1

* Block A2 model BLOCKA2

*
*
*
*

* Lumped Element Model

.SUBCKT BLOCKA2 1 2 5 6 10

.param La = 7.535407e-010 Ca1 = 6.773277e-014
.param Ca2 = 8.389171e-014 Cam1 = 1.416958e-027 Cam2 = 7.327918e-025

C1 1 10 Ca1
C2 2 10 Ca1
C5 5 10 Ca2
C6 6 10 Ca2
C3 1 2 Cam1

```

C4 5 6 Cam2
L1 1 5 La
L2 2 6 La
K1 L1 L2 4.995271e-001
rc20 1 10 r='1/(6.28*hertz*0.02*Ca1)*1.0'
rc21 2 10 r='1/(6.28*hertz*0.02*Ca1)*1.0'
rc22 5 10 r='1/(6.28*hertz*0.02*Ca2)*1.0'
rc23 6 10 r='1/(6.28*hertz*0.02*Ca2)*1.0'
rc25 1 2 r='1/(6.28*hertz*0.02*Cam1)*1.0'
rc26 5 6 r='1/(6.28*hertz*0.02*Cam2)*1.0'

```

```
.ENDS BLOCKA2
```

```
* Block B3 model BLOCKB3
```

```
*
*
*
*
```

```
* Lumped Element Model
```

```
.SUBCKT BLOCKB3 5 6 3 4 7 8 10 1001
```

```
.param Lb3_1 = 8.157384e-015 Lb3_2 = 1.204559e-018 Lb3_3 = 2.416880e-010
```

```
.param Cb3_1 = 9.989805e-014 Cb3_m1 = 2.9187e-024
```

```
.param Cb3_2 = 1.367122e-020 Cb3_m2 = 2.926672e-014
```

```
.param Cb3_3 = 1.109776e-023 Cb3_m3 = 4.366493e-014
```

```
C13 5 10 Cb3_1
```

```
C14 6 10 Cb3_1
```

```
C15 7 1001 Cb3_2
```

```
C16 8 1001 Cb3_2
```

```
R17 10 1001 1.542300e+000
```

```
C18 5 6 Cb3_m1
```

```
C19 7 8 Cb3_m2
```

```
C34 3 10 Cb3_3
```

```
C35 4 10 Cb3_3
```

```
C36 3 4 Cb3_m3
```

```
L5 5 30 Lb3_1
```

```
L6 6 31 Lb3_1
```

```
K3 L5 L6 3.485000e-001
```

```
L37 30 7 Lb3_2
```

```
L38 31 8 Lb3_2
```

```
K39 L37 L38 3.485000e-001
```

```
L40 30 3 Lb3_3
```

```
L41 31 4 Lb3_3
```

```
K42 L40 L41 1.519061e-005
```

```
rc13 5 10 r='1/(6.28*hertz*0.02*Cb3_1)'
```

```

rc14 6 10 r='1/(6.28*hertz*0.02*Cb3_1)'
rc15 7 1001 r='1/(6.28*hertz*0.02*Cb3_2)'
rc16 8 1001 r='1/(6.28*hertz*0.02*Cb3_2)'
rc18 5 6 r='1/(6.28*hertz*0.02*Cb3_m1)'
rc19 7 8 r='1/(6.28*hertz*0.02*Cb3_m2)'
rc34 3 10 r='1/(6.28*hertz*0.02*Cb3_3)'
rc35 4 10 r='1/(6.28*hertz*0.02*Cb3_3)'
rc36 3 4 r='1/(6.28*hertz*0.02*Cb3_m3)'

```

.ENDS BLOCKB3

* Block B4 model BLOCKB4

*
*
*
*

* Lumped Element Model

.SUBCKT BLOCKB4 5 6 3 4 7 8 10 1001

.param Lb4_1 = 1.860580e-014 Lb4_2 = 8.701744e-019 Lb4_3 = 8.254848e-010

.param Cb4_1 = 1.828300e-013 Cb4_m1 = 3.243947e-019

.param Cb4_2 = 1.028294e-020 Cb4_m2 = 4.663562e-014

.param Cb4_3 = 3.578526e-024 Cb4_m3 = 7.759062e-014

C13 5 10 Cb4_1

C14 6 10 Cb4_1

C15 7 1001 Cb4_2

C16 8 1001 Cb4_2

R17 10 1001 9.704218e-001

C18 5 6 Cb4_m1

C19 7 8 Cb4_m2

C34 3 10 Cb4_3

C35 4 10 Cb4_3

C36 3 4 Cb4_m3

L5 5 30 Lb4_1

L6 6 31 Lb4_1

K3 L5 L6 3.485000e-001

L37 30 7 Lb4_2

L38 31 8 Lb4_2

K39 L37 L38 3.485000e-001

L40 30 3 Lb4_3

L41 31 4 Lb4_3

K42 L40 L41 1.942497e-006

rc13 5 10 r='1/(6.28*hertz*0.02*Cb3_1)'

rc14 6 10 r='1/(6.28*hertz*0.02*Cb3_1)'

rc15 7 1001 r='1/(6.28*hertz*0.02*Cb3_2)'

```

rc16 8 1001 r='1/(6.28*hertz*0.02*Cb3_2)'
rc18 5 6 r='1/(6.28*hertz*0.02*Cb3_m1)'
rc19 7 8 r='1/(6.28*hertz*0.02*Cb3_m2)'
rc34 3 10 r='1/(6.28*hertz*0.02*Cb3_3)'
rc35 4 10 r='1/(6.28*hertz*0.02*Cb3_3)'
rc36 3 4 r='1/(6.28*hertz*0.02*Cb3_m3)'
.ENDS BLOCKB4

```

```
* Block B5 model BLOCKB5
```

```
*
*
*
*
```

```
* Lumped Element Model
```

```
.SUBCKT BLOCKB5 5 6 3 4 7 8 10 1001
```

```
.param Lb5_1 = 2.234561e-010 Lb5_2 = 8.545785e-012 Lb5_3 = 5.001731e-010
```

```
.param Cb5_1 = 4.431822e-014 Cb5_m1 = 1.315880e-014
```

```
.param Cb5_2 = 2.079558e-013 Cb5_m2 = 2.498090e-023
```

```
.param Cb5_3 = 1.462159e-018 Cb5_m3 = 2.888650e-014
```

```
C13 5 10 Cb5_1
```

```
C14 6 10 Cb5_1
```

```
C15 7 1001 Cb5_2
```

```
C16 8 1001 Cb5_2
```

```
R17 10 1001 5.026277e+000
```

```
C18 5 6 Cb5_m1
```

```
C19 7 8 Cb5_m2
```

```
C34 3 10 Cb5_3
```

```
C35 4 10 Cb5_3
```

```
C36 3 4 Cb5_m3
```

```
L5 5 30 Lb5_1
```

```
L6 6 31 Lb5_1
```

```
K3 L5 L6 3.485000e-001
```

```
L37 30 7 Lb5_2
```

```
L38 31 8 Lb5_2
```

```
K39 L37 L38 3.485000e-001
```

```
L40 30 3 Lb5_3
```

```
L41 31 4 Lb5_3
```

```
K42 L40 L41 6.364640e-005
```

```
rc13 5 10 r='1/(6.28*hertz*0.02*Cb3_1)'
```

```
rc14 6 10 r='1/(6.28*hertz*0.02*Cb3_1)'
```

```
rc15 7 1001 r='1/(6.28*hertz*0.02*Cb3_2)'
```

```
rc16 8 1001 r='1/(6.28*hertz*0.02*Cb3_2)'
```

```
rc18 5 6 r='1/(6.28*hertz*0.02*Cb3_m1)'
```

```
rc19 7 8 r='1/(6.28*hertz*0.02*Cb3_m2)'
```

```
rc34 3 10 r=1/(6.28*hertz*0.02*Cb3_3)'
rc35 4 10 r=1/(6.28*hertz*0.02*Cb3_3)'
rc36 3 4 r=1/(6.28*hertz*0.02*Cb3_m3)'
.ENDS BLOCKB5
```

```
* Block B6 model BLOCKB6
```

```
*
*
*
*
```

```
* Lumped Element Model
```

```
.SUBCKT BLOCKB6 5 6 3 4 7 8 10 1001
```

```
.param Lb6_1 = 4.536253e-013 Lb6_2 = 8.773316e-015 Lb6_3 = 6.476208e-010
```

```
.param Cb6_1 = 1.936339e-013 Cb6_m1 = 1.106132e-015
```

```
.param Cb6_2 = 1.153513e-017 Cb6_m2 = 1.117692e-014 Cb6_3 = 4.802941e-021
```

```
Cb6_m3 = 1.927254e-015
```

```
C13 5 10 Cb6_1
```

```
C14 6 10 Cb6_1
```

```
C15 7 1001 Cb6_2
```

```
C16 8 1001 Cb6_2
```

```
R17 10 1001 4.698543e+001
```

```
C18 5 6 Cb6_m1
```

```
C19 7 8 Cb6_m2
```

```
C34 3 10 Cb6_3
```

```
C35 4 10 Cb6_3
```

```
C36 3 4 Cb6_m3
```

```
L5 5 30 Lb6_1
```

```
L6 6 31 Lb6_1
```

```
K3 L5 L6 3.485000e-001
```

```
L37 30 7 Lb6_2
```

```
L38 31 8 Lb6_2
```

```
K39 L37 L38 3.485000e-001
```

```
L40 30 3 Lb6_3
```

```
L41 31 4 Lb6_3
```

```
K42 L40 L41 3.390875e-001
```

```
rc13 5 10 r=1/(6.28*hertz*0.02*Cb3_1)'
```

```
rc14 6 10 r=1/(6.28*hertz*0.02*Cb3_1)'
```

```
rc15 7 1001 r=1/(6.28*hertz*0.02*Cb3_2)'
```

```
rc16 8 1001 r=1/(6.28*hertz*0.02*Cb3_2)'
```

```
rc18 5 6 r=1/(6.28*hertz*0.02*Cb3_m1)'
```

```
rc19 7 8 r=1/(6.28*hertz*0.02*Cb3_m2)'
```

```
rc34 3 10 r=1/(6.28*hertz*0.02*Cb3_3)'
```

```
rc35 4 10 r=1/(6.28*hertz*0.02*Cb3_3)'
```

```
rc36 3 4 r=1/(6.28*hertz*0.02*Cb3_m3)'
```

```

.ENDS BLOCKB6
* Block C7 model BLOCKC7
*
*
*1 and 2 are the ends of via stub
*
* Lumped Element Model
.SUBCKT BLOCKC7 1 2 5 6 10
.param Cc71 = 4.209073e-014 Cc7m1 = 9.470753e-016
.param Cc72 = 1.224817e-014 Cc7m2 = 3.030057e-015 Lc7 = 1.023131e-016
C1 1 10 Cc71
C2 2 10 Cc71
C5 5 10 Cc72
C6 6 10 Cc72
C3 1 2 Cc7m1
C4 5 6 Cc7m2
L1 1 5 Lc7
L2 2 6 Lc7
K1 L1 L2 2.054922e-001

rc20 1 10 r='1/(6.28*hertz*0.02*Cc71)*1.0'
rc21 2 10 r='1/(6.28*hertz*0.02*Cc71)*1.0'
rc22 5 10 r='1/(6.28*hertz*0.02*Cc72)*1.0'
rc23 6 10 r='1/(6.28*hertz*0.02*Cc72)*1.0'
rc25 1 2 r='1/(6.28*hertz*0.02*Cc7m1)*1.0'
rc26 5 6 r='1/(6.28*hertz*0.02*Cc7m1)*1.0'

```

```

.ENDS BLOCKC7

```

```

* Block C8 model BLOCKC8
*
*
*1 and 2 are the ends of via stub
*
* Lumped Element Model
.SUBCKT BLOCKC8 1 2 5 6 10
.param Cc1 = 2.998427e-028 Ccm1 = 1.383839e-014
.param Cc2 = 1.875724e-027 Ccm2 = 1.692378e-017 Lc = 5.893929e-028
C1 1 10 Cc1
C2 2 10 Cc1
C5 5 10 Cc2
C6 6 10 Cc2
C3 1 2 Ccm1
C4 5 6 Ccm2
L1 1 5 Lc
L2 2 6 Lc
K1 L1 L2 2.717948e-001

```

```

rc20 1 10 r='1/(6.28*hertz*0.02*Cc1)*1.0'
rc21 2 10 r='1/(6.28*hertz*0.02*Cc1)*1.0'
rc22 5 10 r='1/(6.28*hertz*0.02*Cc2)*1.0'
rc23 6 10 r='1/(6.28*hertz*0.02*Cc2)*1.0'
rc25 1 2 r='1/(6.28*hertz*0.02*Ccm1)*1.0'
rc26 5 6 r='1/(6.28*hertz*0.02*Ccm2)*1.0'
.ENDS BLOCKC8

```

```
* Block D9 model BLOCKD9
```

```
*
```

```
*
```

```
*
```

```
* Lumped Element Model
```

```
.SUBCKT BLOCKD9 11 12 9 10 1003 1002
```

```
.param Cd9m = 1.652689e-028 Cd9 = 1.004745e-013 Ld9 = 5.521096e-010
```

```
C20 11 1003 Cd9
```

```
C21 12 1003 Cd9
```

```
C22 9 1002 Cd9
```

```
C23 10 1002 Cd9
```

```
*V24 1002 1003 0
```

```
C25 11 12 Cd9m
```

```
C26 9 10 Cd9m
```

```
L7 9 11 Ld9
```

```
L8 10 12 Ld9
```

```
K4 L7 L8 3.353565e-001
```

```
rc20 11 1003 r='1/(6.28*hertz*0.02*Cd9)*1.0'
```

```
rc21 12 1003 r='1/(6.28*hertz*0.02*Cd9)*1.0'
```

```
rc22 9 1002 r='1/(6.28*hertz*0.02*Cd9)*1.0'
```

```
rc23 10 1002 r='1/(6.28*hertz*0.02*Cd9)*1.0'
```

```
rc25 11 12 r='1/(6.28*hertz*0.02*Cd9m)*1.0'
```

```
rc26 9 10 r='1/(6.28*hertz*0.02*Cd9m)*1.0'
```

```
R24 1002 1003 3.41
```

```
.ENDS BLOCKD9
```

```
* Block D10 model BLOCKD10
```

```
*
```

```
*
```

```
*
```

```
* Lumped Element Model
```

```
.SUBCKT BLOCKD10 7 8 9 10 1001 1002
```

```
.param Cd10m = 2.508110e-029 Cd10 = 2.259554e-014 Ld10 = 9.009758e-011
```

```
C27 7 1001 Cd10
```

```
C28 8 1001 Cd10
```

```
C29 9 1002 Cd10
C30 10 1002 Cd10
*V31 1001 1002 0.5835
```

```
R31 1001 1002 0.5835
```

```
rc20 7 1001 r='1/(6.28*hertz*0.02*Cd10)'  
rc21 8 1001 r='1/(6.28*hertz*0.02*Cd10)'  
rc22 9 1002 r='1/(6.28*hertz*0.02*Cd10)'  
rc23 10 1002 r='1/(6.28*hertz*0.02*Cd10)'  
rc25 7 8 r='1/(6.28*hertz*0.02*Cd10m)'  
rc26 9 10 r='1/(6.28*hertz*0.02*Cd10m)'
```

```
C32 7 8 Cd10m  
C33 9 10 Cd10m  
L9 7 9 Ld10  
L10 8 10 Ld10  
K5 L9 L10 1.190958e-001  
.ENDS BLOCKD10
```

```
* Block D11 model BLOCKD11
```

```
*  
*  
*
```

```
* Lumped Element Model
```

```
.SUBCKT BLOCKD11 11 12 9 10 1003 1002  
.param Cdm = 1.398043e-029 Cd = 6.065858e-014 Ld = 1.657496e-010  
C20 11 1003 Cd  
C21 12 1003 Cd  
C22 9 1002 Cd  
C23 10 1002 Cd  
R24 1002 1003 4.878469e+000  
C25 11 12 Cdm  
C26 9 10 Cdm  
L7 9 11 Ld  
L8 10 12 Ld  
K4 L7 L8 4.613274e-016
```

```
rc20 11 1003 r='1/(6.28*hertz*0.02*Cd)*1.0'  
rc21 12 1003 r='1/(6.28*hertz*0.02*Cd)*1.0'  
rc22 9 1002 r='1/(6.28*hertz*0.02*Cd)*1.0'  
rc23 10 1002 r='1/(6.28*hertz*0.02*Cd)*1.0'  
rc25 11 12 r='1/(6.28*hertz*0.02*Cdm)*1.0'  
rc26 9 10 r='1/(6.28*hertz*0.02*Cdm)*1.0'  
.ENDS BLOCKD11
```

```
* Block D12 model BLOCKD12
```

```
*
```



```
*  
*  
* Lumped Element Model  
.SUBCKT BLOCKD12 11 12 9 10 1003 1002  
.param Cdm = 5.120691e-030 Cd = 8.073583e-015 Ld = 8.739553e-012  
C20 11 1003 Cd  
C21 12 1003 Cd  
C22 9 1002 Cd  
C23 10 1002 Cd  
R24 1002 1003 2.415086e-001  
C25 11 12 Cdm  
C26 9 10 Cdm  
L7 9 11 Ld  
L8 10 12 Ld  
K4 L7 L8 1.975767e-002  
  
rc20 11 1003 r='1/(6.28*hertz*0.02*Cd)*1.0'  
rc21 12 1003 r='1/(6.28*hertz*0.02*Cd)*1.0'  
rc22 9 1002 r='1/(6.28*hertz*0.02*Cd)*1.0'  
rc23 10 1002 r='1/(6.28*hertz*0.02*Cd)*1.0'  
rc25 11 12 r='1/(6.28*hertz*0.02*Cdm)*1.0'  
rc26 9 10 r='1/(6.28*hertz*0.02*Cdm)*1.0'  
.ENDS BLOCKD12
```

APPENDIX B

USER'S GUIDE OF CEMPIE

CEMPIE, version 4.0 is a Visual C++ program implementing the circuit model extraction technique base on MPIE/MOM formulation. Matlab script **calc_Z.m** is a SPICE type circuit solver, which may solve the Z-parameters and S-parameters for external ports. **Triangle** is a public domain 2D triangular mesh generator written by Dr. Jonathan R. Schewchuk in Carnegie Mellon University. It is used for mesh generation.

B.1. INPUT FILES

Five kinds of input files need to be initialized for a given design. (1) Geometry definition files are "line0.poly", "line1.poly", etc. The number of files depends on how many metal layers the simulated structure has. The name "line" is the default name. User could specify any names, e.g. "mygeometry". Then the name of top metal layer file is "mygeometry0.poly", the second metal layer is "mygeometry1.poly", and so on and so forth. (2) Supper nodes definition file is "settings". (3) Stack up definition file is "stackup". (4) Vertical discontinuity definition file is "vd_setting". (5) Lumped element definition file is "capacitors".

The "line0.poly" file is the initial input polygon file for the mesh generator. The format of poly files is,

```

Number_of_nodes 2 0 0
Node_index x_coordinate y_coordinate
... (one line per node)
Number_of_edges 1
Edge_index start_node stop_node boundary_mark
... (one line per edge)
Number of holes
Hole_index x_coordinate y_coordinate
                (coordinates of an arbitrary point within the hole)
... (one line per hole)

```

Boundary marks should be specified for each edge: "0" for inner edges, "1" for outside edges where currents vanish, "2" for the intersection edges between the

top/bottom metal plane and the via/port. "3" and above for anti-pad edged of coaxial ports and the intersection edges between the internal metal plane and the via/port.

The "settings" file renders the selected points of interest as external ports. It also provides a mean to add lumped series LCR elements between some selected points of interest. The format of "settings" is

```

Number_of_user_selected_locations
Point_index x_coordinate y_coordinate layer reference_x reference_y
reference_layer
... (one line per point)
Number_of_lumped_series_LCR_elements
Element_index x_corrinate y_coordiante layer reference_x reference_y
reference_layer C L R
...(one line per point)

```

The "stackup" file specifies the layer stackup of the dielectric slabs seen in the cross-section of PCB. The format of "stackup" is

```

Number_of_dielectric_layers
Dielectric_layer_index relative_permittivity
losstangent_times_relative_permittivy (it is always a negative number for lossy material
and zero for lossless case) relative_permeability thickness_of_layer (in mils)
...(one line per dielectric layer)
Number_of_infinite_PEC_planes (1 or 0)
PEC_plane_index
0
Number_of_metal_layer
Index_of_metal_layer metal_layer_number(top layer is 0)
...(one line per metal layer)

```

The "vd_settings" file describes via and test port structures. Its format is given as

```

Number_of_vertical_discontinuities

```

*index x y top_layer bottom_layer radius type top_connected_layer
bottom_connected_layer reference_edge_type (from 3 ~) calibration_plane (1:
top_connected_layer, 0:bottom_connected_layer) (The first vertical discontinuity
should be the longest one)*

... (one line per vertical discontinuity)

Number of three PEC connections

index_of_vertical_discontinuities connected_layer

... (one line per three PEC connection)

The file "capacitors" gives the values of the lumped elements specified in "vd_settings". Each row, with three columns: C in F, L in H, and R in Ω .

B.2. MESH GENERATION

Once the initial polygon file is created, a triangle mesh can be created by executing the command

triangle -pen -a0.1 -q30 line0,

where the -a switch imposes an area constraint so that the areas of triangular patches are less than 0.1, and -q switch limits the minimum angle of any triangle no smaller than 30°. The mesh generator **triangle** will generate three files of concern: (1) "line0.1.node", the nodal coordinate file; (2) "line0.1.edge", the edge definition file; and (3) "line0.1.ele", the element definition file. The generated mesh can be viewed by executing

showme line0.1

and there is a button in the graphic interphase of showme to generate a PostScript file.

B.3. GENERATING COMPLEX IMAGES FOR THE GREEN'S FUNCTIONS

Complex images of Green's functions may be generated by executing

green4 -s0.001,

where the switch -s0.001 assumes that the unit used in the input file is mm.

B.4. CIRCUIT EXTRACTION

The circuit extraction may be performed by executing

cempie4_1 -mexample -s0.001 -n4 -f10,

where -m specifies the mesh file names, and -s0.001 is a reflection of the unit used in the input files.

B.5. SPICE SIMULATION

A Matlab script, "calc_Z.m", is used for circuit simulation. Specify the start frequency, stop frequency, total frequency points by modifying the "calc_Z.m" file. Then, in a Matlab environment, use the command

calc_Z.

The output will be saved in Matlab data files "ZZ.mat" and "SS.mat" for Z-parameters and S-parameters respectively.

BIBLIOGRAPHY

- [1] J. Fan, H. Shi, A. Orlandi, J. L. Knighten, J. L. Drewniak, "Modeling DC power-bus structures with vertical discontinuities using a circuit extraction approach based on a mixed-potential integral equation formulation," *IEEE Transactions on Advanced Packaging*, vol. 24, No. 2, pp. 143-157, May 2001.
- [2] A. E. Rueli, "Equivalent circuit models for three-dimensional multiconductor systems," *IEEE Trans. Microwave Theory Tech.*, vol. 22, pp. 216-221, March 1974.
- [3] A. E. Ruehli and H. Heeb, "Circuit models for three-dimensional geometries including dielectrics," *IEEE Trans. Microwave Theory Tech.*, vol. 40, pp. 1507-1515, July 1992.
- [4] B. Archambeault and A. Ruehli, "Electrical package modeling including voltage and ground reference planes using the Partial Element Equivalent Circuit (PEEC) method," in *Proc. 13th Int. Zurich Symp. Tech. Exhibition Electromagn. Compat.*, February 1999, pp. 233-238.
- [5] J. Fan, S. Luan, J. L. Drewniak, "Including SMT ferrite beads in DC power bus and high-speed I/O line modeling," in *Proc. IEEE Int. Symp. Electromagn. Compt.*, 2001. vol. 1, pp. 336-339.
- [6] J. Fan; J. L. Drewniak, J. L. Knighten, "Lumped-circuit model extraction for vias in multilayer substrates," *IEEE Trans. on Electromagn. Compt.*, vol. 45, pp. 272-280, May 2003.
- [7] W. Cui, J. Fan, S. Luan, J. L. Drewniak, "Modeling shared-via decoupling in a multi-layer structure using the CEMPIE approach," in *Proc. Electrical Performance of Electronic Packaging*, Oct. 2001, pp. 265-268.
- [8] S. Luan, J. Fan, W. Liu, F. Xiao, J. Knighten, N. Smith, R. Alexander, J. Nadolny, Y. Kami, J. Drewniak, "Extracting CAD models for quantifying noise coupling between vias in PCB layouts," in *Proc. Electronic Components and Technology Conf.*, 2002. pp. 343-346.
- [9] S. Luan, G. Selli, J. Fan, M. Lai, J. L. Knighten, N. W. Smith, R. Alexander, G. Antonini, A. Ciccomancini, A. Orlandi, J. L. Drewniak, "SPICE model libraries for via transitions," in *Proc. IEEE Int. Symp. Electromagn. Compt.*, 2003. vol. 2, pp. 859-864.
- [10] J. Fan, J. L. Drewniak, H. Shi, J. L. Knighten, "DC power-bus modeling and design with a mixed-potential integral equation formulation and circuit extraction," *IEEE Trans. on Electromagn. Compt.*, vol. 43, pp. 426-436, November 2001.
- [11] J. Fan, Y. Ren, J. Chen, D. M. Hockanson, H. Shi, J. L. Drewniak, T. H. Hubing, T. P. Van Doren, R. E. DuBroff, "RF isolation using power islands in DC power bus design," in *Proc. IEEE Int. Symp. Electromagn. Compt.*, 1999. vol. 2, pp. 838-843.

- [12] H. Shi, J. Fan, J. Drewniak, T. Hubing, T. P. Van Doren, "Modeling multilayered PCB power-bus designs using an MPIE based circuit extraction technique," in *Proc. IEEE Int. Symp. Electromagn. Compt.*, 1998. vol. 2, pp. 647-651.
- [13] S. Luan, F. Xiao, W. Liu, J. Fan, Y. Kami, J. L. Drewniak, R. E. DuBroff. "Modeling noise coupling from non-parallel PCB trace routing," in *Proc. IEEE Int. Symp. Electromagn. Compt.*, 2002. vol. 1, pp. 109-112.
- [14] H. Shi, "Study of printed circuit board power-bus design with a Circuit Extraction Technique Based on a Quasi-Static MPIE/MOM Formulation," Ph. D Dissertation, Department of Electrical and Computer Engineering, University of Missouri-Rolla, 1997.
- [15] S. Rao, D. Wilton, A. Glisson, "Electromagnetic Scattering by Surfaces of Arbitrary Shape," *IEEE Trans. on Antennas Propagat.*, vol. 30, pp. 409-418, May 1982.
- [16] D. Dural, and M. I. Aksun, "Closed-form Green's functions for general sources and stratified media," *IEEE Trans. on Microwave Theory Tech.*, vol. 43, pp. 1545-1552, July 1995.
- [17] C. H. Chan and R. A. Kipp, "Application of the complex image method to characterization of microstrip vias," *Int. J Microwave Millimeter-wave CAE*, vol. 7, pp. 368-379, 1997.
- [18] M. I. Aksun, "A robust approach for the derivation of closed-form Green's functions," *IEEE Trans. on Microwave Theory Tech.*, vol. 44, pp. 651-658, May 1996.
- [19] J. Fan, "Modeling and design of DC power buses in high-speed digital circuit designs," Ph.D Dissertation, Department of Electrical and Computer Engineering, University of Missouri-Rolla, 2000.
- [20] W. C. Chew, *Waves and Fields in Inhomogeneous Media*, IEEE Press, NJ. 1995.
- [21] M. I. Aksun, "Efficient use of closed-form green's functions for three-dimensional problems involving multilayered media," *IEEE Trans. on Antennas Propagat.*, vol. 2, pp. 1354-1357, June 1994.
- [22] M. I. Aksun and R. Mittra, "Choices of expansion and testing functions for the method of moments applied to a class of electromagnetic problems," *IEEE Trans. on Microwave Theory Tech.*, vol. 41, pp. 503-509, March 1993.
- [23] J. Zhao and J. Fang, "Validity of mutual inductor model for electromagnetic coupling between vias in integrated-circuit packages and printed circuit boards," in *Proc. 48th Electronic Components & Technology Conference*, Seattle, Washington, 1998, pp. 1083-1088.
- [24] J. Hwang and T. Wu, "Coupling of the ground bounce noise to the signal trace with via transition in partitioned power bus of PCB," in *Proc. IEEE Int. Symp. Electromagn. Compat.* 2002. pp. 733-736.
- [25] C. Wang, J. Fan, J. Knighten, N. Smith, R. Alexander, and J. Drewniak, "The effects of via transitions on differential signals," in *Proc. Electrical Performance of Electronic Packaging*, 2001, pp. 39-42.

- [26] T. Wang, R.F. Harrington, J. R. Mautz, "Quasi-static analysis of a microstrip via through a hole in a ground plane," *IEEE Trans. Microwave Theory Tech.*, vol. 36, pp. 1008-1013, July 1992.
- [27] P.A. Kok, D. De Zutter, "Prediction of the excess capacitance of a via-hole through a multilayered board including the effect of connecting microstrips or striplines," *IEEE Trans. Microwave Theory Tech.*, vol. 42, pp. 2270-2276, July 1992.
- [28] E. Laermans, J. D. Geest, D. De Zutter, F. Olyslager, S. Sercu, D. Morlion, "Modeling Complex Via Hole Structures," *IEEE Trans. Microwave Theory Tech.*, vol. 25, pp. 206-214, May 2002.
- [29] J. Fan, J.L. Knighten, N.W. Smith, J.L. Drewniak, and A. Orlandi, "Calculation of self and mutual inductances associated with vias in a DC power bus structure from a circuit extraction approach based on a mixed-potential integral equation formulation," in *Proc. of the 14th International Zurich Symp. And Technical Exhibition on EMC*, Switzerland, Zurich, 2001.
- [30] Takanori Okoshi, *Planar Circuits for Microwaves and Lightwaves*, Springer-Verlag Berlin Heidelberg, 1985, pp. 10-42.
- [31] G. T. Lei, R. W. Techentin, P. R. Hayes, D. J. Schwab, and B. K. Gilbert, "Wave model solution to the ground/power plane noise problem," *IEEE Transactions on Instrumentation and Measurement*, vol. 44, No. 2, pp. 300-303, April 1995.
- [32] X. Ye, M. Y. Koledintseva, M. Li, and J. L. Drewniak, "DC power bus design using FDTD modeling with dispersive media and surface mount technology components," *IEEE Transaction on Electromagnetic Compatibility*, vol. 43, No. 4, pp. 579-587, November 2001.
- [33] E. Laermans, J. De Geest, D. De Zutter, F. Olyslager, S. Sercu, and D. Morlion, "Modeling differential via holes," in *Proc. 9th Topical Meeting Elect. Performance Electron. Packag.*, Scottsdale, AZ, October 2000, pp. 127-130.
- [34] E. Laermans, J. De Geest, D. De Zutter, F. Olyslager, S. Sercu, and D. Morlion, "Modeling differential via holes," *IEEE Trans. Adv. Packag.*, vol. 24, pp. 357-363, August 2001.
- [35] Chen Wang, Drewniak, J.L., Jun Fan, Knighten, J.L., Smith, N.W., Alexander, R., "Transmission line modeling of vias in differential signals," in *Proc. IEEE Int. Symp. Electromagn. Compat.*, 2002. pp. 249-252.
- [36] Luan, S., Selli, G., Fan, J., Lai, M., Knighten, J.L., Smith, N.W., Alexander, R., Antonini, G., Ciccomancini, A., Orlandi, A., Drewniak, J.L., "SPICE model libraries for via transitions," in *Proc. IEEE Int. Symp. Electromagn. Compat.*, 2003. pp. 859-864.
- [37] G. Antonini, A.C. Scogna, A. Orlandi, "S-Parameters characterization of through, blind, and buried via holes," *IEEE Trans. on Mobile Computing*, vol. 2, Issue 2, pp 174-184, April-June 2003.

VITA

Shaofeng Luan was born on August 5, 1972 in Sichuan, China. He received his Bachelor and Master degrees in Electronic Engineering in 1994 and 1999 in Tsinghua University, Beijing, China. From 1999 to 2000, he was a software engineer in Lenovo Group and then in Motorola (China) Ltd. He enrolled at the University of Missouri-Rolla as a graduate student in the Electrical Engineering Department in 2000. He received a research assistantship from UMR EMC Laboratory and Department of Electrical and Computer Engineering during his Ph.D. study. He graduated with a Ph.D. in May 2005.